SPATIAL FILTERING OF MAGNETOENCEPHALOGRAPHIC DATA IN SPHERICAL HARMONICS DOMAIN

by

Tolga Esat Özkurt

B.Sc in E.C.E., Istanbul Technical University, 2002

M.Sc in C.S., Istanbul Technical University, 2004

Submitted to the Graduate Faculty of

Swanson School of Engineering in partial fulfillment

of the requirements for the degree of

Doctor of Philosophy

University of Pittsburgh

2009

UNIVERSITY OF PITTSBURGH

SWANSON SCHOOL OF ENGINEERING

This dissertation was presented

by

Tolga Esat Özkurt

It was defended on

January 29th 2009

and approved by

Mingui Sun, Electrical and Computer Engineering

Robert J. Sclabassi, Electrical and Computer Engineering

Luis F. Chaparro, Electrical and Computer Engineering

Zhi-Hong Mao, Electrical and Computer Engineering

William F. Eddy, Statistics, CMU

Dissertation Director: Mingui Sun, Electrical and Computer Engineering

SPATIAL FILTERING OF MAGNETOENCEPHALOGRAPHIC DATA IN SPHERICAL HARMONICS DOMAIN

Tolga Esat Özkurt, PhD

University of Pittsburgh, 2009

We introduce new spatial filtering methods in the spherical harmonics domain for constraining magnetoencephalographic (MEG) multichannel measurements to user-specified spherical regions of interests (ROI) inside the head. The main idea of the spatial filtering is to emphasize those signals arising from an ROI, while suppressing the signals coming from outside the ROI. We exploit a well-known method called the signal space separation (SSS), which can decompose MEG data into a signal component generated by neurobiological sources and a noise component generated by external sources outside the head. The novel methods presented in this work, expanded SSS (exSSS) and generalized expanded SSS (genexSSS) utilize a beamspace optimization criterion in order to linearly transform the inner signal SSS coefficients to represent the sources belonging to the ROI. The filters mainly depend on the radius and the center of the ROI. The simplicity of the derived formulations of our methods stems from the natural appropriateness to spherical domain and orthogonality properties of the SSS basis functions that are intimately related to the vector spherical harmonics. Thus, unlike the traditional MEG spatial filtering techniques, exSSS and genexSSS do not need any numerical computation procedures on discretized headspace. The validation and performance of the algorithms are demonstrated by experiments utilizing both simulated and real MEG data.

TABLE OF CONTENTS

LIST OF TABLES

LIST OF FIGURES

PREFACE

The whole work that is described in this thesis was realized in the Laboratory for Computational Neuroscience of University of Pittsburgh.

The first time I had seen the pictures of the directors of the lab, Dr. Mingui Sun and Dr. Robert J. Sclabassi, was during my MSc studies in Istanbul, Turkey sometime near the end of 2002. They were the coauthors of an IEEE Transactions on Biomedical Engineering paper, whose first author was my ex-advisor Dr. Tayfun Akgül. Since then, I had constructed the lab as an imago of an environment to develop signal processing algorithms especially for the brain signals. I clearly recall thinking that it would be real cool to play with something related to brain! Then, as the river of my destiny drifted me to this path, just about after 3 years, I have had the opportunity to work in the lab throughout my doctorate studies.

I am deeply grateful to my advisor Dr. Mingui Sun, who showed me how to ask scientific questions and answer them properly, who listened to me patiently and provided the convenient environment to pursue the doctorate program. Without his suggestions, patience, support, friendship and encouragement, this thesis would not be possible. I would like to specially thank Dr. Robert J. Sclabassi for his inspirational thoughts during our discussions. His precious support to my studies is more than greatly acknowledged.

I would like to express my sincere thanks to my committee members Drs. Bill Eddy, Luis F. Chaparro and Zhi-Hong Mao. Each of them challenged, criticized my work with their constructing questions and comments. Their invaluable suggestions helped me tremendously to complete this thesis.

A special thanks goes to my colleagues Steven Hackworth, Dr. Wenyan Jia, Dr. Gusphyl Justin, Eliezer Y. Kanal and Seda Şenay, whose witty, humorous dialogues and suggestions are deeply appreciated.

The MEG experiments in the thesis were conducted in the Center for Advanced Brain Magnetic Source Imaging (CABMSI) and University of Pittsburgh Medical Center (UPMC). My thanks, too, to the director of CABMSI, Dr. Anto Bagic, who has been helpful and kind to provide the necessary conditions for the use of the MEG system.

I am indebted to all my dear friends in Pittsburgh and all over the world for their support, solidarity and most importantly their warmth of existence I felt in my hard times while dealing with the doctorate. Last but certainly not least, I am more than grateful to my parents and my two little sisters for their continuous support and care during my studies. Without them, this thesis would not exist at all.

Tolga Esat Özkurt
Pittsburgh, January 2009

1.0 INTRODUCTION

Magnetoencephalography (MEG) and Electroencephalography (EEG) are noninvasive measurement tools that provide high temporal resolution on the units of milliseconds to investigate neuronal activity in the brain [1], [2]. MEG measures the magnetic fields produced by the current sources in the brain utilizing gradiometers and/or magnetometers connected to the superconducting quantum interference devices (SQUIDs) as sensors. The sensor array of modern MEG devices contains between 100 and 400 sensors.

The current sources contributing to the magnetic fields outside the head can be classified into the primary currents which are related to the ionic movements reflecting the neuronal activity and the secondary currents (it has also been called volume, ohmic or return currents in MEG literature) that are extracellular and produced as the effect of the primary currents to complete the circuit as necessitated by the conservation principle of the electric charges [2]. The synchronous activities of tens of thousands of the neurons give rise to the primary currents in the orders of 10 nAm that might cause measurable magnetic fields about 50-500 fT. Since the MEG signals are considered as extremely weak (on the order of ten billionth of the earth's geomagnetic field [1]), elimination of the external interferences such as earth's geomagnetic noise, instrumental noise coming from elevators, microwaves, power-line fields, etc.; and the biological noise arising from heart beats, eye and muscle movements becomes of an important concern. Apart from the necessity of superior sensitivity of the SQUIDs for proper measurement of the magnetic fields induced by the neurons, hardware solutions exist for the avoidance of noise include shielded rooms, reference channels or special sensing units such as the gradiometers, which correspond to the spatial derivatives of the magnetic fields measured outside the head.

The most known way to approximate the primary currents is achieved by dipole modeling. The dipole basically represents the current concentrated to a single point; hence the source space can always be divided into grids, each of which stands for a current dipole. The MEG forward problem assumes that we have the knowledge of the current dipole parameters (namely the strength, location and the orientation), and this problem corresponds to computing the magnetic field measurements from these parameters for a particular head model. Since the mapping between currents and the magnetic fields is well known from the classical physics by the aid of Maxwell's equations, the forward problem is unique and consistent. However, in practice, contrary to the formulation of the forward problem, we know only the sensor measurements from which we aim to investigate the source characteristics for imaging the brain with the fine temporal resolution capability of MEG. Accordingly, the challenge to estimate the source parameters from the measurements is defined as inverse problem. Unlike the forward problem, it is non-unique and hence ill-posed since there are theoretically infinite amounts of combinations of different sources that may give rise to the same MEG measurements. As a result, the inverse problem requires some constraints or *a priori* knowledge of the current sources for accurate solutions to the source localization and source waveform reconstruction.

MEG and EEG are unique noninvasive techniques that can provide us information about neural activities with a temporal resolution below 100 ms. The neural activities are implicitly given as the weighted integration of current source densities. These weights, which are called as leadfields, are basically mappings from the current sources to the magnetic fields outside the head for MEG and to the electrical potentials on the scalp for EEG. The similarity of these formulations enables the use of the some similar inverse methods and spatial filtering techniques for both modalities. These common methods typically assume the knowledge of the properties of the current sources and then compute the leadfields according to the physics behind EEG and MEG. However, unlike these methods, which exploit the linear relation between *a priori* known leadfields and the measurements, the proposed novel spatial techniques in this thesis take advantage of some properties that are only specific to MEG and hence they can only be utilized for MEG.

Because of the sophisticated hardware of MEG to be able to sense the tiny magnetic fields, MEG is much more expensive than EEG. However, the cost of it also comes with an advantage to MEG, which has a better brain source localization accuracy than that of EEG. This advantage stems from the fact that MEG is much less vulnerable to the distortions caused by various layers of cerebrum such as skull, scalp, muscle and cerebrospinal [1], [2]. Hence, the leadfields for MEG are much less susceptible to conductivity profiles and thickness properties of the head. For instance, for spherical head models, the leadfield computations do not require the head parameters for MEG, while they have to be known for determining the leadfields of EEG. This leads to a requirement of a realistic head model for EEG for accurate forward modeling, which increases the computational complexity significantly. Moreover, it is not straightforward to obtain an accurate estimation of conductivities without high-resolution images of the brain [3]. In an experimental study [3] using a realistically designed phantom having 32 dipoles, localization errors were detected to be around 3 mm for MEG and 7-8 mm for EEE in average. Nevertheless, MEG is known to be blind to totally radially oriented dipoles, hence EEG is still considered complementary to MEG for the investigation of the neural activities within the brain [4], [5].

1.1 AIM OF RESEARCH

Most information contained in MEG measurements reflects signals originating from the cortex because of the relatively short distances between the cortex and the sensors in the MEG system. While there have been some attempts to detect the sources arising from deep areas of the brain, such as brainstem [6], thalamus [7], hippocampus [8] and cerebellum [9], the nature of these studies was experimental and their success was highly dependent on the signal quality and the utilization of a realistic head model such as boundary element method (BEM) for the forward calculations. In this dissertation, in the first place, we suggest an MEG spatial filtering method in spherical harmonics domain that can capture the activity arising from deep sources as well as superficial ones. Our approach decomposes the MEG signal localized to inside the head by a recent method called "signal space separation" to

an intraparenchymal signal using a beamspace technique. Signal space separation (SSS), provided first by Taulu and Kajola [10], is a technique designed principally for removing external interferences from MEG measurements. Utilizing a fundamental law of physics, the SSS method decomposes the recorded magnetic field into two parts using vector spherical harmonic basis functions: one for the signals coming from the inside the sensor array volume and the other coming from the outside it. We show that the signal component obtained by the SSS method can be further decomposed by a simple operation into signals originating from deep and superficial sources within the brain. The beamspace method yields a linear transformation matrix in order to maximize the power of the source space of interest and hence guarantees to obtain the optimality in mean-square sense for the modification of the SSS coefficients.

The deep and superficial sources are meant to be with respect to the SSS expansion origin, which is obtained by fitting a hypothetical spherical shell to the sensor array volume. It is not straightforward to apply the aforementioned method to spatially filter the signal for arbitrarily located spherical regions of interests in the head space. Hence, in the second place, we demonstrate a generalization of our method for any selected origin inside the head space eliminating the restriction of it to the SSS expansion origin.

While there have been attempts for the separation of the signals according to specified regions, our proposed methods are unique by realizing the filters in the spherical harmonics domain, which results simple manipulations of the so-called multipole coefficients. Unlike the traditional spatial filtering methods, our approach does not need to divide the source space into thousands of grids and obtain the filtering effect by a discrete numerical computation. This simplicity and the efficiency of the derived formulations stem from their natural appropriateness to the spherical domain and the orthogonality properties of the SSS basis functions that are directly related to the vector spherical harmonics.

1.2 THESIS OUTLINE

This thesis is organized as follows. Chapter 2 provides the background for the development of the proposed methods by briefly describing the forward and inverse problems of MEG. Chapter 3 presents the novel spatial filtering techniques in the spherical harmonics domain called as exSSS and genexSSS with the brief introductions of the SSS and the beamspace methods. In Chapter 4, we demonstrate some results of the experiments using simulated and real data in order to show the validity of the proposed spatial filtering methods. Finally, Chapter 5 summarizes the properties of the methods by comparing them to the other spatial filtering methods in the literature and discusses some potential situations encountered while using the developed methods.

2.0 THEORETICAL BACKGROUND

When a physical system is considered, we can conceive it in three steps as pointed out in [11]. First, the system should be parameterized such that these parameters give rise to physical measurements. In the case of MEG, the parameters are mainly current source magnitudes, locations and orientations. The second step consists of forward modeling, which corresponds to making predictions on the measurements for a given value of these parameters. These first two steps can be considered generally as inductive [11]. The third step, which is deductive, is called inverse modeling. It relies on estimating the values of the parameters from the actual measurements. Since in practice we have only the measurements as the output of the physical system, the third step is the one that is addressed in real life, while the former two steps are used as supplements to solve the inverse problems. In the following sections, we present the mainstream forward modeling methods and inverse methods, in particular for MEG.

2.1 FORWARD PROBLEM

2.1.1 Mapping from source space to MEG space

Mapping from current sources to the magnetic fields in a noiseless environment can be described as

$$b_k(t) = \int_{\Omega} \mathbf{h_k}(\mathbf{r}').\mathbf{j}(\mathbf{r}')d\Omega \tag{2.1}$$

where Ω is the whole source space, $\mathbf{r}'$ stands for the source locations and $\mathbf{h_k}$ is the lead-field mapping of the current sources $\mathbf{j}$ to the magnetic field measurements at the k^{th} ($k =$

$1, 2, \ldots, M$) sensor, denoted as $b_k(t)$. The leadfields correspond to the forward solution, which is realized using locations and orientations of the current sources and locations and orientations of the sensors according to Biot-Savart law, which is explained in detail in Section 2.1.2. Then, the MEG data vector can also be expressed as

$$\mathbf{b} = [b_1, b_2, \ldots, b_M]^{\mathrm{T}} = \int_{\Omega} \mathbf{H}(\mathbf{r}')\mathbf{j}(\mathbf{r}')d\Omega \tag{2.2}$$

where $\mathbf{H}(\mathbf{r}') = [\mathbf{h}_1(\mathbf{r}'), \mathbf{h}_2(\mathbf{r}'), \ldots, \mathbf{h}_M(\mathbf{r}')]^{\mathrm{T}}$ denotes the $(M \times 3)$ matrix of leadfields for all M sensors. The forward problem can be defined briefly as computing the magnetic field outside the head from a given primary source distribution within the brain. It consists of different formulations depending on the selected head model, such as homogenous medium, piecewise homogenous conductor or spherically symmetric conductor model [1], [2]. Note that once the conductivity of the medium is specified, the forward problem yields a unique output for a given source distribution.

2.1.2 Use of Quasistatic Approximation of Maxwell's Equations

Electrical activity in the neurons is typically below 1 KHz, which makes the use of the quasistatic approximation of Maxwell's equations

$$\nabla \times \mathbf{E} = \mathbf{0} \tag{2.3}$$

$$\nabla \times \mathbf{B} = \mu_0 \mathbf{j} \tag{2.4}$$

$$\nabla \cdot \mathbf{E} = \rho/\epsilon_0 \tag{2.5}$$

$$\nabla \cdot \mathbf{B} = 0 \tag{2.6}$$

legitimate for the forward computations. This means that one does not have to take into account the terms that contain the derivatives with respect to the time parameter. Here, $\mathbf{E}$ is the electrical field, $\mathbf{B}$ is the magnetic field, $\mathbf{j}$ is the current density and ρ is the charge density. The permeability and permittivity of the head tissue denoted by μ and ϵ, respectively, are taken as fixed by assigning them values equivalent to those of free space, that is $\mu = \mu_0$ and $\epsilon = \epsilon_0$.

Since the magnetic field is divergence-free, it can always be defined as the curl of a vector field

$$\mathbf{B} = \nabla \times \mathbf{A} \tag{2.7}$$

where $\mathbf{A}$ is called the magnetic vector potential in electromagnetics. Notice that this definition of $\mathbf{A}$ is not unique since one can add arbitrary curl-free components $\nabla\chi$ to $\mathbf{A}$ [12]:

$$\mathbf{A} \rightarrow \mathbf{A} + \nabla\chi. \tag{2.8}$$

This arbitrariness for the choice of $\mathbf{A}$ is called gauge freedom or gauge invariance [13]. If Equation (2.7) is substituted in (2.4) with the use of a vector identity, we obtain:

$$\nabla \times (\nabla \times \mathbf{A}) = \nabla(\nabla \cdot \mathbf{A}) - \nabla^2\mathbf{A} = \mu_0\mathbf{j}. \tag{2.9}$$

We use the usual gauge, called Coulomb gauge (or transverse gauge), where the divergence of $\mathbf{A}$ is accepted to be null [13], [12]. Then equation (2.9) reduces to a three dimensional Poisson's equation, i.e., Poisson's equation in all three dimensions of $\mathbf{A}$:

$$\nabla^2\mathbf{A} = -\mu_0\mathbf{j} \tag{2.10}$$

Poisson's equation can be solved using Green's function method [14]. The Green's function $G(\mathbf{x}, \mathbf{y})$ is defined as a function satisfying the following two conditions:

$$G(\mathbf{x}, \mathbf{y}) = G(\mathbf{y}, \mathbf{x}) \tag{2.11}$$

$$\nabla^2 G(\mathbf{x}, \mathbf{y}) = \delta(\mathbf{x} - \mathbf{y}) \tag{2.12}$$

where $\delta(.)$ is the Dirac delta function. These two properties allow the solution of a Poisson's equation $\nabla^2 u(\mathbf{x}) = \vartheta(\mathbf{x})$ to be

$$u(\mathbf{x}) = \int_V G(\mathbf{x}, \mathbf{y})\vartheta(\mathbf{y})d\mathbf{y}. \tag{2.13}$$

which can be easily verified by substituting (2.12) into the general Poisson's equation. Here, V denotes the whole source space. One can also show [14] that the two conditions (2.11) and (2.12) are satisfied if one chooses the Green function as

$$G(\mathbf{x}, \mathbf{y}) = -\frac{1}{4\pi\|\mathbf{x} - \mathbf{y}\|}. \tag{2.14}$$

Then the solution to the general Poisson's equation finally is

$$u(\mathbf{x}) = \int_V -\frac{1}{4\pi}\|\mathbf{x}-\mathbf{y}\|\vartheta(\mathbf{y})d\mathbf{y}. \tag{2.15}$$

By applying this general result to equations (2.10) and (2.7), we reach the well-known Biot-Savart law

$$\mathbf{B}(\mathbf{r}) = \nabla \times \mathbf{A} = \frac{\mu_0}{4\pi}\int_V \frac{\nabla' \times \mathbf{j}(\mathbf{r}')}{\|\mathbf{r}-\mathbf{r}'\|}dv' \tag{2.16}$$

which provides the mapping relation of the current sources $\mathbf{j}(\mathbf{r}')$ to the magnetic field $\mathbf{B}(\mathbf{r})$ measured at the location $\mathbf{r}$. The leadfields given in (2.1) can be obtained using this fundamental law. Equation (2.16) can be rewritten in another form using vector calculus identities:

$$\mathbf{B}(\mathbf{r}) = \frac{\mu_0}{4\pi}\int_V \frac{\mathbf{j}(\mathbf{r}') \times (\mathbf{r}-\mathbf{r}')}{\|\mathbf{r}-\mathbf{r}'\|^3}dv'. \tag{2.17}$$

The current source $\mathbf{j}(\mathbf{r}')$ is considered to consist of two parts: the primary current $\mathbf{j}^p(\mathbf{r}')$ reflecting the neuronal activity and the secondary current $\mathbf{j}^s(\mathbf{r}')$ resulting from the electrical fields on charge carriers in the source volume:

$$\mathbf{j}(\mathbf{r}') = \mathbf{j}^p(\mathbf{r}') + \mathbf{j}^s(\mathbf{r}') \tag{2.18}$$

$$\mathbf{j}^s(\mathbf{r}') = \sigma(\mathbf{r}')\mathbf{E}(\mathbf{r}') = -\sigma(\mathbf{r}')\nabla V(\mathbf{r}') \tag{2.19}$$

where $\sigma(\mathbf{r}')$ is the conductivity of the head tissue. It is typically accepted as constant and isotropic within specified regions of the brain like scalp, skull, cerebrospinal fluid, gray matter and white matter. Taking $\sigma(\mathbf{r}') = 0$ everywhere in the source space corresponds to the unbounded homogenous conductor model and in this case, it is easy to see from equations (2.17) and (2.19) that only the primary current $\mathbf{j}^p(\mathbf{r}')$ contributes to the magnetic field. Then the solution to the forward problem becomes easy and straightforward. However, it is obvious that taking $\sigma(\mathbf{r}')$ as constant everywhere is too unrealistic for an accurate computation of the magnetic fields.

The spherically symmetric conductor is frequently used and generally accepted as a physically appropriate head model for MEG. This model assumes that the source volume is bounded and it is comprised of concentric spherical volumes that have different conductivity profiles. It was analytically shown that [15] this model proves not to be susceptible to the

secondary currents and hence one does not need the explicit knowledge of the conductivity profiles in the head in order to solve the forward problem. It is worth noting that this is not the case for EEG, i.e., for spherically symmetric head models, unlike MEG, one needs to take the conductivities into account for the EEG forward solutions. This is one of the most important properties that makes MEG a superior tool to identify the primary currents. Moreover, Sarvas's formula [15] reveals that MEG is fundamentally produced by the tangential currents and it is almost blind to the radial currents, which is another main difference from EEG. It was shown that a spherically symmetric model is significantly adequate for accurate results in the MEG forward computations [3]. Nevertheless, one may desire to utilize realistic head models which are dependent upon anatomical information obtained from brain images using magnetic resonance (MR) or computer tomography (CT) imaging. In this case, apart from surface extraction, one also needs to determine the conductivity profiles of the specified regions from these images in order to solve the forward problem numerically by the boundary element method (BEM) [16] or the finite element method (FEM) [17]. Accordingly, utilizing a realistic head model demands a considerable amount of time and care for finding solutions to the forward problem, and this can especially cause difficulty for the inverse methods, for which one has to compute the magnetic fields iteratively [2].

2.2 INVERSE PROBLEM

2.2.1 Linear algebraic formulation

For M sensors and N discrete sources in the brain space, one can also express the relation between magnetic field measurements and the leadfields in (2.2) in discrete algebraic form:

$$\begin{aligned}
\mathbf{b} &= \begin{bmatrix} b_1(t) \\ . \\ . \\ . \\ b_M(t) \end{bmatrix} = \begin{bmatrix} L(r_1, r_{q1}, \mu_1) & \dots & L(r_1, r_{qN}, \mu_N) \\ . & \dots & . \\ . & \dots & . \\ . & \dots & . \\ L(r_M, r_{q1}, \mu_1) & \dots & L(r_M, r_{qN}, \mu_N) \end{bmatrix} \begin{bmatrix} q_1(t) \\ . \\ . \\ . \\ q_N(t) \end{bmatrix} \\
\mathbf{b} &= \mathbf{LQ}
\end{aligned} \tag{2.20}$$

where $\mathbf{b}$ is an $(M \times 1)$ dimensional magnetic signal vector, $\mathbf{Q}$ is the vector of source magnitudes,μ_j is the orientation vector, r_{qj} is the location of the j^{th} source $(j = 1, 2, \dots, N)$,r_k is the location of the k^{th} sensor and $\mathbf{L}$ is the so-called leadfield matrix, an $(M \times N)$ dimensional matrix, whose $(k, j)^{th}$ component is $L(r_k, r_{qj}, \mu_j) = \mathbf{h_k}(r_{qj}) \cdot \mu_j$.

2.2.2 Ill-posedness

According to a definition proposed by Hadamard in 1902, a problem is accepted to be well-posed if it satisfies the following three conditions [18]:

1. *Existence*: For every input to the problem, there should be an output.
2. *Uniqueness*: The solution of the problem should be unique.
3. *Continuity*: The mapping between the solution and the data should be continuous.

If any of these conditions is not fulfilled, the problem is defined to be ill-posed.

The number of sources in the brain N is naturally much larger than the number of MEG sensors M. Hence it can be inferred from (2.20) that the currents in the null space of the leadfield matrix $\mathbf{L}$ do not contribute to the magnetic field measurements. In other words,

the source vector $\mathbf{Q}$ can have any arbitrary part $\mathbf{Q_2}$, which is orthogonal to the lead field matrix $\mathbf{L}$ as:

$$\mathbf{Q} = \mathbf{Q_1} + \mathbf{Q_2},\ \mathbf{b} = \mathbf{LQ} = \mathbf{LQ_1} + \mathbf{LQ_2}$$
$$\mathbf{LQ_1} = \mathbf{b},\ \mathbf{LQ_2} = \mathbf{0} \tag{2.21}$$

and this leads to the evidence that even in a noiseless environment, the MEG inverse problem to estimate the source parameters (such as locations, magnitudes) is non-unique [19], [1] that is, it does not satisfy the second condition and hence it is ill-posed. Besides, it has been shown that [15] the radial parts of the currents do not contribute to the measured MEG data for spherically symmetric conductors, which implies the ill-posedness of the problem also stemming from the physics of MEG. Hence, a priori knowledge of the sources is definitely required for accurate source estimation by the inverse methods.

2.2.3 Common Methods for MEG

The inverse methods for MEG are considered to be in three classes [1], [2]: parametric modeling, which is also referred as dipole fitting, distributed source modeling and scanning based methods.

2.2.3.1 Dipole fitting Dipole fitting is the most preferred technique for clinical purposes. It assumes a number of sources as p and utilizes a nonlinear optimization algorithm in order to minimize the squared error between the MEG signal and the field data computed from the forward modeling for the sources. This method has some pitfalls such as selecting the true number of sources p. It is also noteworthy that the optimization gets more complex for large p and this may result in undesired solutions trapped to local minima of the cost function [2].

2.2.3.2 Distributed source modeling Unlike dipole fitting, the distributed source modeling techniques assume a large number of fixed sources that are located on discrete grids. The leadfield matrix $\mathbf{L}$ becomes fixed depending on the determined grids and hence the problem becomes linear and computationally simpler. Since the number of grids is much larger than the number of sensors M, the problem is underdetermined by nature in these techniques and the solution directly depends on the imposed a priori knowledge on the source vector $\mathbf{Q}$. These techniques can be mainly classified under minimum-norm (MN) approaches and probabilistic approaches.

The source space consists all the vectors $\mathbf{Q}$ that satisfy (2.20). The MN approaches basically select the source estimate $\hat{\mathbf{Q}}$ that has the minimum norm in the solution space. In general, this can be expressed by

$$\min(\hat{\mathbf{Q}} - \mathbf{Q_0})^{\mathrm{T}} \mathbf{C_Q} (\hat{\mathbf{Q}} - \mathbf{Q_0}) \quad \text{subject to} \quad \mathbf{L}\hat{\mathbf{Q}} = \mathbf{b} \tag{2.22}$$

where $\mathbf{Q_0}$ denotes an a priori approximate of the solution and $\mathbf{C_Q}$ is a positive definite weighting matrix that represents the approximate correlations between sources. In this case, the general MN solution can be easily shown to be

$$\hat{\mathbf{Q}}_{genMN} = \mathbf{Q_0} + {\mathbf{C_Q}}^{-1}\mathbf{L}^{\mathrm{T}}(\mathbf{L}{\mathbf{C_Q}}^{-1}\mathbf{L}^{\mathrm{T}})^{-1}(\mathbf{b} - \mathbf{L}\mathbf{Q_0}) \tag{2.23}$$

by the Lagrange multipliers method [19].

If one does not impose any a priori knowledge on the solution, i.e., $\mathbf{Q_0} = \mathbf{0}$ and $\mathbf{C_Q} = \mathbf{I}$, the solution is basically the multiplication of the Moore-Penrose inverse of the leadfield matrix by the measurement vector $\mathbf{b}$:

$$\hat{\mathbf{Q}}_{MN} = \mathbf{L}^{+}\mathbf{b} = \mathbf{L}^{\mathrm{T}}(\mathbf{L}\mathbf{L}^{\mathrm{T}})^{-1}\mathbf{b} \tag{2.24}$$

as can be seen from the given general equation in (2.23). One can easily show that [19] the MN estimate $\hat{\mathbf{Q}}_{MN}$ does not contain any part belonging to the null space of $\mathbf{L}$.

Methods based on MN approaches are distinguished by some variations on the minimization of the norm of the source currents. These variations should be considered in two ways: i) selection of the weighting matrix $\mathbf{C_Q}$, ii) using a different norm degree.

A standard way to determine the weighting matrix is to assign the norm of the leadfields at a particular source location to its diagonal elements:

$$\mathbf{C_Q} = diag\{\|\mathbf{L}_1\|, \ldots, \|\mathbf{L}_N\|\} \tag{2.25}$$

where $\mathbf{L}_j$ denotes a column of $\mathbf{L}$ and $j = 1, \ldots, N$. This weighting matrix can be used in order to remove the bias towards grids on superficial layers [1], [20]. Another very popular MN based inverse method called low-resolution electromagnetic tomography (LORETA) [21] suggests utilizing the discrete spatial Laplacian operator for the weighting matrix as a way of source depth compensation. One can also change the weighting matrix iteratively by taking into account the estimated source vector in the previous iteration [22]. Another well-known method called "focal underdetermined system solver" (FOCUSS) [23] aims at obtaining sparse (and hence focal) solutions by changing the weighting matrix iteratively. The change of the weighting matrix is based on the generalized affine scale transform [23]. The FOCUSS method needs a "good" initial source estimate for a convergence to a focal estimate. Hence there have been successful hybrid uses of it by taking the LORETA estimate as an initial point to the iterations in EEG/MEG literature [24], [25]. The hybridity in these methods enables the estimation of both focal high-resolution required sources and distributed low-resolution required sources.

One of the typical weak points of general MN is that its estimates are too smooth, because of the implicit assumption of Gaussian probability distribution of the sources. Other norm degrees less than 2 are used to obtain more focal and robust source estimates. Minimum current estimate (MCE) [20] is such a method that minimizes the L1 norm of the source vector $\mathbf{Q}$ instead of the L2 (Euclidean) norm. This corresponds to minimizing the sum of the absolute values of source magnitudes. Unfortunately, the solution of L1 norm minimization is not as straightforward as in the case of L2 MN. Thus, the MCE method typically uses a linear programming (LP) scheme which makes it much more computationally demanding. Besides, the MCE optimization requires the dipole orientations at each grid, which can be estimated using MR images or one can use the orientations of the classical MN source estimates [20]. The side effect of MCE is unrealistic focality, i.e., the estimated source activity changes abruptly from one grid to another. In [26], the authors suggest a method

called vector-based spatial temporal analysis (VESTAL), which adds temporal information of data to L1 norm minimization in order to prevent the poor smoothing effect of MCE. This is handled simply by projecting the MCE result to the signal subspace using singular value decomposition (SVD) of the measurements. In [27], a probabilistic approach is siggested to determine an optimal norm degree P taking a value between 1 and 2 for more accurate source identification. Thus, this might help to escape from overly smooth source estimates by $P = 2$ (L2 MN) and too focal estimates by MCE (L1 MN). The optimal degree value P depends on the grid discretization size and the data itself.

One can employ probabilistic approaches to interpret and solve inverse problems. Bayesian methodology relies on maximizing the so-called posteriori probability

$$p(\mathbf{Q}|\mathbf{b}, \xi) = \frac{p(\mathbf{b}|\mathbf{Q}, \xi)p(\mathbf{Q}|\xi)}{p(\mathbf{b}, \xi)} \tag{2.26}$$

that corresponds to the probability of the model accuracy given the data and any prior information ξ [2], [19], [28]. Here $p(\mathbf{Q}|\xi)$ is called the prior probability, which represents the statistical knowledge about the sources and $p(\mathbf{b}|\mathbf{Q}, \xi)$ is called the likelihood, which reflects the probability of the data as a consequence of a given source (forward problem). In practice, the maximization is realized on the logarithm of the posteriori probability to simplify the computations:

$$\hat{\mathbf{Q}} = \arg\max_{\mathbf{Q}} \log p(\mathbf{b}|\mathbf{Q}, \xi) + \log p(\mathbf{Q}|\xi) \tag{2.27}$$

where $p(\mathbf{b}, \xi)$ is taken out, since it acts as a normalization constant.

The Bayesian methodology is useful especially for incorporating a priori knowledge of data and model explicitly and understanding the applicability and characteristics of the particular inverse problem under consideration [11], [28]. For instance, in [29], they derive both least-squares EEG/MEG dipole fitting and independent component analysis (ICA) using a Bayesian formulation. This reveals the implicit assumptions under these source identification methods and allows developing other methods by modifying these assumptions appropriately. If the prior probability $p(\mathbf{Q}|\xi)$ and the likelihood $p(\mathbf{b}|\mathbf{Q}, \xi)$ are taken as Gaussian distributions, the maximization of the posterior probability corresponds to L2 MN source estimation [2], [19], [20]. If the prior probability is accepted to be exponential distribution instead of Gaussian, the Bayesian estimation becomes equivalent to MCE [20].

Thus, one can interpret or produce various MN methods based on Bayesian methodology. In [30], they incorporate some temporal and spatial constraints to the prior probability. The spatial constraints are managed through the gradients of some nonlinear functions of the Lorentzian form, in order to allow the preservation of necessary local discontinuities of sources. The level of the discontinuity is achieved through a parameter, which is computed adaptively through iterations. The temporal constraints are imposed by the assumption of slow change of dipoles with respect to the sampling frequency. This is implemented by weighting the source dipoles with the orthogonal projection of the previous temporal samples of the estimated source. It was shown that addition of these constraints to the prior probability and maximizing the obtained posterior probability using an iterative procedure may lead to improved reconstructed source waveforms and spatial resolutions when compared with LORETA. Not only do the Bayesian methods allow the solution of inverse problems, but they also help to extract useful information such as in [31], where they use the Bayesian approach in order to estimate EEG source localization error bounds and total information of EEG data in terms of entropy.

2.2.3.3 Scanning methods These methods rely on estimating one source at a grid and scanning the whole source region afterwards. We briefly mention the two most popular scanning methods called beamformers and multiple signal classification (MUSIC).

Known as Capon's method [32] in traditional spectrum estimation, beamformers have also been popular for tackling EEG/MEG inverse problems [33], [34]. Linearly constrained minimum variance (LCMV) beamforming is based on the principle of passing the signals at a source location and attenuating the signals coming from elsewhere. This is realized by Capon's own methodology in [32], which minimizes the source power $P_{\mathbf{W}_d} = \mathbf{W}_d \mathbf{R}_b {\mathbf{W}_d}^{\mathrm{T}}$ under the unity constraint $\mathbf{L}_d^{\mathrm{T}} \mathbf{W}_d = 1$, where $\mathbf{W}_d$ is the LCMV beamforming filter, $\mathbf{L}_d$ is the leadfield at a desired location r_d, and $\mathbf{R}_b$ is the autocorrelation matrix of data. When this optimization problem is solved by the Lagrange multipliers technique, the LCMV beamforming filter for the location r_d can be obtained through

$$\mathbf{W}_d = \frac{{\mathbf{R}_b}^{-1} \mathbf{L}_d}{{\mathbf{L}_d}^{\mathrm{T}} {\mathbf{R}_b}^{-1} \mathbf{L}_d} \tag{2.28}$$

and then the source signal is estimated at that particular location $\hat{\mathbf{Q}}_{LCMV} = \mathbf{W}_d^{\mathrm{T}}\mathbf{b}$. LCMV is classified as an adaptive method, since it depends upon estimating the autocorrelation matrix from the measurements.

One can show that while the constraint makes the LCMV beamforming filter pass the signals from r_d, the minimization blocks the signals from all other sources r_k where $k \neq d$ and $k = 1, \ldots, d-1, d+1, \ldots, N$ [35]. The major disadvantage of LCMV beamforming is its weakness in estimating correlated sources. The blocking capability of the filter depends on the correlation between sources and hence any correlation causes a leakage coming from the other sources, which distorts the filter output or source estimate $\hat{\mathbf{Q}}_{LCMV}$ [35].

MUSIC is a well-known array signal processing technique being used for the MEG source identification problem for the first time in [36]. It separates the total signal space into noise and signal subspaces by eigendecomposition of the autocorrelation of the measured signal

$$\mathbf{R}_b = \boldsymbol{\varphi}\boldsymbol{\Lambda}\boldsymbol{\varphi} = [\boldsymbol{\varphi_s}\boldsymbol{\varphi_n}] \begin{bmatrix} \boldsymbol{\Lambda_s} & \\ & \boldsymbol{\Lambda_n} \end{bmatrix} [\boldsymbol{\varphi_s}\boldsymbol{\varphi_n}]^{\mathrm{T}} \tag{2.29}$$

where $\boldsymbol{\Lambda_s}$ is the diagonal matrix of the largest eigenvalues, $\boldsymbol{\varphi_s}$ is the corresponding eigenvector matrix, $\boldsymbol{\Lambda_n}$ is the diagonal matrix of the remaining smallest eigenvalues and $\boldsymbol{\varphi_n}$ is the corresponding eigenvector matrix. Here $\boldsymbol{\varphi_s}$ is said to span the signal subspace while $\boldsymbol{\varphi_n}$ spans the noise subspace, which is orthogonal to the signal subspace.The sources are considered to be located where the leadfield $\mathbf{L}_d$ is orthogonal to the noise subspace. Thus, by a grid search, the source locations are identified according to a cost function

$$C(r_d) = \frac{\|\boldsymbol{\varphi_n}\boldsymbol{\varphi_n}^{\mathrm{T}}\mathbf{L}_d\|^2}{\|\mathbf{L}_d\|^2} \tag{2.30}$$

where $d = 1, \ldots, N$. Unlike LCMV beamformer, MUSIC does not require uncorrelation but linear independency between sources. However, it is reported to fail when there is correlation between sources for noisy data [2].

There have been attempts to show that all these linear inverse problem approaches converge to similar results without any specific a priori information about the source and the signal spaces [19], [37].

3.0 SPATIAL FILTERING TECHNIQUES

When an MEG system receives signals arising from various locations, classical temporal filtering may not be an appropriate tool to obtain the desired signal belonging to the region of interest (ROI). For instance, the interferences to be filtered out may have similar temporal characteristics or they may have common temporal frequency bands with the desired part [38]. Spatial filtering of MEG can be defined as an attempt to preserve or enhance the part of the signal that corresponds to a defined desired spatial property, while suppressing the parts being produced by the unwanted activity.

3.1 INTRODUCTION

3.1.1 Noise removal

Since the magnetic fields of brain are extremely weak, noise removal is great interest of various spatial filtering methods. In this case, the unwanted activity can be described under terms such as environmental noise (electrical power lines, elevators, etc.), biological noise (eye blink, heart beat, muscle movement, brain background activity, etc.) and sensor noise. Among these methods, the signal space projection (SSP) [39],[40] is a popular one that aims at removing the contributions of the undesired sources or artifacts by exploiting their spatial structure. The removal of the artifacts is handled through composing projection operators by the aid of SVD of some estimated artifact and/or source component vectors. In general, the desired part of the signal is not orthogonal to the artifact component, thus applying the principle of orthogonality in this approach introduces a distortion in the signal space.

This possible distortion should be taken into account for the source modeling after the SSP is applied to the data. Additionally, the accurate estimate of the spatial templates of the artifacts or the interesting sources is crucial for the accuracy of the SSP transformed data. The effect of SSP to the source localization based on the spatial template pattern is examined in detail in [41]. In [42], they also proposed a similar approach to SSP, by the addition of taking into account the possible delays and nonlinear transforms of the artifact component vectors. These vectors were defined to represent only the environmental noise and estimated by the reference channels used also in other works [43]. It is obvious that using reference channels is legitimate if these channels are solely sensitive to the noise but not to the brain sources.

Popular and efficient signal processing methods such as independent component analysis (ICA) [44],[45],[46],[47], adaptive filtering [48] and nonlinear Wiener filtering [49] have also been employed for the rejection of various artifacts. The main drawback of these techniques is that they often suffer from unrealistic assumptions about spatiotemporal data characteristics like independence and uncorrelatedness.

3.1.2 Constraining signal to a region of interest

As in the case of beamspace methods [50], one could also define a specific region of interest (ROI) inside the head space in order to enhance the signals arising from there while suppressing the ones arising from out of the ROI. Then the external noise elimination mentioned in the previous subsection corresponds to selecting the ROI as the whole head source space.

As it is pointed out in [51], the spatial filtering and the inverse problem can be studied from the signal processing point of view, if they are considered in analogy with the well-known spectrum estimation problem:

$$x_t = \int_{-1/2}^{1/2} e^{2\pi f t} X(f) df \tag{3.1}$$

If $b_k(t)$ is considered analogous with the time samples x_t, then the leadfield matrix would correspond to complex sinusoidals and the current sources would be analogous to Fourier coefficients, which give rise to spectrum estimates. With the same analogy, while the inverse

problem corresponds to the spectrum estimation; the spatial filtering would be designing a filter that passes the specified band $[a, b]$, where $0 < a < b < \pi$ and attenuates the frequency outside it. Accordingly, it is the complexity of the kernel and the three dimensionality of the location parameter that makes the MEG inverse problem more difficult and challenging than the spectrum estimation.

3.1.2.1 Obtaining deep structures Deep sources in the brain are of great importance to studies related to memory, emotions, motor controls and disorders like Parkinson, Alzheimer, Huntington and epilepsy [52]. However, a great amount of contribution to the MEG measurements arises from the superficial cortical areas because of their closeness to the sensors and their anatomical structures composed of pyramidal cells producing strong excitatory postsynaptic potentials [1], [2]. In [52], they presented an anatomical model of deep brain structures with the support of an experimental study that gives evidence to the possible detection of these structures from MEG. There have also been some other various attempts to detect the sources arising from deep areas of the brain, such as brainstem, thalamus, hippocampus and cerebellum [6], [7], [39], [9]. However, the nature of these studies was experimental and their success was highly dependent on the signal quality and the utilization of a realistic head model such as boundary element method for the forward calculations. By selecting an ROI inside the head, spatial filtering may be a useful way to reveal the deep source activities in the brain. We demonstrate a novel spatial filtering method [53], [54] that we call exSSS developed in particular for deep and superficial regions in Section 3.4.1 and 3.4.2.

3.1.2.2 Dimension reduction One another fundamental motive behind filtering the signal to an ROI is that its dimension is reduced. Then the source localization problem is expected to be less ill-posed and less computationally demanding since the solution space is shrunk [50], [55], [56]. For instance, as one of the widely known inverse methods, the linearly constrained minimum variance beamformers may yield severe source localization errors for correlated sources [35]. Spatial filtering the signal into regions that do not have

strong correlated source activity may prevent this flow of the method. Other benefits of the spatial filtering include monitoring the activity for a specified region, which is a common practice for tomographic neurofeedback or brain computer interfaces [57], [58].

3.1.2.3 Data independency Many classical spatial filtering techniques such as SSP, ICA, vector beamformers [59] utilize the data characteristics for the design of the filters. Even if one has the accurate knowledge of some spatiotemporal template or spectral structure of the interference, any possible spatiotemporal similarity between the desired signal and unwanted signal is expected to cause a signal loss or improper separation and loss of statistical variability for the source localization techniques [55]. In these cases, exploiting the physical knowledge of the system that maps the unknown sources to the observed data might be a more realistic and safe way. We are calling such designs as "data-independent spatial filters". For instance, in [57], data-independent filters are designed based on standardized low-resolution electromagnetic tomography (sLORETA) coupled with beamspace methodology. The signal space separation (SSS) method [10],[60] is such a data-independent filtering technique. It separates the magnetic field measurements into two parts corresponding to the sources inside the sensor array and to those outside it. Utilizing Maxwell equations, and representing these parts with vector spherical harmonics, the SSS accomplishes removing the external interferences from the MEG measurements without imposing unrealistic assumptions. The details of the SSS method are given in the next section. In Sections 3.3 and 3.4, we demonstrate an extension of the SSS method to spatially filter the signal into ROI's inside the head. While all aforementioned methods (except SSS) utilize the classical leadfields, our approach differs as taking advantage of the vector spherical harmonics and its orthogonality properties by a simple manipulation of the SSS coefficients using a beamspace method. Moreover, the representation in the spherical harmonics domain avoids the need of discretizing the source space into grids for the computation of the leadfields and gives rise to a filtering that can be achieved inside the sensor array.

3.2 SIGNAL SPACE SEPARATION (SSS) METHOD

The SSS is a recent method that separates the magnetic field measurements into two parts corresponding to the sources inside the sensor array and to those outside it. The method only takes the sensor geometry and an expansion origin into account without requiring any data dependency in general. We explain the details of the derivation of the SSS in the following.

In the modern MEG devices, the magnetic fields are measured non-invasively by the SQUID sensors, which are located 2-4 cm from the skull. Hence, these sensors may be assumed to be on a source-free region, i.e., they contain neither the internal brain sources nor the external interferences. This causes one of the fundamental quasistatic Maxwell's equations $\nabla \times \mathbf{B} = \mu_0 \mathbf{j} = \mathbf{0}$. Then, the magnetic scalar potential U can be used to describe the magnetic field that is produced by current sources inside and outside the head as $\mathbf{B} = -\mu_0 \nabla U$,which is valid only if and only if the measurement space is source-free by Ampere's law [12]. Since the magnetic field is divergence free ($\nabla \cdot \mathbf{B} = 0$), then U must satisfy the Laplace's equation:

$$\nabla \cdot \mathbf{B} = -\mu_0 \nabla \cdot (\nabla U) = \nabla^2 U = 0 \tag{3.2}$$

The solutions of (3.2) are called harmonic functions. It is well-known that the Laplace's equation in the spherical coordinates

$$\nabla^2 U = \frac{1}{r^2}\frac{\partial U}{\partial r}\left(r^2 \frac{\partial U}{\partial r}\right) + \frac{1}{r^2 \sin\theta}\frac{\partial^2 U}{\partial \phi^2} + \frac{1}{r^2 \sin\theta}\frac{\partial U}{\partial \phi}\left(\sin\theta \frac{\partial U}{\partial \phi}\right) = 0 \tag{3.3}$$

can be solved using the separation of variables by expressing the solution U as the multiplication of three independent functions each of which depends on only one separate spherical coordinate:

$$U(r, \theta, \phi) = R(r)\Theta(\theta)\Phi(\phi) \tag{3.4}$$

where r is the radial distance, θ is the polar angle ranging from $0 \leq \theta \leq \pi$ and ϕ is the azimuthal angle ranging from $0 \leq \phi < 2\pi$. By substituting (3.4) into (3.3) and solving the second-order differential equations, the general solution at a location $\mathbf{r} = (r, \theta, \phi)$ can be obtained as:

$$U(\mathbf{r}) = \sum_{l=0}^{\infty} \sum_{m=-l}^{l} \alpha_{lm} \frac{Y_{lm}(\theta, \phi)}{r^{l+1}} + \sum_{l=0}^{\infty} \sum_{m=-l}^{l} \beta_{lm} r^l Y_{lm}(\theta, \phi). \tag{3.5}$$

As it is observed from (3.5), the solution is mainly based on the superpositions of the function $Y_{lm}(\theta, \phi)$ so-called as normalized spherical harmonic function ("spherical" implies the coordinate system and "harmonic" implies that it is a solution of Laplace's equation) with differing degrees l and orders m:

$$Y_{lm}(\theta, \phi) = \sqrt{\frac{2l+1}{4\pi}\frac{(l-m)!}{(l+m)!}} P_{lm}(\cos\theta) e^{im\phi} \tag{3.6}$$

where $P_{lm}(.)$ denotes the associated Legendre function. The associated Legendre function is a special function, which is a solution of a second-order differential equation, named as general Legendre equation:

$$(1-x^2)y'' - 2xy' + \left[l(l+1) - \frac{m^2}{1-x^2}\right] y = 0. \tag{3.7}$$

This equation has nonsingular solutions for $x = (-1, 1)$ only if l and m are integers such that $-l \leq m \leq l$. The Laplace's equation is known to be unique [13] for a volume V bounded by a surface S. In other words, there is only one solution U that satisfies $\nabla^2 U$ with the given values of U on S. The uniqueness theorem can be easily proved by assuming two solutions U_1 and U_2 and then showing that $U_1 = U_2$. If we define a third function $U_3 := U_1 - U_2$, according to the aforementioned assumptions

$$\begin{aligned} \nabla^2 U_1 &= 0,\ \nabla^2 U_2 = 0 \\ \nabla^2 U_3 &= \nabla^2 U_1 - \nabla^2 U_2 = 0 \end{aligned}$$

by the linearity of Laplace operator and it gives zero on the boundary surface:

$$U_3(S) = U_1(S) - U_2(S) = 0.$$

Hence, U_3 is also harmonic, i.e., it satisfies the Laplace's equation and it is zero on the boundary S as well. Since both minima and maxima of an harmonic function have to lie on the boundary[13], $U_3 = 0$ should also be satisfied everywhere inside the volume V. As a result, $U_1 = U_2$ is valid everywhere inside V, which finally concludes the uniqueness of the solution U in V.

By utilizing the uniqueness theorem, we can show that the first part of (3.5) $U_{in}(\mathbf{r}) = \sum_{l=0}^{\infty}\sum_{m=-l}^{l}\alpha_{lm}\frac{Y_{lm}(\theta,\phi)}{r^{l+1}}$ corresponds to the magnetic scalar potential stemming from the inner sources with $\|\mathbf{r}'\| < R$, while the second part $U_{out}(\mathbf{r}) = \sum_{l=0}^{\infty}\sum_{m=-l}^{l}\beta_{lm}r^{l}Y_{lm}(\theta,\phi)$ corresponds to that of stemming from the outer sources with $\|\mathbf{r}'\| > R$, where R is the radius of the sensor array surface. This is verified as follows: We select a point $r_\infty \to \infty$ outside V; then it is easy to see that U_{out} blows up and hence the solution can only be expressed by U_{in}. As a result, all the sources outside V have to be zero for the validation of the Laplace's equation by the uniqueness theorem and hence U_{in} is produced only by the sources inside V. Similarly, when we select a point $r_0 \to 0$ inside V, this time U_{in} blows up and according to the uniqueness theorem, the solution inside is only represented by U_{out}. Since the same solution requires the nullity of the sources inside, only the outer sources contribute to U_{out}.

Accordingly, any magnetic field $\mathbf{B}$ measured at $\mathbf{r}$ can be represented and divided into two components $\mathbf{B}_{in}$ and $\mathbf{B}_{out}$ by vector spherical harmonic functions $\mathbf{x}_{lm}$ and $\mathbf{y}_{lm}$ that are obtained by taking the gradient of (3.5):

$$\begin{aligned}
\mathbf{B}(\mathbf{r}) = \nabla U(\mathbf{r}) &= \sum_{l=0}^{\infty}\sum_{m=-l}^{l}\alpha_{lm}\nabla\left(\frac{Y_{lm}(\theta,\phi)}{r^{l+1}}\right) + \sum_{l=0}^{\infty}\sum_{m=-l}^{l}\beta_{lm}\nabla\left(r^{l}Y_{lm}(\theta,\phi)\right) \\
&= \sum_{l=0}^{\infty}\sum_{m=-l}^{l}\alpha_{lm}\mathbf{x}_{lm} + \sum_{l=0}^{\infty}\sum_{m=-l}^{l}\beta_{lm}\mathbf{y}_{lm} \\
&= \nabla U_{in} + \nabla U_{out} := \mathbf{B}_{in} + \mathbf{B}_{out}
\end{aligned} \tag{3.8}$$

where the inner component $\mathbf{B}_{in}$ corresponds to the source locations $\|\mathbf{r}'\| < R$ and the outer component $\mathbf{B}_{out}$ corresponds to $\|\mathbf{r}'\| > R$ (see Figure 1). These functions also called as SSS basis functions have the explicit form as:

$$\begin{aligned}
\mathbf{x}_{lm} &= \nabla\left(\frac{Y_{lm}(\theta,\phi)}{r^{l+1}}\right) = \frac{1}{r^{l+2}}\left[-(l+1)Y_{lm}(\theta,\phi)\mathbf{u}_r + \frac{Y_{lm}(\theta,\phi)}{\partial\theta}\mathbf{u}_\theta + \frac{imY_{lm}(\theta,\phi)}{\sin\theta}\mathbf{u}_\phi\right] \\
\mathbf{y}_{lm} &= \nabla\left(r^{l}Y_{lm}(\theta,\phi)\right) = r^{l-1}\left[lY_{lm}(\theta,\phi)\mathbf{u}_r + \frac{Y_{lm}(\theta,\phi)}{\partial\theta}\mathbf{u}_\theta + \frac{imY_{lm}(\theta,\phi)}{\sin\theta}\mathbf{u}_\phi\right]
\end{aligned} \tag{3.9}$$

Spherical harmonic functions $Y_{lm}(\theta,\phi)$ are orthonormal eigenfunctions of the Laplacian operator on the spherical surface [12], [61]:

$$\int_{\phi=0}^{2\pi}\int_{\theta=0}^{\pi} Y_{l1m1}(\theta,\phi)Y^{*}_{l2m2}(\theta,\phi)\sin\theta d\theta d\phi = \delta_{l1l2}\delta_{m1m2} \tag{3.10}$$

$$\nabla^2 Y_{lm}(\theta,\phi) = -\frac{l(l+1)}{r^2}Y_{lm}(\theta,\phi). \tag{3.11}$$

They constitute a complete set and hence any harmonic function can be represented as a series expansion of them, i.e., they form Fourier-like representations for any function being evaluated on the spherical surface $k(\theta,\phi)$, which has sufficient continuity properties [61]:

$$k(\theta,\phi) = \sum_{l=0}^{\infty}\sum_{m=-l}^{l}\gamma_{lm}Y_{lm}(\theta,\phi). \tag{3.12}$$

Similar desirable properties such as orthonormality and completeness are also valid for vector spherical harmonics as well as the scalar ones [12], [61], [62]. This makes them naturally useful tools for MEG signal processing. For instance, Popov [63] proposed a continuation of MEG data around the surface of the sensor array using a spherical harmonics expansion. In [64], they exploited the orthogonality properties of the vector spherical harmonics in order to compute the total information from MEG signals using Shannon's theory. In [51], the spherical harmonic functions were used to explore the resolution limits of the MEG inverse problems. They were also commonly utilized for the computation and approximation of the MEG forward problem [65], [66]. We apply (3.8) given for a 3 dimensional magnetic field to an M channel MEG signal as

$$\mathbf{b} = [b_1, b_2, \ldots, b_M]^{\mathrm{T}} = \sum_{l=0}^{L_{in}}\sum_{m=-l}^{l}\alpha_{lm}\mathbf{X}_{lm} + \sum_{l=0}^{L_{out}}\sum_{m=-l}^{l}\beta_{lm}\mathbf{Y}_{lm} = \mathbf{b}_{in} + \mathbf{b}_{out} \tag{3.13}$$

where the SSS basis vectors $\mathbf{X}_{lm}$ and $\mathbf{Y}_{lm}$ are obtained by taking into account the locations and orientations of the sensors. An arbitrary number of coefficients can be included in the expansion up to an upper limit $l = L_{in}$ and $l = L_{out}$ for the sufficient representations of $\mathbf{b}_{in}$ and $\mathbf{b}_{out}$, respectively. Then, the equation (3.13) may be rewritten for the sake of algebraic clarity as

$$\mathbf{b} = \mathbf{S}\boldsymbol{\omega} \tag{3.14}$$

where the $(M \times p)$ dimensional basis functions matrix $\mathbf{S} = [\mathbf{S}_{in}\mathbf{S}_{out}]$ comprises inner and outer basis functions

$$\begin{aligned}\mathbf{S}_{in} &= [\mathbf{X}_{1,-1}, \mathbf{X}_{1,0}, \mathbf{X}_{1,1}, \mathbf{X}_{2,-2}, \ldots, \mathbf{X}_{L_{in},L_{in}}] \\ \mathbf{S}_{out} &= [\mathbf{Y}_{1,-1}, \mathbf{Y}_{1,0}, \mathbf{Y}_{1,1}, \mathbf{Y}_{2,-2}, \ldots, \mathbf{Y}_{L_{out},L_{out}}]\end{aligned} \tag{3.15}$$

and the $(p \times 1)$ coefficient vector $\boldsymbol{\omega} = [\boldsymbol{\alpha}^{\mathrm{T}}\boldsymbol{\beta}^{\mathrm{T}}]^{\mathrm{T}}$ contains the SSS coefficients for inner and outer parts:

$$\begin{aligned}\boldsymbol{\alpha} &= [\alpha_{1,-1}, \alpha_{1,0}, \alpha_{1,1}, \ldots, \alpha_{L_{in},L_{in}}]^{\mathrm{T}} \\ \boldsymbol{\beta} &= [\beta_{1,-1}, \beta_{1,0}, \beta_{1,1}, \ldots, \beta_{L_{out},L_{out}}]^{\mathrm{T}}.\end{aligned} \tag{3.16}$$

Here the total number of the coefficients is denoted by $p = p_{in} + p_{out}$, where the number of the inner coefficients is $p_{in} = L_{in}^2 + 2L_{in}$ and the number of the outer coefficients is $p_{out} = L_{out}^2 + 2L_{out}$. It should be noted that the coefficient with $l = 0, m = 0$ is dismissed in the expansion since that represents a magnetic monopole [66]. The SSS coefficients vectors $\boldsymbol{\alpha}$ for the inner part and $\boldsymbol{\beta}$ for the outer part may be estimated through a pseudo-inverse operation as $\hat{\boldsymbol{\omega}} = \mathbf{S}^{+}\mathbf{b} = [\hat{\boldsymbol{\alpha}}^{\mathrm{T}}\hat{\boldsymbol{\beta}}^{\mathrm{T}}]^{\mathrm{T}}$[10]. Then, the reconstruction of the signal that corresponds to inner sources, that is free of the external interferences, is obtained easily by $\hat{\mathbf{b}}_{in} = \mathbf{S}_{in}\hat{\boldsymbol{\alpha}}$. In practice, p_{in} should be chosen to be less than M in order to have well-posed system of equations, since the number of measurement sensors is limited with respect to the number of degrees of freedom in the field.

The SSS method relies solely on the sensor geometry and the quasistatic Maxwell equations. This distinguishes it from the other commonly used MEG signal separation techniques such as ICA and SSP that depend on spatiotemporal assumptions such as independence or uncorrelatedness. These assumptions may be unrealistic and cause severe signal loss and improper separation. Thus, the SSS offers a much more realistic way to decompose the MEG signal by the token of exploiting the physical knowledge of the system that maps the unknown sources to the observed data.

While the SSS enables the separation of the MEG data into components corresponding to inner and outer sources, it cannot separate the data inside the head to that coming from an arbitrary spherical region of the head. This is due to the fact that, in the first place,

the measurement sensors are located outside the head. More importantly, in the second place, the SSS decomposition can only be achieved for a boundary that does not contain current sources. Only by satisfying this source-free assumption for the MEG sensor array, the Laplace's equation for the magnetic scalar potential in (3.2) can be solved and the magnetic measurements can be written in the form of equation (3.8). In the following sections, we present the development of spatial filters in order to extend the separation capability of the SSS to the regions inside the head.

One should also note that the so-called "magnetic multipole expansion in spherical coordinates" in MEG literature [67],[66] is a specific version of the SSS expansion. It includes only the first part in (3.8) (inner expansion) to represent the MEG measurements. Hence it is identical with the SSS when one takes $L_{out} = 0$. We shortly call it "multipole expansion" throughout this thesis.

3.3 BEAMSPACE METHODOLOGY

Various beamspace design algorithms in the name of "beamforming" were overviewed in detail in [38]. The name "beamforming" comes from the desire to form pencil beams in antenna systems to capture signals arising from specific locations while attenuating the signals coming from the other locations [38].

In particular for MEG signal processing, the beamspace methodology has typically been used as a preprocessing for the purpose of spatial filtering, dimension reduction and noise elimination of data [50],[55]. Then the beamspaced data is typically taken as an input to an inverse method in order to estimate the source magnitudes, orientations and locations. In [38], the beamforming algorithms were classified as data-independent, statistically optimum, adaptive and partially adaptive. In MEG literature, generally the beamspace method is conceived as "data-independent" beamforming, i.e., the weights of the filter are designed

such that its response is dependent neither on data nor on its statistics and hence we accept the same terminology in this thesis. Note that data-independency in the preprocessing may prevent any extra degree of variability stemming from the data when it is given input to the inverse techniques [55].

We can express the energy of the MEG data $\mathbf{b}$ by

$$P(\mathbf{b}) = tr(\mathbf{R}_b) = tr\left(E\{\mathbf{b}\mathbf{b}^{\mathrm{H}}\}\right) \tag{3.17}$$

where the superscript H denotes the Hermitian transpose. By substituting (2.2) into (3.17), the autocorrelation function becomes

$$\mathbf{R}_b = E\{\mathbf{b}\mathbf{b}^{\mathrm{H}}\} = \iint_{\Omega} \mathbf{H}(\mathbf{r}')E\{\mathbf{j}(\mathbf{r}')\mathbf{j}(\mathbf{r}'')^{\mathrm{H}}\}\mathbf{H}(\mathbf{r}'')^{\mathrm{H}}d\Omega' d\Omega'' \tag{3.18}$$

The rationale of the beamspace method relies on looking for a linear transformation matrix $\mathbf{T}$ that maximizes the energy of the data in a region of interest Ω_{ROI}, which is the trace of the autocorrelation matrix

$$\mathbf{R}_{\mathbf{b}ROI} = \iint_{\Omega_{ROI}} \mathbf{H}(\mathbf{r}')E\{\mathbf{j}(\mathbf{r}')\mathbf{j}(\mathbf{r}'')^{\mathrm{H}}\}\mathbf{H}(\mathbf{r}'')^{\mathrm{H}}d\Omega' d\Omega'' \tag{3.19}$$

in Ω_{ROI}. In general, we do not have any knowledge on the sources, then the term in the expectation operator can be taken as identity matrix, i.e.,$E\{\mathbf{j}(\mathbf{r}')\mathbf{j}(\mathbf{r}'')^{\mathrm{H}}\} = \mathbf{I}$. In this case, the cost function is the trace of a matrix

$$\mathbf{G} = \int_{\Omega_{ROI}} \mathbf{H}(\mathbf{r}')\mathbf{H}(\mathbf{r}')^{\mathrm{H}}d\Omega' \tag{3.20}$$

so-called as the Gram matrix [50], which describes the deterministic second-order relations among the leadfields. Hence, maximizing the energy of the beamspaced data $\tilde{\mathbf{b}} = \mathbf{T}^{\mathrm{T}}\mathbf{b}$ is equivalent to

$$\max P(\tilde{\mathbf{b}}) = \max tr(\mathbf{T}^{\mathrm{T}}\mathbf{R}_{\mathbf{b}ROI}\mathbf{T}) = \max tr(\mathbf{T}^{\mathrm{T}}\mathbf{G}\mathbf{T}) \quad \text{if } E\{\mathbf{j}(\mathbf{r}')\mathbf{j}(\mathbf{r}'')^{\mathrm{H}}\} = \mathbf{I}. \tag{3.21}$$

By imposing a constraint $\mathbf{T}^{\mathrm{T}}\mathbf{T} = \mathbf{I}$, the beamspace optimization can be written as:

$$\max_{\mathbf{T}} \; tr(\mathbf{T}^{\mathrm{T}}\mathbf{G}\mathbf{T}) \quad \text{subject to} \quad \mathbf{T}^{\mathrm{T}}\mathbf{T} = \mathbf{I} \tag{3.22}$$

Solution of (3.22) can be found out simply by the method of Lagrange multipliers, which results a $(M \times n)$ dimensional matrix $\mathbf{T}$, whose columns are composed by the eigenvectors of the Gram matrix $\mathbf{G}$, corresponding to the greatest n eigenvalues ($n \leq M$). In [55], the detail of this criterion that allows for an optimal linear transformation of the magnetic field data in mean-square sense is provided. The solution $\mathbf{T}$ can be shown to correspond to a linear transformation which minimizes the mean-squared representation error (MSRE)[55]:

$$\text{MSRE} = |\mathbf{b}^{\mathrm{T}}\mathbf{b} - \tilde{\mathbf{b}}^{\mathrm{T}}\tilde{\mathbf{b}}| = \int_{\Omega} \|(\mathbf{I} - \mathbf{T}^{\mathrm{T}}\mathbf{T}\mathbf{H}(\mathbf{r}')\mathbf{j}(\mathbf{r}'))\|^2 d\Omega \tag{3.23}$$

Therefore the beamspace method yields the optimal representation of the data in the sense of mean-squares for any determined source space Ω_{ROI}.

When the beamspace methodology is applied "directly" to EEG/MEG data, the integration in (3.20) is approximated by dividing the source volume into grids and computing it discretely at all those grids. The choice of the number of integration elements (number of voxels) determines the accuracy of the Gram matrix computation.

3.4 SPATIAL FILTERING IN SPHERICAL HARMONICS

In this section, novel algorithms for spatial filtering are demonstrated. These algorithms were developed assuming that the SSS was applied to the data beforehand. In other words, after the inner SSS coefficients ($\boldsymbol{\alpha}$) are extracted from the MEG data, our goal is to optimally manipulate them such that the reconstruction of the manipulated coefficients gives rise to the desired components. The SSS expansion origin should be selected as symmetrically as possible with respect to the sensors for an accurate representation of the separated components [68]. Accordingly, the SSS expansion origin is determined by fitting a hypothetical spherical shell to the sensor array.

In Section 3.4.1, we derive a beamspace formulation in the spherical harmonics domain in order to separate the MEG data into deep and superficial components.

In Section 3.4.2, we present our main algorithm to decompose the MEG data into parts corresponding to concentric spherical source regions, in particular to those that are originated

from deep and superficial sources. We call this method the expanded SSS method (exSSS). The components for this method are named as deep and superficial. Here, the depth is meant to be defined according to the SSS expansion origin.

In Section 3.4.3, we discuss and show a generalized method for exSSS in order to spatially filter the signal to any spherical region with a user-specified arbitrary origin in the head space, i.e., without necessarily being dependent on the SSS expansion origin. We call this method generalized expanded SSS (genexSSS). This extends the capability and the flexibility of the exSSS to spherical source volumes that are not dependent on any fixed origin. The schematic representation given in Figure 2 illustrates the main parts in the algorithms.

3.4.1 Beamspace in the SSS domain for deep and superficial sources

In this section, we concentrate on extending the SSS by by manipulating $\boldsymbol{\alpha}$ to further separate the signal inside the head into two parts that correspond to $||\mathbf{r}'|| < \hat{r}$ and $||\mathbf{r}'|| > \hat{r}$, where $\hat{r}$ is any arbitrary radius which is less than R and greater than zero. Hence the SSS-filtered signal $\mathbf{b_{in}}$ will be decomposed into two parts: signals originating from deep sources ($\mathbf{b_{deep}}$) and superficial sources ($\mathbf{b_{sup}}$). Figure 1 exhibits the geometrical schema of this separation.

Our method aims to find a transformation in the SSS domain that maximizes the energy for the deep (or superficial) component while minimizing it for the superficial (or deep) component. This may be formulated as

$$\max_{\mathbf{T}} \frac{tr(\mathbf{T}^{\mathrm{T}}\mathbf{G}_d\mathbf{T})/v_d}{tr(\mathbf{T}^{\mathrm{T}}\mathbf{G}_s\mathbf{T})/v_s} \tag{3.24}$$

where $\mathbf{G}_d$ and $\mathbf{G}_s$ are Gram matrices, and v_d and v_s are spherical volumes for deep and superficial components, respectively.

This criterion is one of the beamspace formulations known as MaxSNR in the literature [38], [50]: Hence we consider the deep part as "signal" and the remaining superficial part as "noise" and would like to maximize the SNR by a linear transformation. The solution for Equation (3.24) can be handled by assigning a change of variable as $\mathbf{T}' = \mathbf{G}_s^{-1/2}\mathbf{T}$. Then the maximization term can be written as:

$$\max \frac{tr(\mathbf{T'}^{\mathrm{T}}\mathbf{G}_d\mathbf{T}')/v_d}{tr(\mathbf{T'}^{\mathrm{T}}\mathbf{G}_s\mathbf{T}')/v_s} = \max \frac{tr(\mathbf{T}^{\mathrm{T}}(\mathbf{G_s}^{-1/2})^{\mathrm{T}}\mathbf{G}_d\mathbf{G_s}^{-1/2}\mathbf{T})/v_d}{tr(\mathbf{T}^{\mathrm{T}}(\mathbf{G_s}^{-1/2})\mathbf{G}_s\mathbf{G_s}^{-1/2}\mathbf{T})/v_s} \tag{3.25}$$

Since the Gram matrix is always Toeplitz, (3.25) becomes

$$\max \frac{tr(\mathbf{T}^{\mathrm{T}}{\mathbf{G_s}}^{-1/2}\mathbf{G}_d{\mathbf{G_s}}^{-1/2}\mathbf{T})/v_d}{tr(\mathbf{T}^{\mathrm{T}}{\mathbf{G_s}}^{-1/2}\mathbf{G}_s{\mathbf{G_s}}^{-1/2}\mathbf{T})/v_s} = \max \frac{tr(\mathbf{T}^{\mathrm{T}}{\mathbf{G_s}}^{-1/2}\mathbf{G}_d{\mathbf{G_s}}^{-1/2}\mathbf{T})/v_d}{tr(\mathbf{T}^{\mathrm{T}}\mathbf{T})/v_s}\,. \tag{3.26}$$

This formulation indicates that (3.24) is equivalent to

$$\max \frac{v_s}{v_d} tr(\mathbf{T}^{\mathrm{T}}{\mathbf{G_s}}^{-1/2}\mathbf{G}_d{\mathbf{G_s}}^{-1/2}\mathbf{T}). \tag{3.27}$$

By imposing a constraint $\mathbf{T}^{\mathrm{T}}\mathbf{T} = \mathbf{I}$ on the transformation matrix, we can finally express the beamspace optimization as

$$\max_{\mathbf{T}} \frac{v_s}{v_d} tr(\mathbf{T}^{\mathrm{T}}{\mathbf{G_s}}^{-1/2}\mathbf{G}_d{\mathbf{G_s}}^{-1/2}\mathbf{T}) \quad \text{subject to} \quad \mathbf{T}^{\mathrm{T}}\mathbf{T} = \mathbf{I}\,. \tag{3.28}$$

Thus the optimization reduces to a simple beamspace formulation as in (3.22) and the solution becomes a matrix whose columns are the eigenvectors of

$$\mathbf{G}_f = \frac{v_s}{v_d}{\mathbf{G_s}}^{-1/2}\mathbf{G}_d{\mathbf{G_s}}^{-1/2} \tag{3.29}$$

that correspond to its largest eigenvalues [50].

We consider the leadfield-like representations of the inner SSS coefficients given by [67],[10]

$$\alpha_{lm} = \int_{\Omega_{in}} \boldsymbol{\lambda}_{lm}(\mathbf{r}') \cdot \mathbf{j}_{in}(\mathbf{r}') d\Omega_{in} \tag{3.30}$$

where α_{lm}'s are the SSS inner component coefficients, Ω_{in} denotes the inner head space, $\mathbf{j}_{in}(\mathbf{r}')$ is the inner source density at any source location $\mathbf{r}'$ and $\boldsymbol{\lambda}_{lm}$ is the leadfield-like vector directly related to the vector spherical harmonic functions $\mathbf{x}_{lm}(\theta,\phi)$ defined as

$$\boldsymbol{\lambda}_{lm}(\mathbf{r}') = \frac{i}{2l+1}\sqrt{\frac{l}{l+1}} r^l \mathbf{x}^*_{lm}(\theta,\phi) \tag{3.31}$$

$$\mathbf{x}_{lm}(\theta,\phi) = \frac{-1}{\sqrt{l(l+1)}}\left[\frac{mY_{lm}(\theta,\phi)}{\sin\theta}\mathbf{u}_\theta + i\frac{\partial Y_{lm}(\theta,\phi)}{\partial\theta}\mathbf{u}_\phi\right]. \tag{3.32}$$

$\mathbf{x}_{lm}(\theta,\phi)$ is one of the three vector spherical harmonic functions whose concepts and basic properties were introduced by Hill in [62]. Note that MEG senses only the tangential components of the source currents in a spherically symmetric conductor and hence $\mathbf{x}_{lm}(\theta,\phi)$ does not have a radial component. Additionally, the vector spherical harmonics yield an or-

thogonal representation for the primary current in the case of spherically symmetric volume conductor unlike the non-orthogonal representation by leadfield vectors of forward modeling computations.

Let us denote the (l, m) index of the SSS coefficient (where l and m are integers and $1 \leq l \leq L_{in}, -l \leq m \leq l$) as $a = 1, \ldots, p_{in}$ and the (L, M) index of the SSS coefficient (where L and M are integers and $1 \leq L \leq L_{in}, -L \leq M \leq L$) as $b = 1, \ldots, p_{in}$ for simplicity. In this case, the Gram matrix $\mathbf{G}^s$ for the spherical harmonics domain can be defined as

$$\begin{aligned} (\mathbf{G}^s)_{ab} &= \int_\Omega \boldsymbol{\lambda}_{lm}(\mathbf{r}') \cdot \boldsymbol{\lambda}_{LM}(\mathbf{r}') d\Omega = \int_\Omega \boldsymbol{\lambda}_a(\mathbf{r}') \cdot \boldsymbol{\lambda}_b(\mathbf{r}') d\Omega \\ \mathbf{G}^s &= \int_\Omega \boldsymbol{\Lambda}(\mathbf{r}') \boldsymbol{\Lambda}(\mathbf{r}')^{\mathrm{H}} d\Omega \end{aligned} \tag{3.33}$$

where $\boldsymbol{\Lambda}(\mathbf{r}') = [\boldsymbol{\lambda}_{1,-1}(\mathbf{r}'), \boldsymbol{\lambda}_{1,0}(\mathbf{r}'), \ldots, \boldsymbol{\lambda}_{L_{in},L_{in}}(\mathbf{r}')]^{\mathrm{T}}$ is the $(p_{in} \times 2)$ dimensional matrix of spherical leadfield-like vectors that are built by spherical harmonics functions. Notice that unlike the classical Gram matrix defined in (3.20), the sensor configuration (orientations, gradiometer and magnetometer specifications, etc.) is not explicitly present in (3.33). However, this does not lose generality since the $\boldsymbol{\alpha}$ coefficients already contain this information after the SSS is applied. Accordingly, the a^{th} row and b^{th} column of Gram matrix $\mathbf{G}_d$ for the deep component can be computed as

$$(\mathbf{G}_d)_{ab} = \int_\phi \int_\theta \int_{r=0}^{\hat{r}} \left(\frac{i}{2l+1} \sqrt{\frac{l}{l+1}} r^l \mathbf{x}^*_{lm}(\theta, \phi) \right) \cdot \left(\frac{-i}{2L+1} \sqrt{\frac{L}{L+1}} r^L \mathbf{x}_{LM}(\theta, \phi) \right) r^2 \sin\theta dr d\theta d\phi. \tag{3.34}$$

Utilizing the orthonormality property of vector spherical harmonics [62], [61]

$$\int_\phi \int_\theta \mathbf{x}^*_{lm}(\theta, \phi) \cdot \mathbf{x}_{LM}(\theta, \phi) \sin\theta d\theta d\phi = \delta_{lL} \delta_{mM} \tag{3.35}$$

equation (3.34) can be reduced to the diagonal matrix

$$\begin{aligned} (\mathbf{G}_d)_{ab} &= \delta_{lL}\delta_{mM} \frac{1}{(2l+1)^2} \frac{l}{l+1} \int_\phi \int_\theta |\mathbf{x}_{lm}(\theta, \phi)|^2 \sin\theta d\theta d\phi \int_{r=0}^{\hat{r}} r^{2l+2} dr \\ &= \delta_{lL}\delta_{mM} \frac{1}{(2l+1)^2} \frac{l}{l+1} \frac{\hat{r}^{2l+3}}{2l+3} = \delta_{ab} y(l) \end{aligned} \tag{3.36}$$

with $\delta_{ab} = \delta_{lL}\delta_{mM}$ and $y(l) = \frac{1}{(2l+1)^2} \frac{l}{l+1} \frac{\hat{r}^{2l+3}}{2l+3}$.

Equation (3.36) implies that the diagonal matrix $\mathbf{G}_d$ can be explicitly interpreted as below:

$$\mathbf{G}_d = \begin{bmatrix} y(1) & & & & & & & \\ & y(1) & & & & & & \\ & & y(1) & & & & & \\ & & & y(1) & & & & \\ & & & & y(2) & & & \\ & & & & & y(2) & & \\ & & & & & & \ddots & \\ & & & & & & & y(L_{in}) \end{bmatrix} \tag{3.37}$$

We can find the Gram matrix for the superficial component $\mathbf{G}_s$ by only changing the lower limit to $\hat{r}$ and the upper limit to R for the radial parts:

$$(\mathbf{G}_s)_{ab} = \int_\phi \int_\theta \int_{\hat{r}}^{R} \left(\frac{i}{2l+1} \sqrt{\frac{l}{l+1}} r^l \mathbf{x}^*_{lm}(\theta, \phi) \right) \cdot \left(\frac{-i}{2L+1} \sqrt{\frac{L}{L+1}} r^L \mathbf{x}_{LM}(\theta, \phi) \right) r^2 \sin\theta dr d\theta d\phi. \tag{3.38}$$

Conducting similar computations to the ones in (3.36), the Gram matrix for the superficial component is found:

$$(\mathbf{G}_s)_{ab} = \frac{1}{(2l+1)^2} \frac{l}{l+1} \frac{R^{2l+3} - \hat{r}^{2l+3}}{2l+3} \delta_{ab}. \tag{3.39}$$

Then by substituting (3.36) and (3.39) to (3.29), the final Gram matrix can be obtained:

$$(\mathbf{G}_f)_{ab} = \frac{v_s}{v_d} \frac{\hat{r}^{2l+3}}{R^{2l+3} - \hat{r}^{2l+3}} \delta_{ab}. \tag{3.40}$$

Since $\mathbf{G}_f$ is a diagonal matrix, all of its eigenvectors constitute an identity matrix and its eigenvalues are in the form of (3.40). This result suggests a transformation matrix $\mathbf{T}$ that selects the $\boldsymbol{\alpha}$ coefficients where $\frac{v_s}{v_d} \frac{\hat{r}^{2l+3}}{R^{2l+3} - \hat{r}^{2l+3}}$ is sufficiently large, while the other coefficients are eliminated. This corresponds to the first $\boldsymbol{\alpha}$ coefficients $\boldsymbol{\alpha}_{deep} = [\alpha_{1,-1}, \alpha_{1,0}, \ldots, \alpha_{ss}]^{\mathrm{T}}$ whose indices include only the degrees $l = 1, 2, \ldots, s$. Reconstructing the signal with the selected SSS coefficients leads to an estimate of deep sources in the optimal sense with

respect to the beamspace technique. As pointed out in [55] in detail, the MSRE given in (3.23) is the sum of the eigenvalues that correspond to the eliminated coefficients, hence the coefficients that are close to zero have negligible effect on the accuracy of the beamspace representation. The metric for the accuracy of the beamspace representation can be obtained through dividing the sum of the selected eigenvalues by the sum of the all eigenvalues. This metric is a reasonable measure when one determines a threshold to select the $\boldsymbol{\alpha}$ coefficients.

Likewise, in order to estimate the superficial component, one has to optimize the reciprocal of the term in (3.24) in the same way, which results in obtaining the reciprocal of (3.40) for the final Gram matrix $\mathbf{G}_f$. Therefore, on the exact contrary to the case of deep components, the beamspace transformation for superficial components simply yields the last $\boldsymbol{\alpha}$ coefficients $\boldsymbol{\alpha}_{sup} = [\alpha_{L_{in}-s+1,-(L_{in}-s+1)}, \alpha_{L_{in}-s+1,-(L_{in}-s)}, \ldots, \alpha_{L_{in},L_{in}}]^{\mathrm{T}}$ whose indices are $l = L_{in} - s + 1, \ldots, L_{in}$. Hence eliminating the initial and the final $\boldsymbol{\alpha}$ coefficients results in optimal solutions in the mean-square sense in the SSS domain for the specified deep and superficial source regions, respectively. As (3.40) indicates, the number of coefficients to be selected directly depends on the determination of the boundary parameters, i.e., the separating radius $\hat{r}$ and the sensor array radius R.

3.4.2 Expanded SSS (exSSS)

As stated in Section 3.1.2, the estimation of deep and superficial components from the input data using beamspace criterion can be considered analogous to spatial filtering in the SSS domain. In this case, l denotes the spatial frequency with the lower frequencies corresponding to deeper sources, whereas higher frequencies correspond to the more superficial ones. This result agrees with the equations (3.30) and (3.31), which show that the greater the l degree of the SSS coefficients are, the greater the contribution from the superficial sources is. Our result is also consistent with the study in [69], which states that the highest spatial frequencies are most related to the sources closest to the measurement plane, i.e., superficial sources. The contribution from the sources increases exponentially with l. As shown in the previous section, the beamspace solution corresponds to selecting the SSS coefficients from the beginning and the end (Fig. 3a). This may be interpreted as a "sharp" low-pass filter-

ing for the estimation of deep sources and a "sharp" high-pass filtering for the superficial sources. However, the extent of the contribution from the sources changes depending on the l-degree and the depth $\hat{r}$ and hence selecting the coefficients uniformly as formulated in Section 3.4.1, may not give a reliable estimation. To overcome this problem, we suggest an eigenvalue-weighted filtering of the selected SSS coefficients (Figure 3b). Eigenvalues of the Gram matrix $\mathbf{G}_f$ represent the contributed energy to the magnetic measurement for a particular l-degree. Hence, we modify the beamspace transformation matrix $\mathbf{T}$ as $\tilde{\mathbf{T}} = \mathbf{TD}$, where $\mathbf{D}$ denotes the diagonal matrix whose diagonal elements are the selected largest eigenvalues of $\mathbf{G}_f$. This modification leads to a simple manipulation of the SSS coefficients as

$$(\hat{\alpha}_{lm})_{deep} = \alpha_{lm}\frac{v_s}{v_d}\frac{\hat{r}^{2l+3}}{R^{2l+3}-\hat{r}^{2l+3}} = \alpha_{lm}\frac{(R^3-\hat{r}^3)\,\hat{r}^{2l}}{R^{2l+3}-\hat{r}^{2l+3}} = \alpha_{lm}f(\hat{r},R) \tag{3.41}$$

where $f(\hat{r},R) = \frac{(R^3-\hat{r}^3)\hat{r}^{2l}}{R^{2l+3}-\hat{r}^{2l+3}}$. In practice, the selection of the eigenvectors corresponding to the largest eigenvalues (mentioned in the previous section) is unnecessary for the modified beamspace method, since the contribution of the eigenvectors to the Gram matrix are determined by the eigenvalue-weighting, i.e., the ones corresponding to small eigenvalues diminish with the weighting.

The filter's output should ideally be zero for all frequencies when $\hat{r} = 0$ (non-signal), i.e., $f(0,R) = 0$ and its output should be unity for all frequencies when $\hat{r} = R$ (all-signal) , i.e., $f(R,R) = 1$. Hence, we look for the limits in order to normalize the filter for non-signal and all-signal cases. As $\hat{r} \to 0$, it is easy to see that $f(0,R) \to 0$. For the all-signal case, the limit is taken using L'Hopitals rule:

$$\lim_{\hat{r}\to R} f(\hat{r},R) = \lim_{\hat{r}\to R}\frac{(R^3-\hat{r}^3)\,\hat{r}^{2l}}{R^{2l+3}-\hat{r}^{2l+3}} = \lim_{\hat{r}\to R}\frac{2l\hat{r}^{2l-1}R^3-(2l+3)\hat{r}^{2l+2}}{-(2l+3)\hat{r}^{2l+2}} = \frac{3}{2l+3} \tag{3.42}$$

Equation (3.42) indicates that the limit for the all-signal case depends on l value, therefore we need to normalize the filter by multiplying every coefficient with $\frac{2l+3}{3}$. This will guarantee the necessary boundary conditions we stated above. Hence the normalized filter can be expressed as

$$\begin{aligned}(\tilde{\alpha}_{lm})_{deep} &= \alpha_{lm}\frac{2l+3}{3}f(\hat{r},R)\\ \tilde{\boldsymbol{\alpha}}_{deep} &= \mathbf{F}\boldsymbol{\alpha}\end{aligned} \tag{3.43}$$

where $\mathbf{F}$ is the diagonal matrix whose elements are composed of $\frac{2l+3}{3} f(\hat{r}, R)$. Figure 4a depicts how the SSS coefficients are modified by the normalized filter when $\hat{r}$ varies between 0 and R. The estimated deep component is obtained by reconstructing the signal with the filtered coefficients:

$$\hat{\mathbf{b}}_{deep} = \mathbf{S}_{in} \tilde{\boldsymbol{\alpha}}_{deep}. \tag{3.44}$$

Estimation of the superficial part is similarly realized by the modification given below:

$$\begin{aligned} (\tilde{\alpha}_{lm})_{sup} = \alpha_{lm} \frac{3}{2l+3} \frac{1}{f(\hat{r}, R)} &= \alpha_{lm} \frac{3}{2l+3} \frac{1}{R^3 - \hat{r}^3} \frac{R^3 - \hat{r}^3}{\hat{r}^{2l}} \\ \hat{\mathbf{b}}_{sup} &= \mathbf{S}_{in} \tilde{\boldsymbol{\alpha}}_{sup}. \end{aligned} \tag{3.45}$$

While the filter in (3.45) gives unity for all coefficients, when $\hat{r} \to R$ (non-signal case, since there is no signal for $\hat{r} > R$); the filter coefficients tend to infinity for $\hat{r} \to 0$ (all-signal case). Hence, the superficial region spatial filter does not give stable solutions when the separating radius is close to zero (Figure 4b). In these cases, we advise using deep region spatial filter for $\hat{r} \to R$, since it yields more stable and accurate estimates.

The exSSS method permits the assignment of weights to the SSS coefficients based on their contribution to deep or superficial sources instead of a uniform selection process. Accordingly, the modified beamspace solution "rolls-off" the spatial frequencies yielding the alternative filtering depicted in Figures 3b and 4.

3.4.3 Generalized expanded SSS (genexSSS)

The SSS expansion origin must be determined such that any part of the brain is closer to it than any of the MEG sensors for successful elimination of the undesired external noise. It was reported that, in general the best performances of the SSS are obtained when the expansion origin is selected symmetrical to the sensors [68]. However, it is highly possible that the ROI's are not concentric with the SSS expansion origin. In these cases, the exSSS method is not applicable for spatial filtering. In Figure 5, we depict a schematic representation of the hypothetical sphere V_1 that is obtained with a fitting to the sensors. The center of this sphere is O, which is also accepted as the SSS expansion origin. Let's suppose that our aim is to spatially filter the signal to the spherical region V_2 with a center O$'$ and a radius $\hat{r}$ .In

this case, we consider another spherical volume V_3 that is centered at O$'$ and encapsulates the whole brain source space. Then it is clear that the minimum radius of V_3 should be $(R + ||\text{O-O}'||)$ in order to cover V_2, i.e., V_2 and V_3 are tangent to each other. Since we can assume that the external sources are eliminated by the SSS, there are not any sources in the complement of V_1 relative to V_3, which we denote as $V_3 \backslash V_1$ in Figure 5. This gives the legitimacy to implement the beamspace filtering for the targeted region V2, since V2 and V3 are concentric at O$'$.

We give the details of this filtering method as follows: After the SSS is applied to the data $\mathbf{b}$, we obtain the signal $\mathbf{b}_{in}$ that is expected only to arise from the regions in the head space. The genexSSS method [70] consists of realizing a multipole expansion at O$'$. Let's assume that the basis matrix of this expansion is $\tilde{\mathbf{S}}$,which is computed similarly to $\mathbf{S_{in}}$ but only taking the origin as O$'$ instead of O. The expansion and the estimation of the multipole coefficients can be described as:

$$\begin{aligned} \mathbf{b}_{in} &= \tilde{\mathbf{S}}\boldsymbol{\alpha}'' \\ \hat{\boldsymbol{\alpha}}'' &= \tilde{\mathbf{S}}^{+}\mathbf{b}_{in} \end{aligned} \tag{3.46}$$

It should be noted that the multipole coefficients are intrinsic only to the source and the expansion origin [71]. If the external sources are eliminated by the SSS, we can consider a new hypothetical source space V_3 with the center O$'$ and the radius $(R + ||\text{O-O}'||)$ in order to realize a new MaxSNR beamspace as in (3.24), since this sphere becomes concentric with the targeted spherical region as can be observed from Figure 5. In this case the filtering is realized by

$$(\hat{\alpha}_{lm})_f = (\alpha_{lm})'' f(\hat{r}, R + ||O - O'||)\frac{2l+3}{3} \tag{3.47}$$

and hence the filtered signal $\hat{\mathbf{b}}_f$ is finally obtained by transforming the coefficients back to the measurements space:

$$\hat{\mathbf{b}}_f = \tilde{\mathbf{S}}\hat{\boldsymbol{\alpha}}_f \tag{3.48}$$

These steps lead to a spatial filter that can be formulated as:

$$\hat{\mathbf{b}}_f = \tilde{\mathbf{S}}\tilde{\mathbf{F}}\hat{\boldsymbol{\alpha}}'' = \tilde{\mathbf{S}}\tilde{\mathbf{F}}(\tilde{\mathbf{S}})^{+}\mathbf{b}_{in} = \tilde{\mathbf{S}}\tilde{\mathbf{F}}(\tilde{\mathbf{S}})^{+}\mathbf{S}_{in}\boldsymbol{\alpha} \tag{3.49}$$

where $\tilde{\mathbf{F}}$ is a diagonal matrix consisting of $f(\hat{r}, R + |O - O'|)^{\frac{2l+3}{3}}$. As can be seen by a comparison of (3.43) and (3.49), when one shifts the origin of the targeted region from O to O′, in order to estimate $\hat{\mathbf{b}}_f$, the only additional term to compute is $\tilde{\mathbf{S}}$.

The multipole coefficients of the filtered signal $\hat{\mathbf{b}}_f$ helps us to observe how the original inner SSS coefficients $\boldsymbol{\alpha}$ are modified by the proposed spatial filter:

$$\hat{\boldsymbol{\alpha}}_f := (\mathbf{S}_{in})^{+}\hat{\mathbf{b}}_f = (\mathbf{S}_{in})^{+}\tilde{\mathbf{S}}\tilde{\mathbf{F}}(\tilde{\mathbf{S}})^{+}(\mathbf{S}_{in})\boldsymbol{\alpha} := \mathbf{F}''\boldsymbol{\alpha} \tag{3.50}$$

where $\mathbf{F}'' = (\mathbf{S}_{in})^{+}\tilde{\mathbf{S}}\tilde{\mathbf{F}}(\tilde{\mathbf{S}})^{+}(\mathbf{S}_{in})$ explicitly shows the necessary manipulation of $\boldsymbol{\alpha}$ for an estimation of the signal corresponding to the target region. This also yields evidence how this filtering is the generalized form of (3.43), since when one selects O=O′, it is easy to see that

$$\begin{aligned} \tilde{\mathbf{S}} &= \mathbf{S}_{in} \\ (\mathbf{S}_{in})^{+}\tilde{\mathbf{S}} &\approx (\tilde{\mathbf{S}})\mathbf{S}_{in} \approx \mathbf{I} \\ \mathbf{F}'' &\approx \tilde{\mathbf{F}} = \mathbf{F} \end{aligned} \tag{3.51}$$

which makes the filtering in (3.49) equivalent to (3.43), i.e., $\mathbf{F}'' \approx \mathbf{F}$ and $\hat{\boldsymbol{\alpha}}_f \approx \tilde{\boldsymbol{\alpha}}_{deep} = \mathbf{F}\boldsymbol{\alpha}$. For the general case of O≠O′, notice that the filtering matrix $\mathbf{F}''$ is not diagonal. In other words, the SSS coefficients α_{lm} are not modified by weighting them separately as in (3.43), but in general they are transformed also by the linear contributions from the other coefficients.

3.4.4 Adding data dependency

Additionally, for a compensation of errors in the SSS [10] or the filtering at O' in genexSSS, one may attach a simple data dependency to our filters described in Section 3.4.2 and Section 3.4.3, which corresponds to principal component analysis (PCA), as described in [57]. This is realized by constituting the $(M \times D)$ dimensional matrix $\mathbf{D} = [\mathbf{u}_1, \mathbf{u}_2, \ldots, \mathbf{u}_D]$, where $\mathbf{u}_i$ is the eigenvector corresponding to the largest i^{th} eigenvalue $(i = 1, \ldots, D)$ of the autocorrelation matrix $\mathbf{R}_{in}$ of the data with $\mathbf{R}_{in} = E\{\mathbf{b}_{in}\mathbf{b}_{in}^{\mathrm{T}}\}$. The data dependent filtering is hence managed by projecting the filtered data into signal subspace as:

$$\left(\hat{\mathbf{b}}_f\right)_{data\_dependent} = \mathbf{D}\mathbf{D}^{\mathrm{T}}\hat{\mathbf{b}}_f. \tag{3.52}$$

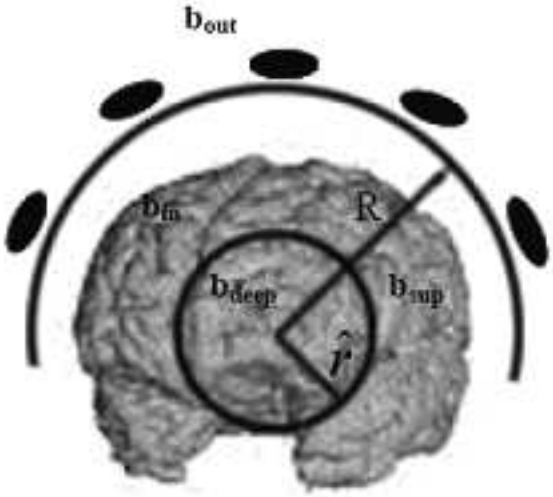

Figure 1: The SSS method decomposes the MEG data $\mathbf{b}$ into components $\mathbf{b}_{in}$ and $\mathbf{b}_{out}$, which correspond to inside the sensor array volume and outside it. The proposed approach decomposes inner SSS component $\mathbf{b}_{in}$ into $\mathbf{b}_{deep}$ and $\mathbf{b}_{sup}$ by determining a spherical boundary inside the head.

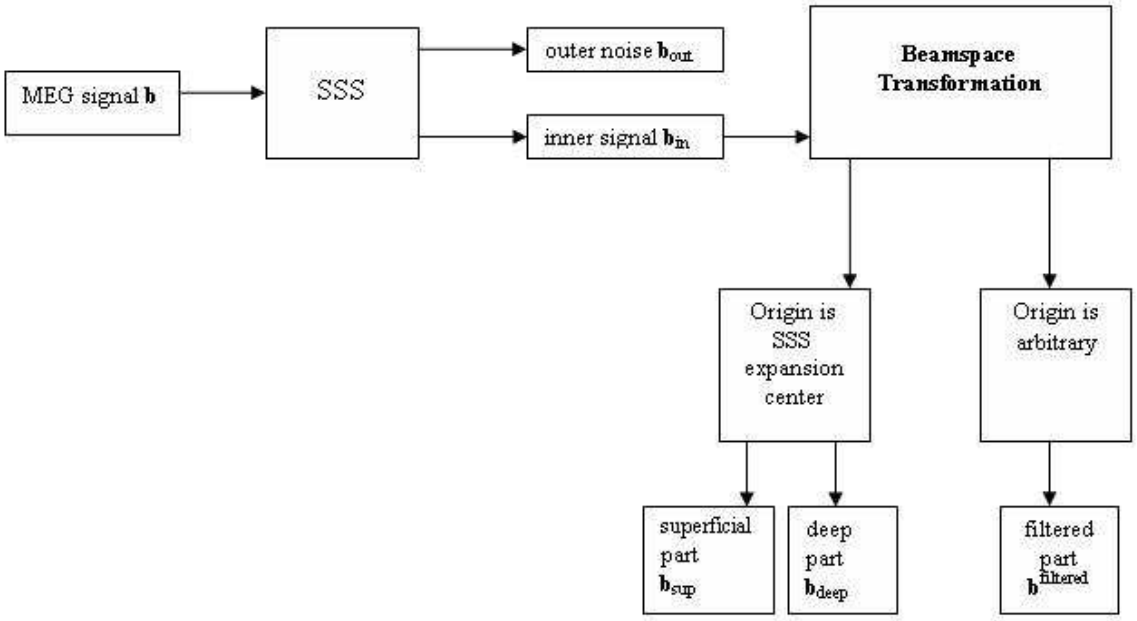

Figure 2: The main steps of the proposed spatial filtering methods

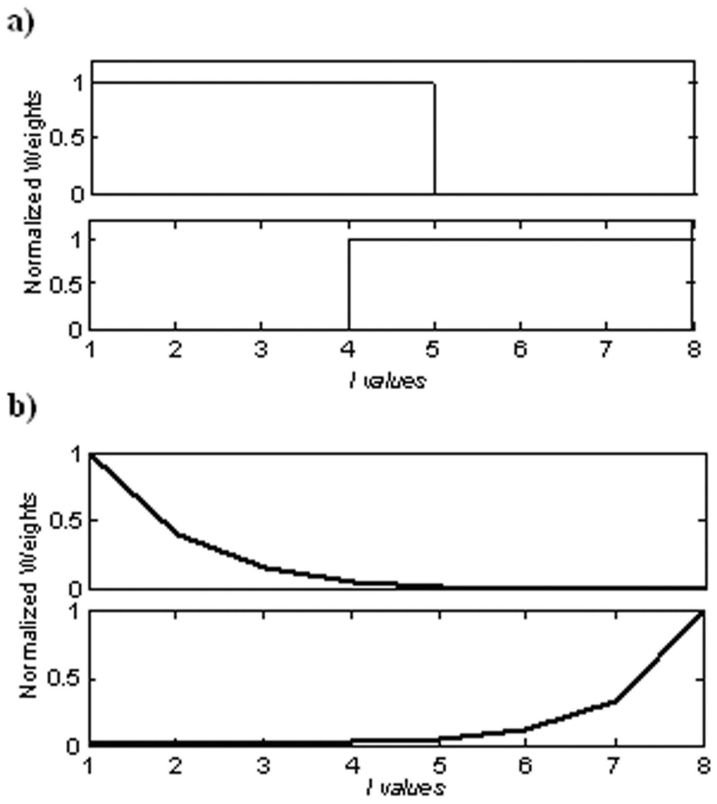

Figure 3: For the separating radius $\hat{r} = 6$ cm and sensor array radius R=11 cm a) "Sharp" spatial filtering of the SSS coefficients according to the classical beamspace criterion for deep (top panel) and superficial (bottom panel) components. b) Spatial filtering of the SSS coefficients according to the modified beamspace criterion (eigenvalue weighting) for deep (top panel) and superficial (bottom panel) components. The filter weights are normalized.

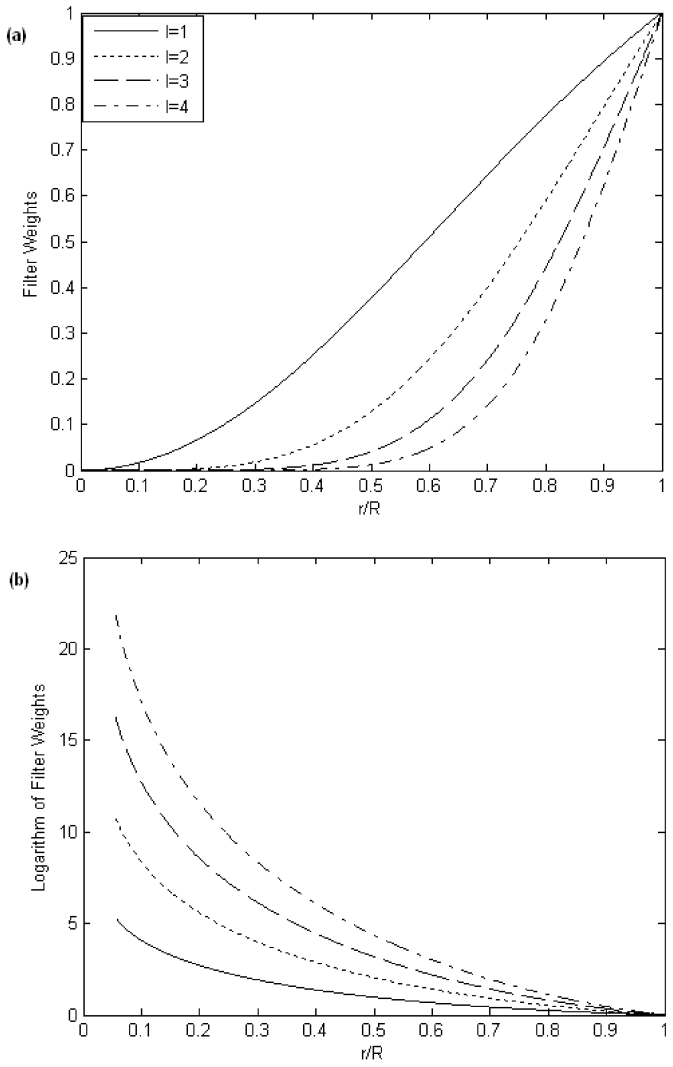

Figure 4: Filter weights for modified beamspace approach as the separating radius $\hat{r}$ varies between 0 and R, a) for the deep component estimation, b) for the superficial component estimation. The weights are depicted for l=1(solid), l=2(dotted), l=3 (dashed) and l=4 (dot-dashed).

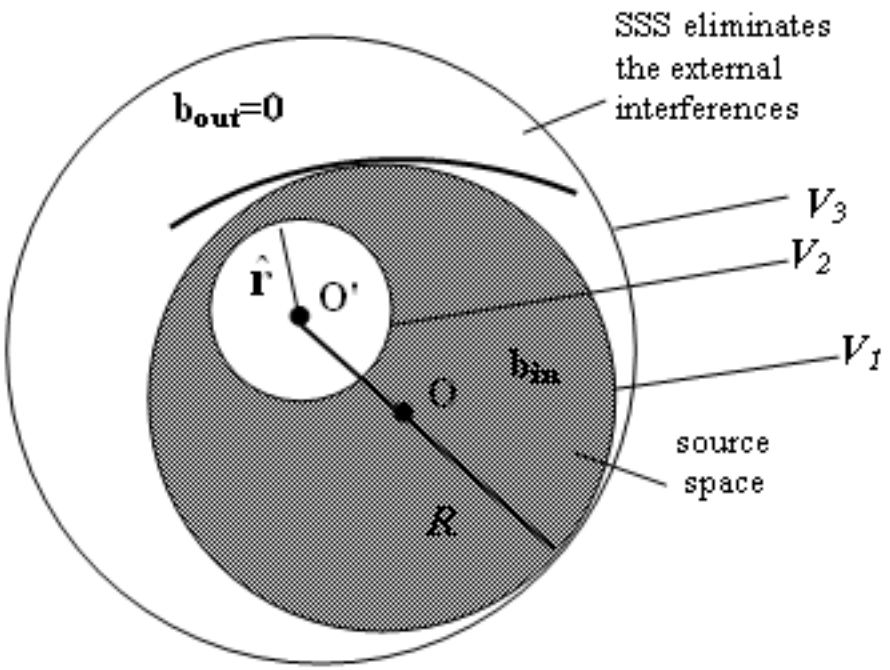

Figure 5: The head space is represented by the hypothetical sphere V_1 with the center O and the radius R, the ROI is represented by the sphere V_2 with the center O′ and the radius $\hat{r}$. The spherical region V_3 is centered on O′ and it covers the whole head space with the radius $(R + |\text{O-O}'|)$. Under the assumption of the non-existence of the external interferences ($\mathbf{b}_{out} = 0$) by the SSS expanded at O, the beamspace filtering is applied to the multipole coefficients expanded at O′ in order to constrain the signal to V_2.

4.0 EXPERIMENTS

4.1 MEG MEASUREMENT SYSTEM

In order to verify the validity of the proposed method and evaluate its performance under various conditions, we used simulated MEG data with sensor characteristics compatible with those of Elekta Neuromag® Vector view 306 channel system. The phantom and real data experiments were also conducted using the same system by the support of the Center for Advanced Brain Magnetic Source Imaging (CABMSI) and University of Pittsburgh Medical Center (UPMC).

This system measures the magnetic signal using totally 306 sensors: 204 planar gradiometers and 102 magnetometers. The sensors are arranged in a plane as 102 tripled sensor elements, each of which includes a magnetometer that measures the z component of the magnetic field B_z perpendicular to the surface of that plane and two orthogonal gradiometers that measure the partial derivatives of B_z: $\frac{\partial B_z}{\partial x}$ and $\frac{\partial B_z}{\partial y}$ [72]. The gradiometers enable the reduction of the existent undesirable uniform sources. All of the sensors are held in liquid helium to maintain the temperature at 4.2 K so that they have the superconductivity in order to sense the weak magnetic fields produced by the brain sources [72].

4.2 FILTERING DEEP AND SUPERFICIAL PARTS

In all of the experiments, the dipole sources were produced using the spherically symmetric conductor model given in [15]. Sarvas' formula, SSS, exSSS and genexSSS methods were all implemented in Matlab® 7.0 environment with the aid of Fieldtrip toolbox. Matlab source codes for the genexSSS procedure are freely available at http://sites.google.com/site/neuronetsite.

4.2.1 Simulated data

A spherically symmetric head model [15] of radius $R = 9$ cm was utilized for the forward computations. The origin was accepted to be the center of the sphere that was found by a fitting to the sensor array volume. Two source dipoles were created at coordinates $\mathbf{r}_{deep} = (2, 3, -1)$ cm for the deep source and $\mathbf{r}_{sup} = (4, 5, 3)$ cm for the superficial source (Figure 6a). Notice that the radial distances of the dipoles from the origin are $||\mathbf{r}_{deep}|| = 3.7417$ cm and $||\mathbf{r}_{sup}|| = 7.0711$ cm. The sampling frequency was chosen as 1 KHz in the simulation. Duration of the field data is 400 ms, which corresponds to a data length of 400 samples. The deep dipole has no activity for 0-199 ms and it has sinusoidal waveform of 5 Hz for 200-399 ms (Figure 6b). Conversely, the superficial dipole has the sinusoidal activity for the interval 0-199 ms and it does not show any activity for the other half. Random Gaussian noise was added to simulated sources to give an *SNR* of 30 dB. Hence, the waveforms for both dipoles are exactly the same with the same amplitude but their activities are in different time intervals. This makes it easier to evaluate the performance of the suggested spatial filters. Superimposed responses from all sensors for the simulated MEG waveform are plotted in Figure 7. Notice that although the energies of the deep and superficial source waveforms are exactly the same, the resultant MEG data has much greater contribution from the superficial source than from the deep source. Since there are no external interferences for the synthesized data, it is unnecessary to implement the SSS expansion outside the head, i.e., we determined $L_{out} = 0$. In [60], it is experimentally shown (for the case of Elekta Neuromag® 306 channel system) that the upper limit for the inner expansion $L_{in} = 8$ is enough in order to sufficiently represent the dipolar sources that are not further than 8 cm from the origin. Note also that

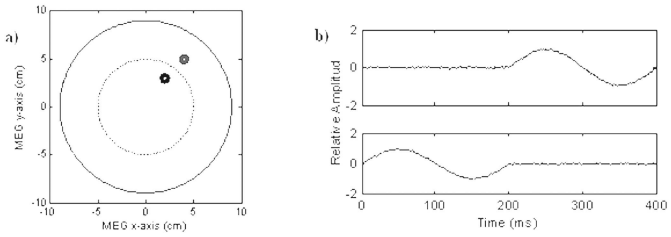

Figure 6: a) The locations of the simulated dipoles. b) Simulated waveforms of deep (top panel) and superficial (bottom panel) source dipoles. They are sinusoids of 5 Hz for different time intervals. The superficial source activity is for 0-199 ms and the deep source activity is for 200-399 ms.

choosing higher than this limit may cause unstable SSS basis matrices which are manifested as having high condition numbers. This makes the pseudo-inversion operation of the SSS basis matrices problematic for the extraction of the coefficients. Accordingly, the upper limit for the inner expansion was chosen as $L_{in} = 8$. Therefore, the dimension of the 306 channel magnetic measurement is reduced to $p_{in} = 80$. The estimated deep and superficial parts were computed using the exSSS method explained in Section 3.4.2. We define the energy of the MEG data as the sum of energies of all channels. In order to evaluate our algorithm quantitatively, we utilized various signal-to-noise ratios $SNR_{deep} = \frac{\sum_{k=1}^{M}\sum_{n=201}^{400}|b_k(n)|^2}{\sum_{k=1}^{M}\sum_{n=1}^{200}|b_k(n)|^2}$ and $SNR_{sup} = \frac{1}{SNR_{deep}}$ for the simulated data $\mathbf{b}$. Here k denotes the channel number, M=306 is the number of channels and n is the time index for the simulated MEG signal $\mathbf{b}$. Since the source activities for the dipoles arise for different time intervals, SNR_{deep} is computed by simply dividing the energy of the second half to the first one for all channels and similarly, SNR_{sup} is computed by obtaining the ratio of energy of the first half to the second for all channels. These signal-to-noise ratios of the estimated deep part $\hat{\mathbf{b}}_{deep}$ and the superficial part $\hat{\mathbf{b}}_{sup}$ are computed for different separating radii varying between $\hat{r} = 0.1$ and $\hat{r} = 8.9$ cm with increments of 0.1 cm. The SNR_{deep} of the simulated signal $\mathbf{b}$ is 0.1197. Figure 8a shows that the SNR_{deep} of the estimated deep part $\hat{\mathbf{b}}_{deep}$ decreases while the separating radius $\hat{r}$ increases. It takes the value around 0.3331 for $\hat{r} = 0.1$ cm and decreases until reaching to

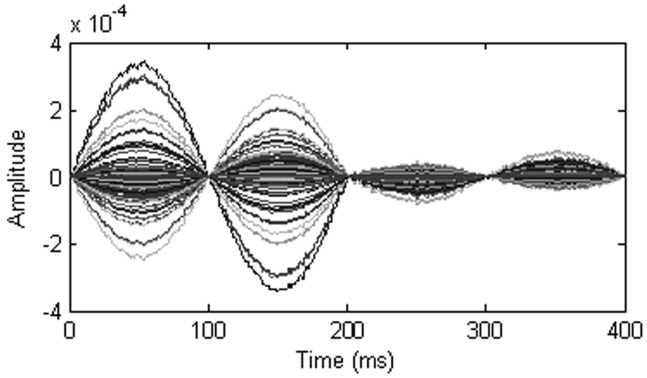

Figure 7: Overlapped channel waveforms for the simulated MEG signal from a superficial source dipole and a deeper source dipole that have exactly the same waveform. The energy of the response for the superficial part is much greater than the energy of the response for the deeper part.

0.1215 for $\hat{r} = 8.9$ cm, which is very close to SNR_{deep} of the original signal $\mathbf{b}$ as expected. The energy resulting from the superficial source is much more than the energy resulting from the deep source, so one cannot avoid some contamination from the superficial source as the separating radius increases. Consequently, the SNR_{deep} of $\hat{\mathbf{b}}_{deep}$ is greater than that of $\mathbf{b}$ regardless of the separating radius. The SNR_{sup} of the original simulated signal is 8.3518. The algorithm reaches the maximum $SNR_{sup} = 30.9761$ for $\hat{\mathbf{b}}_{sup}$ when $\hat{r} = 6.4$ cm, which is a boundary between the locations of the deep source and the superficial source (Figure 8b). Note that the SNR_{sup} of the estimated superficial signal is greater than that of the original signal $\mathbf{b}$, when the separating radius $\hat{r}$ is greater than 1.8 cm. The gain of the filter for the superficial part is much greater than the gain for the deep part as expected.

In Figure 9, we provide the algorithm outputs for one of the channels to exhibit its affect on the original magnetic field data. Note that the figures demonstrate the estimated signals $\hat{\mathbf{b}}_{deep}$ and $\hat{\mathbf{b}}_{sup}$ for $\hat{r} = 4$ cm and $\hat{r} = 7$ cm, respectively. In Figure 9a, it is observed that the deep part estimation causes the reduction of the strength of the superficial source contribution (0 ms-199 ms), while it enhances the deep source contribution (200 ms-399 ms). Figure 9b demonstrates the attenuation of the deep sinusoidal part for the estimated

superficial signal $\hat{\mathbf{b}}_{sup}$. Apart from the signal to noise ratios SNR_{deep}, SNR_{sup} and the waveforms, the spatial structure of the estimated deep and superficial signals is also one of the factors for the evaluation of the suggested algorithm. We used Elekta Neuromag® software in order to apply dipole fitting on $\hat{\mathbf{b}}_{deep}$ obtained with $\hat{r} = 4$ cm and on $\hat{\mathbf{b}}_{sup}$ obtained with $\hat{r} = 7$ cm. Note that the spherical volume conductor model was set for the forward computations utilized in the dipole fitting software. The locations of the fitted dipoles were found at (2.5034, 4.0897, 0.0226) cm for $\hat{\mathbf{b}}_{deep}$ and (4.8034, 6.1697, 3.2026) cm for $\hat{\mathbf{b}}_{sup}$, which yield root mean square localization errors as 1.5769 cm and 1.4334 cm, respectively.

We also applied the sharp spatial filtering given in Section 3.4.1 to the simulated data and provided the SNR_{deep} results for the estimated deep components in Figure 10 to compare with the exSSS results. It exhibits its step-wise dependency on $\hat{r}$ and gives evidence that its filtering performance cannot become better than that of the exSSS.

4.2.2 Phantom data

The simulations show that, the method extracts the superficial and deep waveforms reasonably well. However, a bias on the localization accuracy is also apparent from the dipole-fitting results described above. For a better understanding and evaluation of the algorithm on the basis of spatial bias and localization accuracy, we realized a phantom head experiment. This experiment reflects the more realistic conditions for the creation of the MEG data except that it does not contain the brain noise. The phantom consists of 32 artificial dipoles with known positions. The dipoles are activated by an internal signal generator. Since the system allows only one dipole activation at a time, we activated two separate dipoles sequentially, which are located at (5.97 0 2.29) cm and (3.58 0 2.55) cm and then regarded the addition of them to be the phantom signal as an input to the modified beamspace method. Note that these locations correspond to 6.4 cm and 4.4 cm distances from the center of the phantom, respectively and the radius of the cover is 8.75 cm. The deep dipole has a sinusoidal waveform of 20 Hz and is active for 50-150 ms while the superficial dipole has the same activity for 100-200 ms. Hence, between 100-150 ms, both of them are active. The amplitude of the deep dipole was chosen to be twice that of the superficial one.

An SSS expansion with $L_{in} = 8$ and $L_{out} = 1$ was applied to the data. We did not assign $L_{out} = 0$, because of the apparent small interference with the original data. A separating radius of $\hat{r} = 5$ cm was selected to apply the modified beamspace algorithm to the SSS inner component. Figure 11 demonstrates a sample channel of the original, the SSS filtered, the superficial dipole, the exSSS estimated superficial, the deep dipole and the exSSS estimated deep component signals. Figures 11c and 11d exhibit the waveforms for the original dipole and the estimated superficial component. As can be observed from them, the deep contribution was masked powerfully such that it cannot even be discerned from Figure 11d. Comparison of Figure 11e and Figure 11f implies that the deep component estimation cannot mask the part coming from the superficial dipole completely. Nevertheless, one may get an idea about how the SNR_{deep} is increased for the estimated deep component by comparing Figure 11a and Figure 11f, despite a more limited performance. This is not unexpected since the SNR_{sup} for the original signal $\mathbf{b}$ is 1.75, i.e., the contribution of the superficial component is much more than that of the deep one. Thus, deep source spatial filtering of the data cannot avoid some significant contamination arising from the superficial part.

We utilized the Elekta Neuromag® software with the spherically symmetric conductor volume to fit a dipole for the duration of the overlapped activity (100-150 ms). The locations of the fitted dipoles for the inner SSS component, the estimated deep component and the estimated superficial component are obtained from the software as (3.89 0.65 2.44) cm, (3.06 0.83 2.09) cm and (7.2 -0.95 3.51) cm, respectively. Note that these locations correspond to the radial distances 4.6377 cm, 3.7974 cm and 8.0661 cm with respect to the origin.

Consequently, the fitting results both for the simulated and the phantom head signal indicate a spatial bias toward deeper (further from the expansion origin) regions for the estimated deep component and more superficial (closer to the surface) regions for the estimated superficial component. The leadfields were not subjected to any kind of filtering for the dipole fitting experiments realized in this work. This imbalance between data and the leadfields may be one of the reasons that causes the localization bias. Hence, it would be a good idea to weight the computed leadfields depending on their location and depth parameters, for dipole fitting optimizations or imaging based inverse solutions.

4.2.3 Auditory evoked field data

We used auditory evoked field data acquired from a 32-year-old female. Pure sinusoidal tones per 1 second were utilized for the stimulation. The sampling frequency was 1 KHz and l20 epochs of 600 ms duration were averaged. As observed in Figure 12, the total average data exhibit two peaks: one at around 100 ms (the M100 peak) and the other one at around 200 ms (the M200 peak) [73]. For the sources located in the auditory cortical area, the M100 peak is usually utilized. When a current dipole is fitted using spherical conductor model with Elekta Neuromag® software for the M100 peak, the location of this dipole corresponds to (6.67, 1.54, 5.19) cm with respect to the SSS expansion origin and hence the radial distance for M100 is found to be 8.59 cm. The SSS coefficients were obtained with parameters $L_{in} = 8$ and $L_{out} = 3$. These parameters are accepted to be sufficient to capture the MEG data activity [60]. We used our algorithm exSSS to separate the cortical activity for a separating radius $\hat{r} = 8$ cm and $R = 11$ cm. After the coefficients were modified according to the beamspace formulation, the estimated deep and superficial parts were reconstructed by multiplying them with the inner SSS basis vectors. The estimated superficial part is plotted in Figure 13. It is observed that the estimated superficial part retains the auditory evoked potential. We provide the plotting of the deep part in Figure 14. As can be seen from it, the deep component captures some alpha wave activity in the occipital part and does not have significant auditory potential peak M100 as the estimated superficial component. We also used Elekta Neuromag® software in order to fit a dipole for the instant that M100 occurs for the deep and superficial components. The fitted dipole locations on the MR image are provided in Figure 13c and Figure 14c, for the superficial component and the deep component, respectively. These figures point out the effect of the decomposition for the auditory activity. The dipole for the estimated deep part deviates from the auditory cortical area as expected. On the other hand, the fitted dipole for the estimated superficial part is found to be at (6.46, 1.79, 5.44) cm with respect to the expansion origin, which means a radial distance of 8.63 cm between the fitted dipole and the origin. This is quite close to the dipole fitting results for the original signal at around 100 ms.

4.2.4 Imaging learning and reward system

An experiment was conducted in order to investigate the interactions related to human learning and reward system [74], which is known to consist of various cortical and subcortical regions such as prefrontal cortex, striatum and amygdala. The experiment was based on the paradigm described in [75], where the subjects are exposed to die rolls and requested to wager on them beforehand. Considerable activity changes in the neural regions accountable for the reward system had already been reported in [75] utilizing fMRI. However, the low temporal resolution of fMRI imaging does not allow to determine the interactions in millisecond level. Hence, we repeated the same type of experiment using MEG.

The averaged MEG data were spatially filtered by the exSSS to mask the effect of strong superficial sources. Then the source waveforms were reconstructed by sLORETA. Discernible activities were apparent from these waveforms as can be observed from Figure 15. It should be noted that the same activities could not be revealed without applying the exSSS as a preprocessing step. Hence, the preliminary results of this experiment yield the promise of our spatial filtering methods for the high temporal resolution investigations of deep brain activities.

4.3 FILTERING NON-CONCENTRIC PARTS INSIDE THE HEAD

4.3.1 Simulated data

The sampling frequency was chosen as 1 KHz in the simulations. A hypothetical sphere was fitted to the sensor array volume and the origin of the coordinate system was set at the center of this sphere. This origin is also accepted as the SSS expansion origin. Figure 16a schematizes the positions of the simulated dipoles. Three dipolar point sources were produced using Sarvas's formula [15] for spherically symmetric conductors: two dipoles d_1,d_2 located inside the head space at the same distance with respect to the origin and an external source dipole d_3. The locations of the dipoles d_1,d_2,d_3 are $\mathbf{r_1}$=(2,4,3) cm, $\mathbf{r_2}$=(-3,2,4) cm and $\mathbf{r_3}$ = (-400,-120,150) cm, respectively. It is worth noting that the radial distances of the first

two dipoles is $||\mathbf{r_1}|| = ||\mathbf{r_2}|| = 5.3851$ cm and the external dipole is $||\mathbf{r_3}|| = 4.43$ meters. We obviously choose the radial distances same for the inner sources in order to observe the resolving capability of the proposed method.

The simulated signal **bb** was generated by activating d_1 for 0-199 ms, d_2 for 200-399 ms and d_3 for 0-399 ms. Hence, the inner sources were activated for non-overlapped latency ranges and the external source was made active for the entire range. The waveforms of the inner sources are sinusoidal of 5 Hz, while the waveform of the external source was chosen as a sinusoidal of 2.5 Hz (Figure 16b). Some Gaussian noise of SNR=30 dB was added to the simulated signal for the sensor noise. The signal-to-interference ratio (SIR) is defined as the ratio of the energy arising from the inner sources to that arising from the external interferences. The SIR of the simulated MEG signal was 7.65 dB. It should be noted that the suppression capability of the SSS increases as the interference sources are located further from the sensor array and the SIR is smaller [60], [76]. In order to evaluate the performance of the filtering, we define two other signal-to-noise ratios particularly for the simulations:

$$SNR_{\mathbf{b_1}} = \frac{\sum_{k=1}^{M}\sum_{n=201}^{400}|bb_k(n)|^2}{\sum_{k=1}^{M}\sum_{n=1}^{200}|bb_k(n)|^2}$$

$$SNR_{\mathbf{b_2}} = \frac{1}{SNR_{\mathbf{b_1}}}.$$

Note that the magnetometers are amplified by 100 in all SNR and SIR computations to make their amplitudes comparable to those of the gradiometers. We denote the filtered signal corresponding to d_1 as $\mathbf{b_1}$ and that corresponding to d_2 as $\mathbf{b_2}$. The energies of d_1 and d_2 were chosen as equivalent, hence $SNR_{\mathbf{b_1}}(\mathbf{bb}) \approx SNR_{\mathbf{b_2}}(\mathbf{bb}) \approx 1$ for the simulated MEG signal. The aim of the genexSSS filtering is to increase $SNR_{\mathbf{b_1}}$ for $\mathbf{b_1}$ and similarly to increase $SNR_{\mathbf{b_2}}$ for $\mathbf{b_2}$ as much as possible.

For all of the experiments in the simulations, the genexSSS "expansion" parameters for are chosen as follows: We determine the inner expansion upper limit $L_{in} = 8$ (for $\mathbf{S}_{in}$ and $\tilde{\mathbf{S}}$) and the outer expansion upper limit $L_{out} = 3$ (for $\mathbf{S}_{out}$). These are suitable choices based on the other works about the application of the SSS algorithm [60],[76]. While for the ROI parameters ($\hat{r}$ and O′), in the first place in Section 4.3.1.1, we choose them arbitrarily

such that the ROI captures the targeted dipole while it excludes the other. In the second place in Section 4.3.1.2, we present a more optimal way of determining an ROI, in order to investigate the behavior of the genexSSS with respect to the ROI selection.

4.3.1.1 Filtering for arbitrary ROI's In order to filter the part corresponding to d_1, we set the origin of the ROI as O_1' at (1,3,2) cm 1 cm further from all three directions of its location $\mathbf{r_1}$. Notice that $||\mathbf{r_1} - O_1'|| = 1.73$ cm and $||\mathbf{r_2} - O_1'|| = 4.58$ cm, and hence the radius of the ROI would be some value between them for an appropriate use of the method. Accordingly, the radius of the ROI was selected as $\hat{r} = 2.5$ cm. The sensor radius was $R = 13.57$ cm. These parameters were used in (3.49) and the filtered signal $\mathbf{b_1}$ was obtained with the addition of data dependency in (3.52). In order to filter $\mathbf{b_2}$ corresponding to d_2, we replicated the same procedure assigning the same values to the parameters except changing the origin as O_2' at (-4,1,3) cm, i.e., it was set 1 cm further from all three directions of $\mathbf{r_2}$. Hence in this case, the distance between O_2' and the dipoles are $||\mathbf{r_1} - O_2'|| = 6.71$ cm and $||\mathbf{r_2} - O_2'|| = 1.73$ cm.

The *SNR*'s for these particular parameter values are given in Table 1, which shows that the simulated signal has almost same amount of contribution from d_1 as d_2. Utilizing the genexSSS filter with the selected ROI's enabled the energy of the targeted contribution to be twice more.

We provide three typical separate channels in Figures 17, 18 and 19. The amplitudes of the channels in all these figures are normalized for a better visual comparison and clearer understanding of the effect of the genexSSS filtering. In Figure 17a, it is observed that the simulated signal is severely affected by the external interference (the source d_3 in Figure 16a), especially in the second half (200-399 ms). Figure 17b depicts the same channel of $\mathbf{b}_{in}$ exhibiting that the SSS eliminates this interference contained in $\mathbf{bb}$. Figures 17c and 17d clearly show that the filtered signals $\mathbf{b_1}$ and $\mathbf{b_2}$ are not only free of the interference but the contribution of d_2 is also suppressed in the former and it is increased in the latter.

In Figure 18a, a channel that has a greater contribution from d_1 is exhibited. While it is observed from Figure 18b that the genexSSS filtering successfully decreases activity arising from d_2 for $\mathbf{b_1}$, Figure 18c shows that the strength of the same activity is relatively

increased for $\mathbf{b_2}$. Contrary to the channel presented in Figure 18a, an example channel that has a greater contribution from d_2 is provided in Figure 19a for a comparison. We see from Figure 19b that the activity arising from d_1 is increased to such a degree that its strength becomes more than the one arising from d_2. The same channel of the filtered signal $\mathbf{b_2}$ given in Figure 19c indicates that the contribution of the first half of the signal coming from d_1 is decreased.

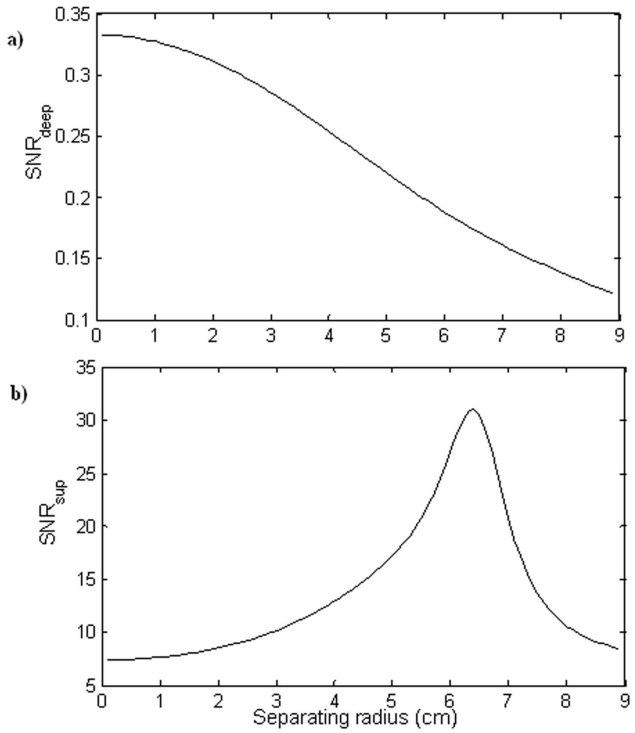

Figure 8: a) The change of SNR_{deep} for the estimated deep component when the separating radius $\hat{r}$ varies between 0.1 cm and 8.9 cm with the increments of 0.1 cm and with the sensor array radius R= 9 cm., b) The change of SNR_{sup} for the estimated superficial component when the separating radius $\hat{r}$ varies between 0.1 cm and 8.9 cm with the increments of 0.1 cm and with the sensor array radius R =9 cm.

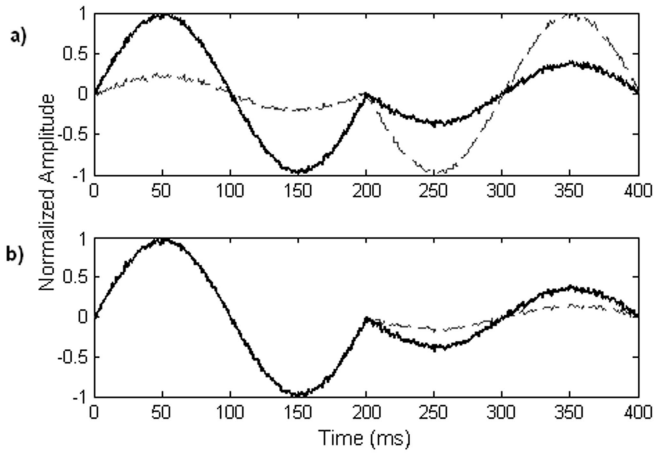

Figure 9: a) Original simulated MEG signal (solid) and the estimated deep component signal (dashed) for the 151^{th} channel, b) Original simulated MEG signal (solid) and the estimated superficial component signal (dashed) for the 151^{th} channel

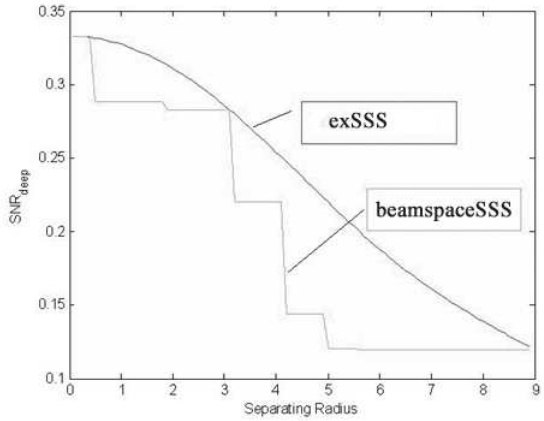

Figure 10: The change of SNR_{deep} for the estimated deep component both by the sharp filtering (beamspaceSSS) and exSSS. The separating radius $\hat{r}$ varies between 0.1 cm and 8.9 cm with the increments of 0.1 cm.

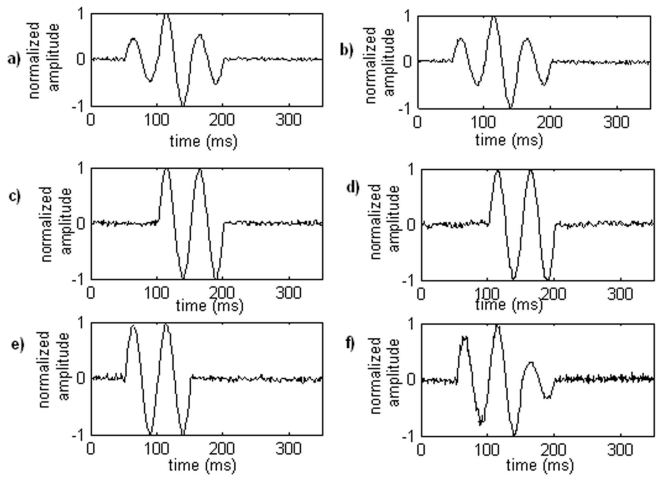

Figure 11: The waveform of the 163^{th} channel for a) Original phantom MEG data, b) SSS filtered phantom data for $L_{in} = 8$ and $L_{out} = 1$, c) The original superficial dipole of the phantom data in a), d) The estimated superficial component signal for $\hat{r} = 5$ cm, e) The original deep dipole of the phantom data in a), f) The estimated deep component signal for $\hat{r} = 5$ cm.

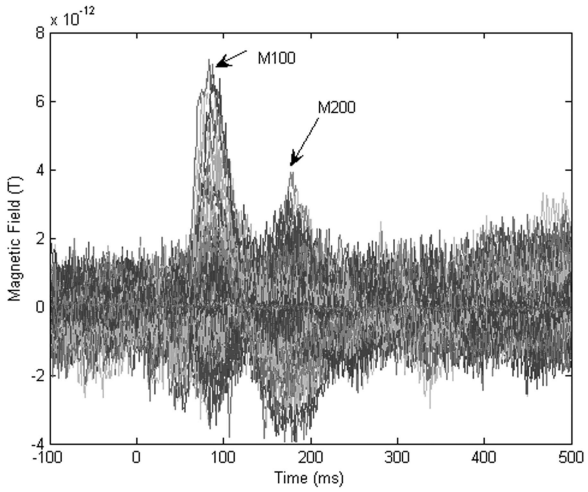

Figure 12: The overlapped measurements of the auditory evoked MEG channels for the sampling frequency of 1 KHz.

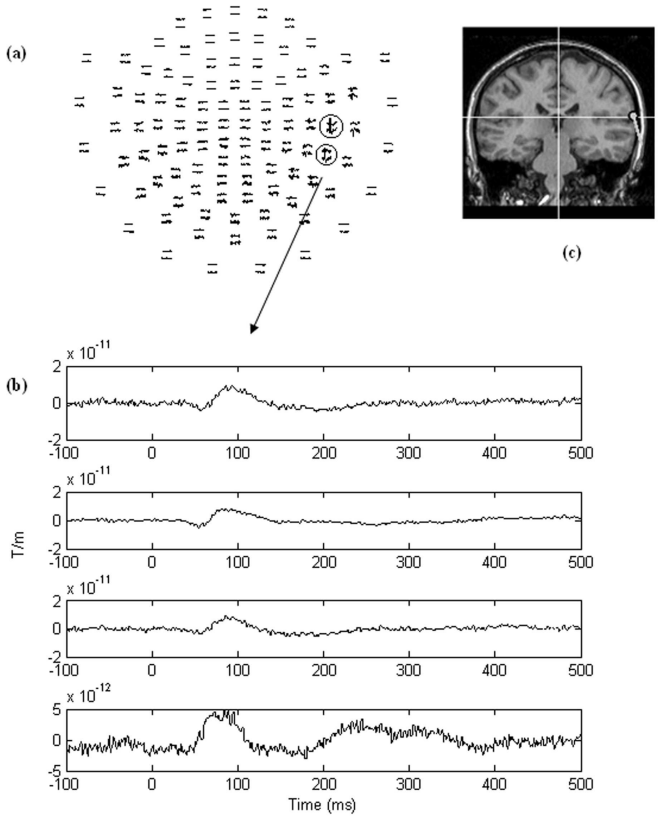

Figure 13: a) Channel layout for the estimated superficial component from the auditory evoked MEG data by the exSSS for a separating radius $\hat{r} = 8$ cm. b) The MEG waveforms for the sensors marked in a), which show auditory activity. c) Estimated location of the evoked potential on the MR image for the superficial component. The estimation is realized using Elekta Neuromag® dipole fitting software.

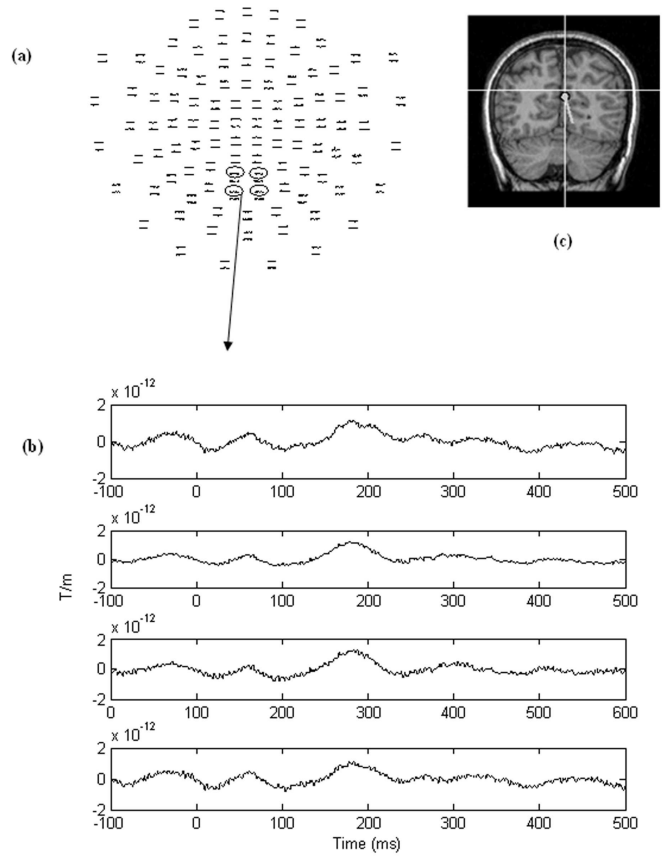

Figure 14: a) Channel layout for the estimated deep component from the auditory evoked MEG data by exSSS for a separating radius $\hat{r} = 8$ cm. The auditory evoked response is suppressed for the deep component. b) The MEG waveforms for the sensors marked in a). They show stronger alpha wave activity than the same sensors in the superficial component. c) Estimated location of the dipole (at around 95 ms) on the MR image for the deep component. The estimation is realized using Elekta Neuromag® dipole fitting software.

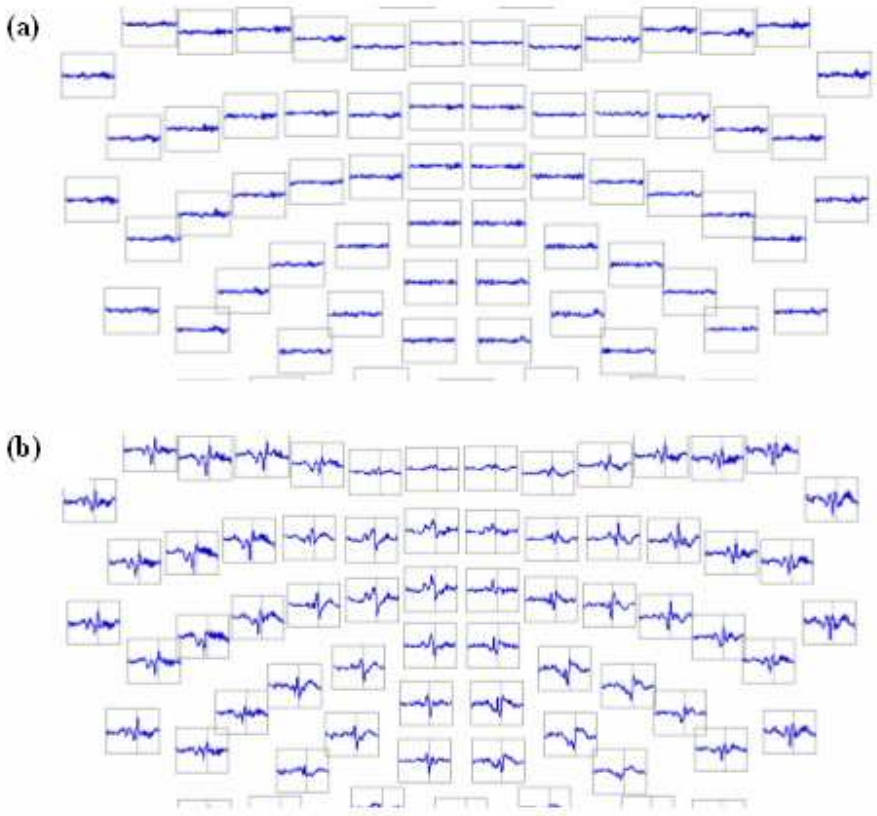

Figure 15: a)Some MEG channel waveforms related to the gambling experiment b) The same channel waveforms in a) except that they were filtered by the exSSS. Notice that the presence of significant activity between 200 ms and 350 ms was uncovered by the exSSS method.

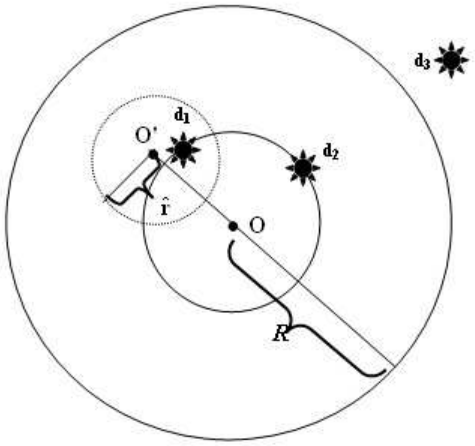

(a)

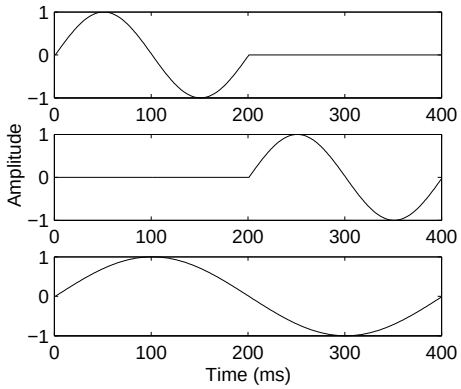

(b)

Figure 16: a) Two inner dipoles and one external dipole are simulated. The affect of the external source d3 to the simulated signal is diminished by the SSS. Since d_1 and d_2 are located with the same radial distance with respect to O, in order to filter d_1, a spherical ROI is constructed with a radius and a center O′. b) Waveforms of the simulated dipoles d_1 (top), d_2 (middle), d_3 (bottom). The inner sources d_1 and d_2 have the same sinusoidal waveform of 5 Hz but activated for different latencies. The waveform of the outer source is a sinusoidal of 2.5 Hz activated for the whole range.

Table 1: THE SIGNAL-TO-NOISE RATIOS OF THE FILTERED SIMULATED SIGNALS FOR THE RADIUS OF THE ROI $\hat{r} = 2.5$ cm

	SNR_{b_1}	SNR_{b2}
$\mathbf{b}_{in}$	1.0080	0.9921
$\mathbf{b}_1$	1.8562	0.5387
$\mathbf{b}_2$	0.4840	2.0659

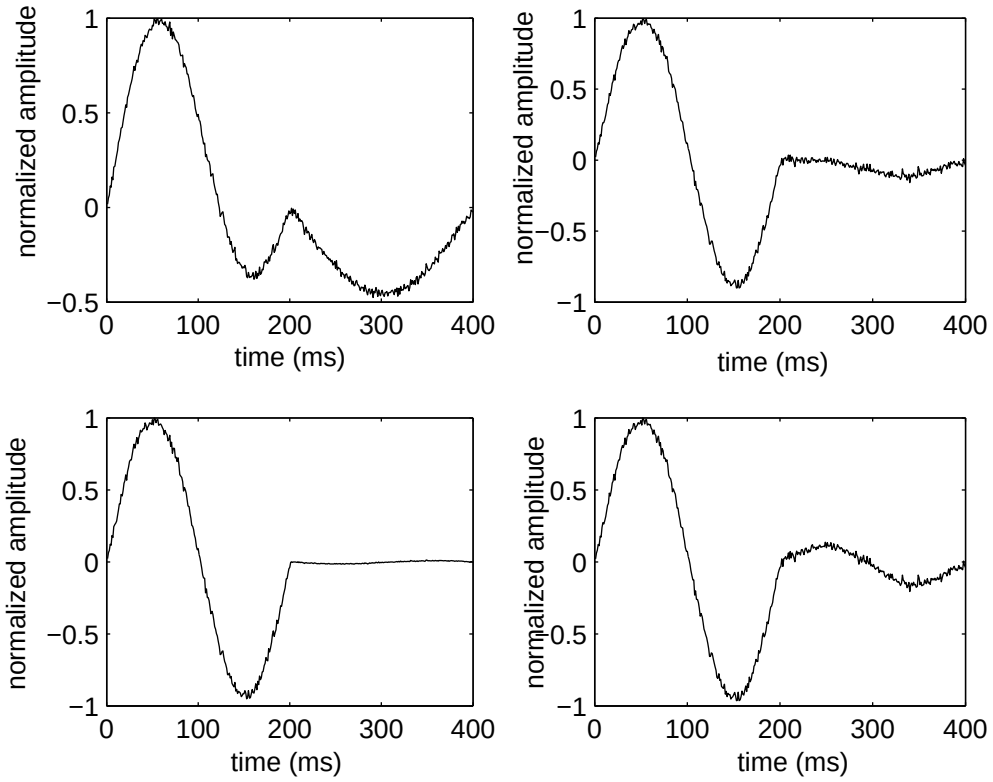

Figure 17: The normalized waveform of the 155^{th} channel of a) the original simulated data **bb**, b) the SSS filtered data $\mathbf{b}_{in}$, c) the filtered data $\mathbf{b_1}$ corresponding to the ROI with the origin O_1' set at (1,3,2) cm and radius $\hat{r} = 2.5$ cm, d) the filtered data $\mathbf{b_2}$ corresponding to the ROI with the origin O_2' set at (-4,1,3) cm and the radius $\hat{r} = 2.5$ cm.

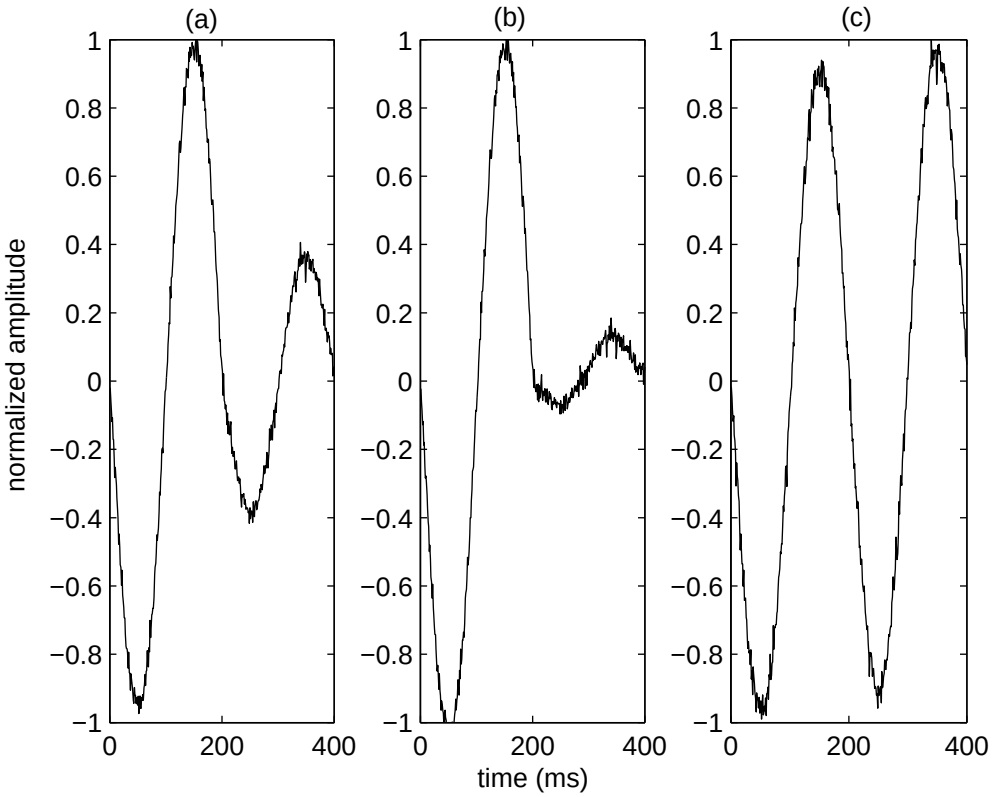

Figure 18: The normalized waveform of the 64^{th} channel for a) the original simulated data **bb**. It has a greater contribution from d_1. b) the filtered data $\mathbf{b_1}$ corresponding to the ROI with the origin O_1' set at (1,3,2) cm and radius $\hat{r} = 2.5$ cm. The energy of the first half stemming from d_1 is increased. c) the filtered data $\mathbf{b_2}$ corresponding to the ROI with the origin O_2' set at (-4,1,3) cm and radius $\hat{r} = 2.5$ cm. The energy of the second half is increased.

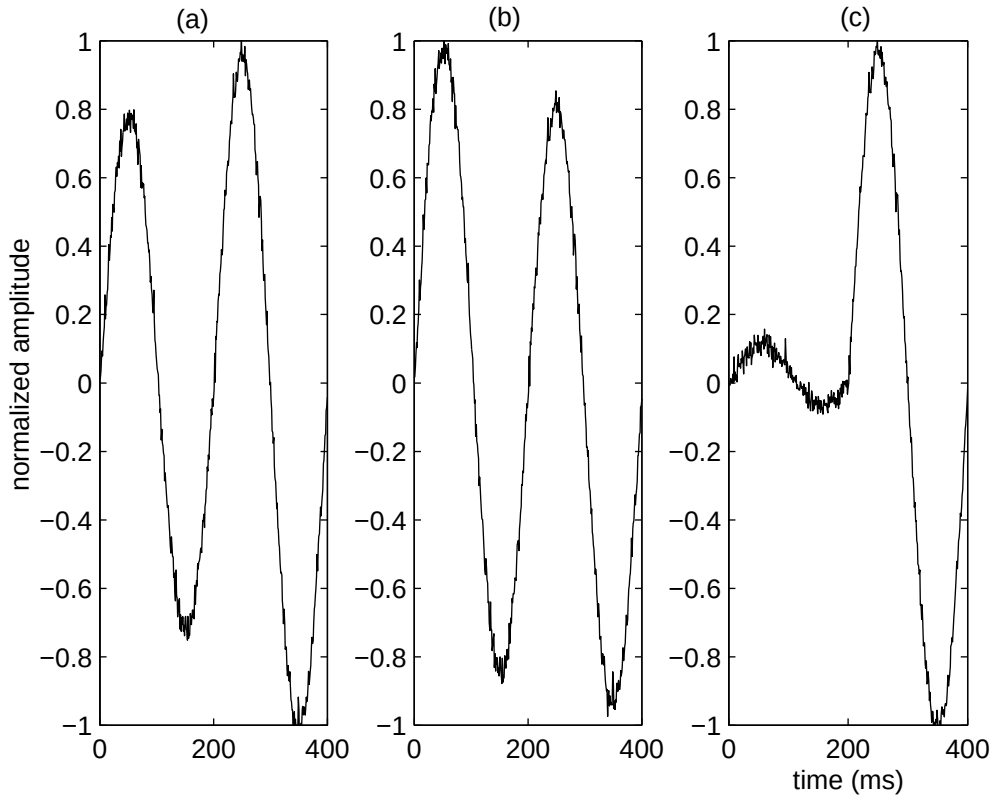

Figure 19: The normalized waveform of the 85^{th} channel for a) the original simulated data **bb**. It has a greater contribution from d_2. b) the filtered data $\mathbf{b_1}$ corresponding to the ROI with the origin O_1' set at (1,3,2) cm and radius $\hat{r} = 2.5$ cm. The energy of the first half stemming from d_1 is increased. c) the filtered data $\mathbf{b_2}$ corresponding to the ROI with the origin O_2' set at (-4,1,3) cm and radius $\hat{r} = 2.5$ cm. The first half that is coming from d_1 is suppressed.

4.3.1.2 Sensitivity to the ROI parameters For a proper genexSSS filtering of the signal corresponding to one of the dipoles, the ROI is expected to encapsulate that particular dipole while excluding the other dipole to be masked. In other words, $\hat{r}$ should be chosen as greater than the distance of O$'$ from the location of the targeted source and less than the distance of O$'$ from the location of the undesired source, i.e., for instance, if one would like to filter the signal $\mathbf{b_1}$ corresponding to d_1, then $||\mathbf{r_1} - O'|| < \hat{r} < ||\mathbf{r_2} - O'||$ should be satisfied. Hence, there exist theoretically infinite possible choices on the ROI parameters O$'$ and $\hat{r}$ for a filtering by genexSSS. In simulations, we restrict the location of the ROI by considering O$'$ to be on the line that passes through both $\mathbf{r_1}$ and $\mathbf{r_2}$. This line is illustrated in Figure 20. The coordinates of O$'$ in the direction of dir_1 can be found out by the equation:

$$O'_1(x, y, z) = \frac{(p+q)\mathbf{r_1} - p\mathbf{r_2}}{q} \tag{4.1}$$

where $p = ||\mathbf{r_1} - O'||$ and $q = ||\mathbf{r_1} - \mathbf{r_2}|| = 5.47$ cm . Note that the equation (4.1) can be simply modified in order to determine the centers of the ROI in the direction of dir_2 for filtering the signal corresponding to the dipole d_2. Choosing a direction dir_1 for O$'$ when filtering for d_1 (or dir_2 for filtering d_2) enables the minimum ratio of $||\mathbf{r_1} - O'||/||\mathbf{r_2} - O'||$ (or alternatively $||\mathbf{r_2} - O'||/||\mathbf{r_1} - O'||$), which is desirable for a better separation, since one would like to have the ROI as distant as possible to the unwanted sources while making it as close as possible to the targeted sources. This clearly explains why we restrict the ROI center selections on the line depicted in Figure 20. We varied p between 0.01 cm and 5.01 cm with the increments of 0.5 cm in the direction of dir_1 to determine values for O$'$ and for each O$'$, we assigned various values of $\hat{r}$ between 0.1 cm and 8.9 cm with the increments of 0.1 cm. These parameters were substituted in (3.49) and the filtered signal $\mathbf{b_1}$ was obtained with the addition of data dependency in (3.52) for all determined ROI's. In Figure 21a, we provide the $SNR_{\mathbf{b_1}}(\mathbf{b_1})$ for the selected ROI's to exhibit the method's sensitivity to O$'$ and $\hat{r}$. It is observed that as the center of the ROI gets farther from d_2, the filtering performance increases up to a limit, in this case p=2.51 cm. However, the $SNR_{\mathbf{b_1}}$ degrades for p=3.01 cm and for $p \geq 3.51$ cm, it is seen that the $SNR_{\mathbf{b_1}}$ starts decreasing even below 1 and hence the filter loses its suppression capability. Notice that the $SNR_{\mathbf{b_1}}$ curves take their maximum at a value $\hat{r}$, where $||\mathbf{r_1} - O'|| < \hat{r} < ||\mathbf{r_2} - O'||$. It is also worth noting these

experiments indicate that an optimal selection of O′ and $\hat{r}$ may give rise to a considerable improvement on the suppression performance as up to $SNR_{\mathbf{b_1}} = 7.413$ in our example. This is a much greater performance when compared with the result for arbitrarily selected ROI's in Section 4.3.1.1, where the filtering could only lead to $SNR_{\mathbf{b_1}} \approx 2$.

The degradation of the method for p values bigger than 3.01 cm is caused by the instability of the matrix $\tilde{\mathbf{S}}$ occurring as $||O - O'||$ gets larger. The condition number of a matrix yields an estimate of accuracy for the pseudo-inversion of it. For the case of $\tilde{\mathbf{S}}$, the condition number depends on both L_{in} and $||O - O'||$. Since $L_{in} = 8$ is fixed, the only parameter that changes it is O′. Figure 21b shows the condition numbers of $\tilde{\mathbf{S}}$ with respect to p, which determines the position of O′. It is observed that the condition number starts increasing enormously for $p \geq 3.01$ cm.

In Figure 22, we yield the overlapped channel waveforms of the simulated signal **bb**, SSS-filtered signal $\mathbf{b_{in}}$ and genexSSS-filtered signal $\mathbf{b_1}$ with $\hat{r} = 5.3$ cm and $p = 2.51$ cm [O′=(4.29, 4.92, 2.54) cm] that resulted the maximum $SNR_{\mathbf{b_1}}$. Figures 22a and 22b show that the SSS method eliminates the low-frequency sinusoidal signals that were caused by the external dipole d_3. While the comparison of Figures 22b and 22c gives evidence how the signal between 200-399 ms is masked by the genexSSS for $\mathbf{b_1}$, apart from being interference free. In Figure 23a, we give a sample channel to exhibit how the genexSSS filtering successfully decreases activity arising from d_2 for $\mathbf{b_1}$.

We assigned various values of O′ (this time in the direction of dir_2) and $\hat{r}$ in order to obtain estimates $\mathbf{b_2}$. The obtained $SNR_{\mathbf{b_2}}$ values for these ROI's showed that the performance of the filter for $\mathbf{b_2}$ had a similar tendency with the previous results for $\mathbf{b_1}$. That is, when the distance $||O - O'||$ is greater than around 6 cm, the filter output is likely to have degeneracy because of a high singularity of the matrix $\tilde{\mathbf{S}}$. This singularity is caused by the imbalance in the components of $\tilde{\mathbf{S}}$, since the origin O′ gets too close to some of the sensors while it becomes too distant from some other sensors. Thus, the genexSSS (similarly to the SSS for the case of $\mathbf{S_{in}}$) should be used with special caution to the condition number of $\tilde{\mathbf{S}}$ while the ROI is being determined.

Figure 23b depicts a sample channel for an estimated $\mathbf{b_2}$ with $||\mathbf{r_2} - O'|| = 2.01$ cm and $\hat{r} = 6.3cm$, which shows that the strength of the activity corresponding to d_1 is decreased while the second half arising from d_2 is preserved.

While we evaluated the genexSSS based on its "noise" suppression capability, the maintenance of the spatial structure of the inputs is also a highly desired property of a spatial filter. Figure 24 exhibits the imaged amplitudes of $\mathbf{b_{in}}$ and the genexSSS outputs $\mathbf{b_1}$ and $\mathbf{b_2}$ for all channels. It is observed that not only the components corresponding to the non-ROI regions (200-399 ms for $\mathbf{b_1}$ and 0-199 ms for $\mathbf{b_2}$) were suppressed from the data, but the spatial structure of the desired components was also successfully preserved.

4.3.2 Real data

Bilateral auditory evoked fields have been in interest of many MEG studies [77]. In this study, the auditory evoked field data was acquired from a 50 year-old male subject with pure tones as stimuli. The observed data were obtained with a sampling frequency of 1 KHz. The duration of each trial was 600 ms and 150 trials were averaged. The whole-channel averaged data is provided in Figure 25. Difficulty arises for the estimation of the bilateral auditory cortical sources when the well-known inverse techniques such as dipole fitting and linearly constrained minimum variance beamformers are applied directly without any special care [77], [78]. The failures of these methods are mainly due to the temporal overlapped activities in distinct locations and the strong correlations between the sources causing a significant leakage in particular for the beamformers. In order to overcome these limitations, one simple way is to determine some important sensors for each hemisphere of the brain and realizing the techniques only for these selected sensors. However, this leads to limited accuracies of source location estimations and source waveform reconstructions since the selected sensors have always some contributions from the other regions. Apart from this, the use of null constraints for the excluded regions was also suggested particularly for the beamformers [78].

In this section, we demonstrate the realization of the genexSSS filter for the separation of the signal corresponding to two specified ROI's in each hemisphere. The origins of these

ROI's were selected as the dipole locations obtained by Elekta Neuromag® software using a spherical conductor head model. The sensors were divided into two parts for each hemisphere and the dipole fitting was realized only for these subsets of the sensors at around the M100 peak occurring at 100 ms. The estimated locations obtained from these subsets were (-5.19,-1.93, 2.10) cm for the left hemisphere and (4.80,-0.61 ,2.20) cm for the right hemisphere. Notice that as mentioned above, these results may not be accurate due to the selection of the sensors which have contributions from the contralateral activities. However, taking these crude approximate results as the origins of ROI's is sufficient to roughly determine the necessary spherical ROI's for the spatial filtering.

The radii for both ROI's were selected to be $\hat{r} = 6$ cm and the sensor array radius was $R = 13.5$ cm. The schematic representations of the ROI's named as ROI_{left} and $\text{ROI}_{\text{right}}$ are given in Figure 26. The spherical basis expansion parameters were chosen as $L_{in} = 8$, $L_{out} = 3$. These parameters were incorporated into the genexSSS filter with the inclusion of the data-dependent signal space projection and the filtered signals $\mathbf{b}_{left}$ and $\mathbf{b}_{right}$ were obtained for the ROI_{left} and $\text{ROI}_{\text{right}}$, respectively.

Figure 27 shows all the gradiometers for $\mathbf{b}_{left}$, while Figures 28(a) and 28(b) exhibit the channels that were marked by the rectangles in Figure 27. It is observed that the auditory peaks in the channels close to the left hemisphere were retained, while the same activities for the channels in the proximity of the right hemisphere were successfully reduced. One of the sample channels is provided in Figure 29 to show the typical effect of the genexSSS on the signal.

Similarly, Figures 30, 31 and 32 exhibit the gradiometers of $\mathbf{b}_{right}$ in various levels. They indicate that the amplitudes of auditory activities coming from the left hemisphere were decreased, while those arising from the right hemisphere were preserved for the filter output $\mathbf{b}_{right}$.

We also applied dipole fitting on the filtered MEG signals, this time covering all of the sensors. The estimated locations of the fitted dipole for $\mathbf{b}_{left}$ and $\mathbf{b}_{right}$ were found at (-5.11,-0.32,3.03) cm and (4.67,0.90,1.61) cm, respectively. These resulted locations indicate that one can reach similar localization estimates for the each bilateral auditory evoked source without having to fit the dipoles for user-selected sensors from the original data.

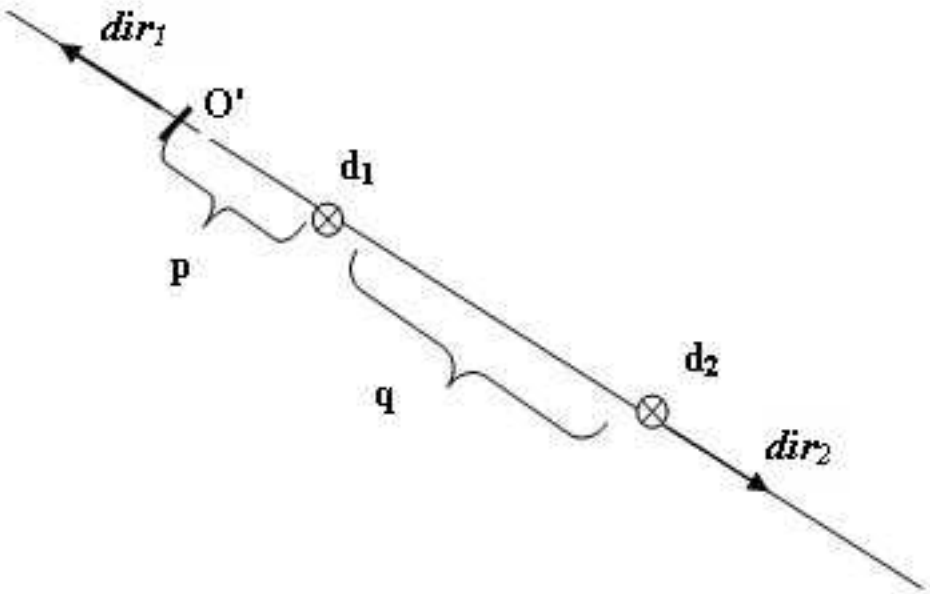

Figure 20: The ROI's whose centers O' were selected to be on the line connecting d_1 and d_2. This minimizes the ratio of the distance $||\mathbf{r_1} - O'||/||\mathbf{r_2} - O'||$ for spatially filtering the signal corresponding to d_1 and the distance $||\mathbf{r_2} - O'||/||\mathbf{r_1} - O'||$ for spatially filtering the signal corresponding to d_2.

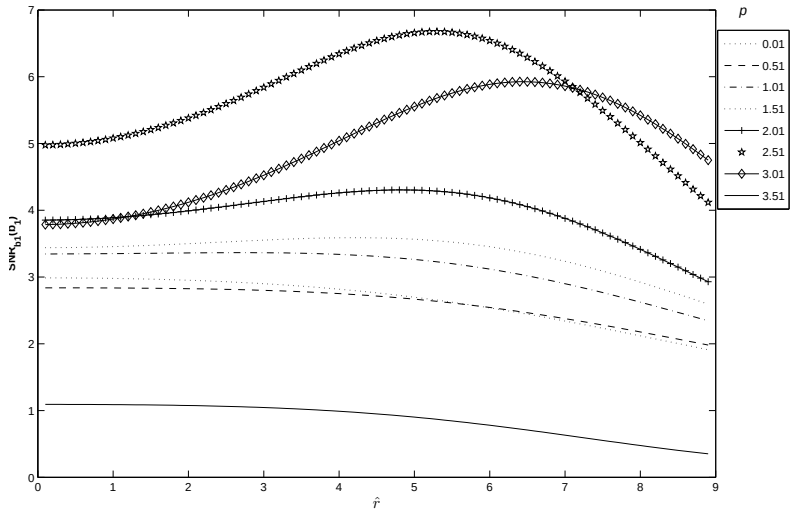

(a)

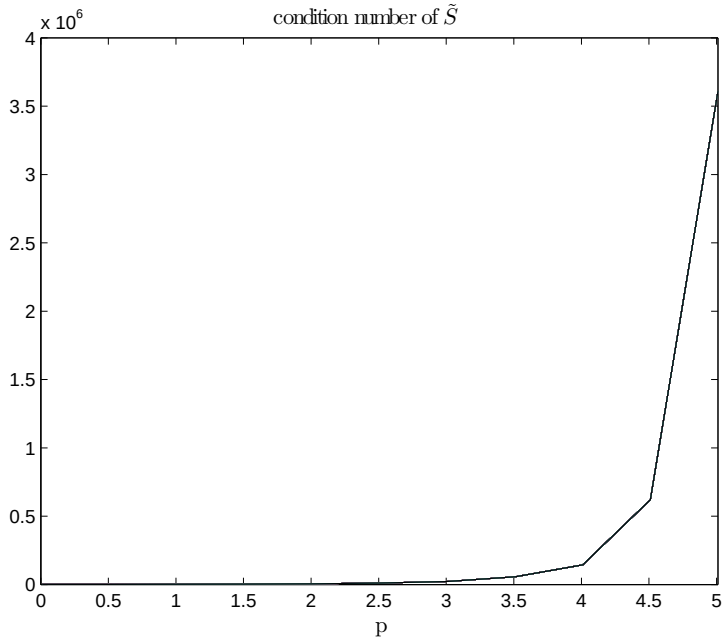

(b)

Figure 21: a) The change of $SNR_{\mathbf{b_1}}$ for different ROI's whose centers were chosen on the line passing through d_1 and d_2, while their radii were varied between $\hat{r} = 0.1$ cm and $\hat{r} = 8.9$ cm with the increments of 0.1 cm. b) The condition number of $\tilde{\mathbf{S}}$ with respect to the parameter p, which determines the center of ROI placed on the line given in Figure 20. The genexSSS filtering performance given in (a) starts declining for $p > 2.51$ cm because of the increase of the condition number for that range.

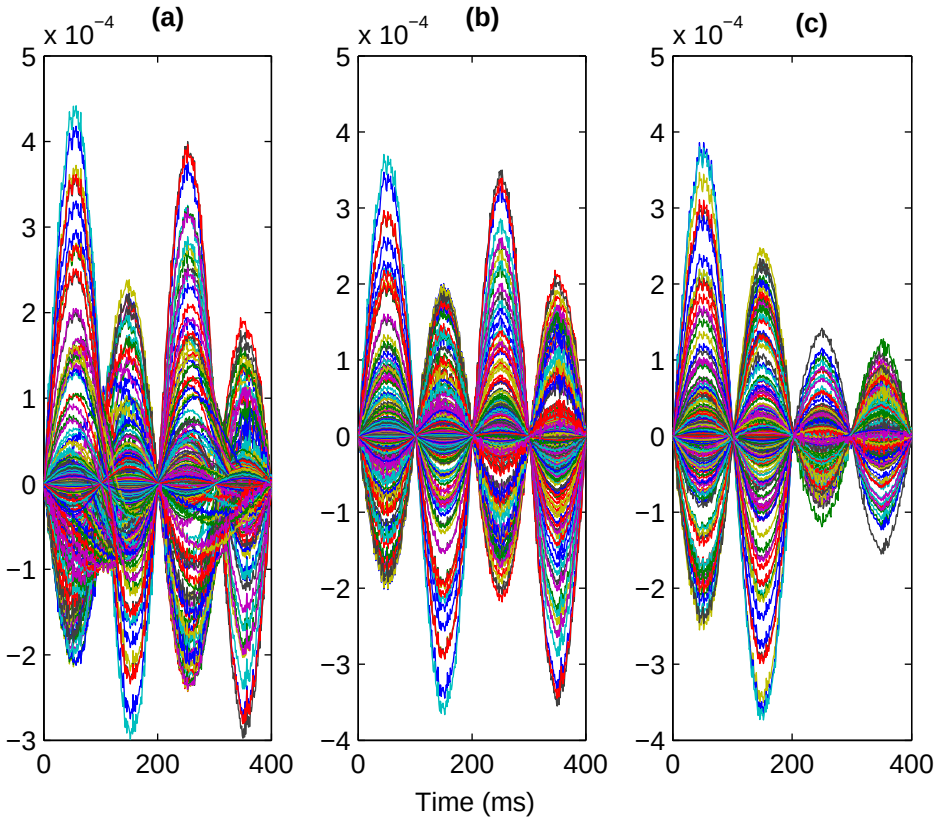

Figure 22: Overlapped channel waveforms a) for the simulated data **bb** which was created by three dipoles d_1, d_2, d_3: two inner dipoles d_1 and d_2 that have exactly the same energy and located at the same distance with respect to the SSS expansion origin, and another dipole d_3 outside the head space, b) SSS filtered data $\mathbf{b}_{in}$ obtained by selecting the expansion upper limits as $L_{in} = 8$ and $L_{out} = 3$. It is free of the external noisy part arising from d_3, c) genexSSS filtered $\mathbf{b_1}$ with a selected ROI that has the origin O′ at (4.29, 4.92, 2.54) cm and with the radius $\hat{r} = 5.3$ cm. The energy of the second part arising from d_2 is masked.

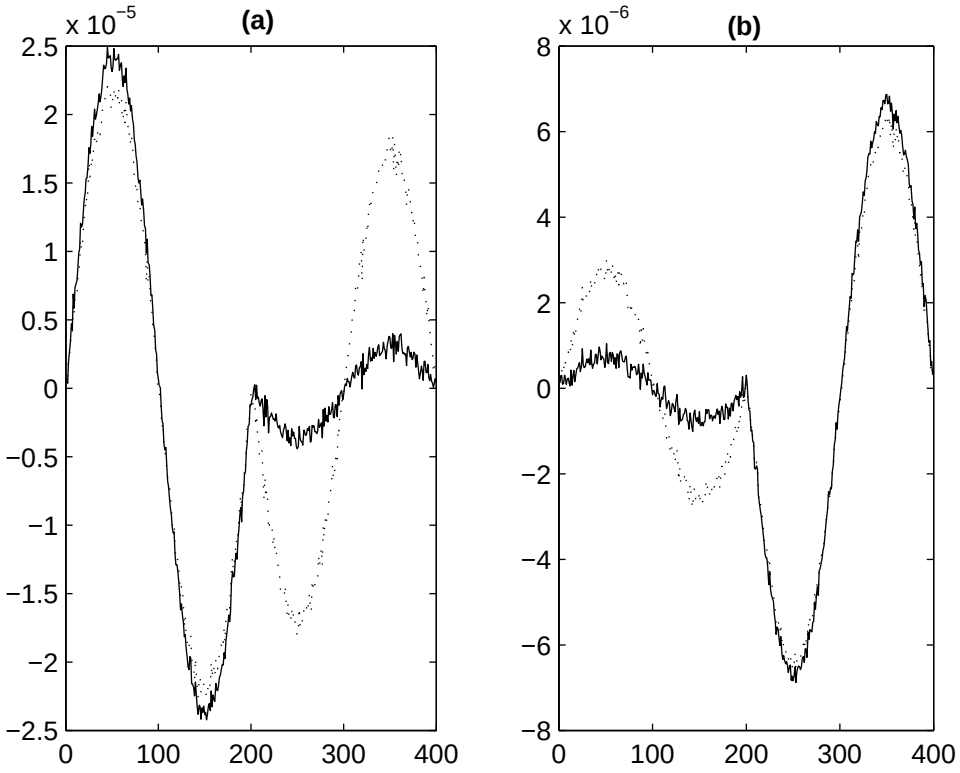

Figure 23: a) The waveform of the 251^{th} channel for the original simulated data **bb** (dotted) and the genexSSS filtered data $\mathbf{b_1}$ (solid) corresponding to the ROI with the origin O′ set at (4.29, 4.92, 2.54) cm and the radius $\hat{r} = 5.3$ cm. The energy of the second half stemming from d_2 is suppressed while the first half corresponding to d_1 is preserved. (b) The waveform of the 158^{th} channel for the original simulated data **bb** (dotted) and the genexSSS filtered data $\mathbf{b_2}$ (solid) corresponding to the ROI with the origin O′ set at (-4.83, 1.27, 4.37) cm and the radius $\hat{r} = 6.3$ cm. This time the energy of the first half is suppressed and the second half corresponding to d_2 is preserved.

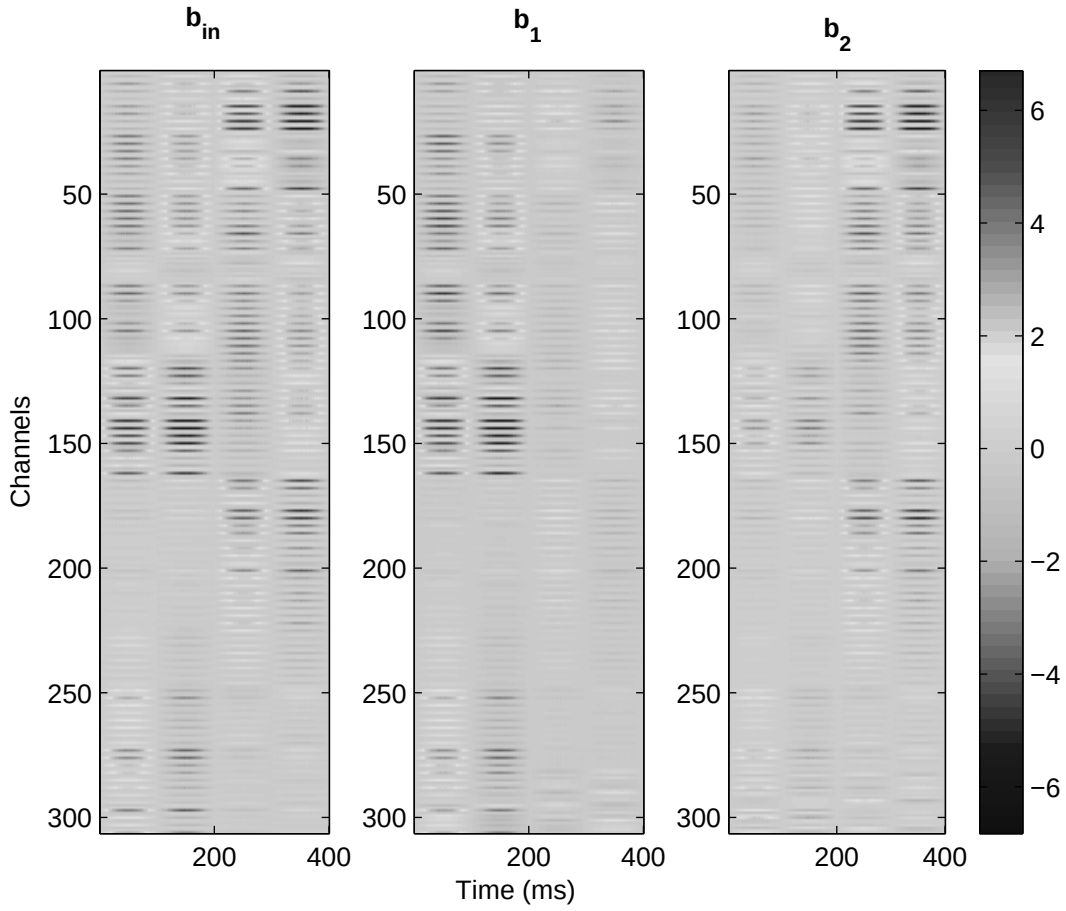

Figure 24: The images for normalized $\mathbf{b_{in}}$,$\mathbf{b_1}$ and $\mathbf{b_2}$. The energy of the unwanted part coming from d_2 (d_1) is reduced while the spatial complexity coming from $d_1(d_2)$ is preserved for $\mathbf{b_1}$ ($\mathbf{b_2}$).

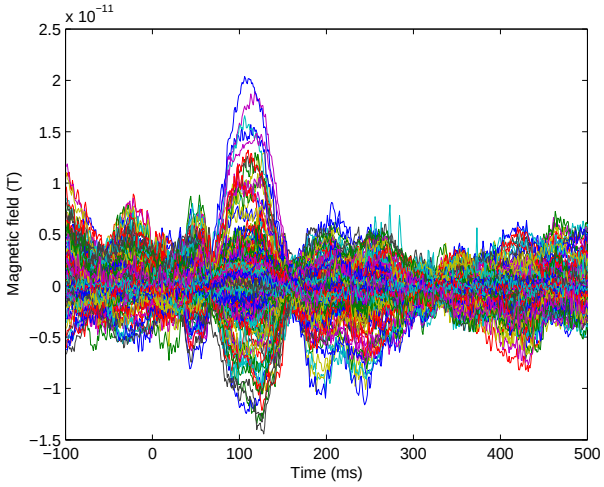

Figure 25: Overlapped bilateral auditory evoked magnetic field measurements with the sampling frequency of 1 KHz.

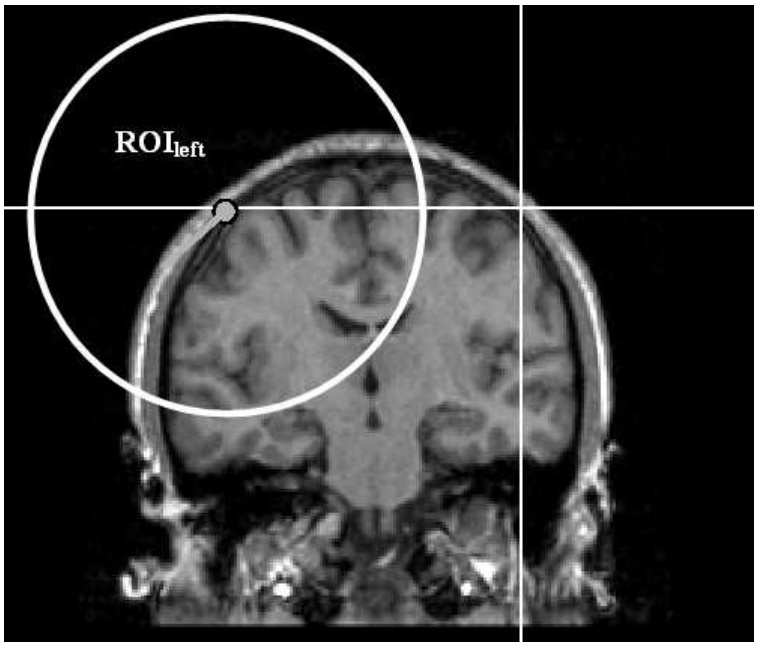

(a)

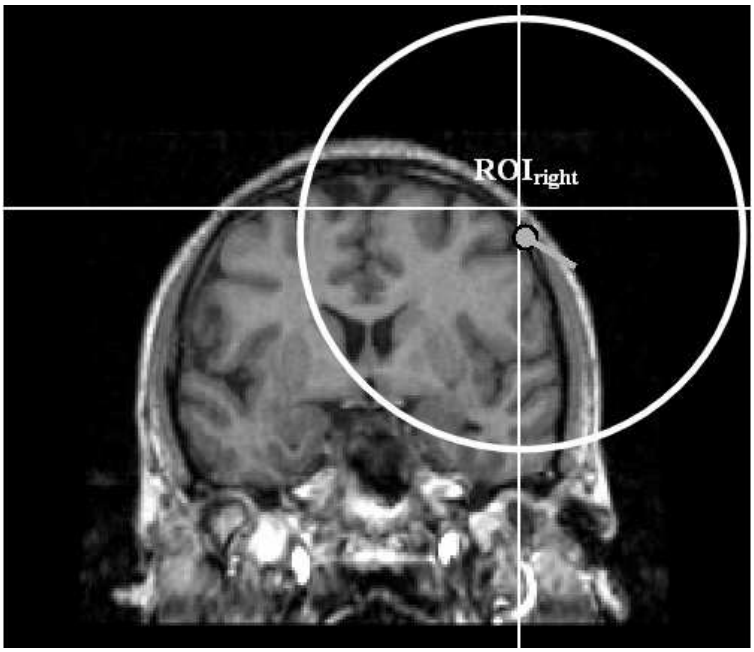

(b)

Figure 26: The fitted dipoles for the sensors covering a) only the left hemisphere and b) only the right hemisphere. The estimated locations of the dipoles are utilized for setting the origins of $\mathrm{ROI}_{\mathrm{left}}$ and $\mathrm{ROI}_{\mathrm{right}}$ in order to accentuate the data arising from that hemisphere and suppressing the part arising from the contralateral part.

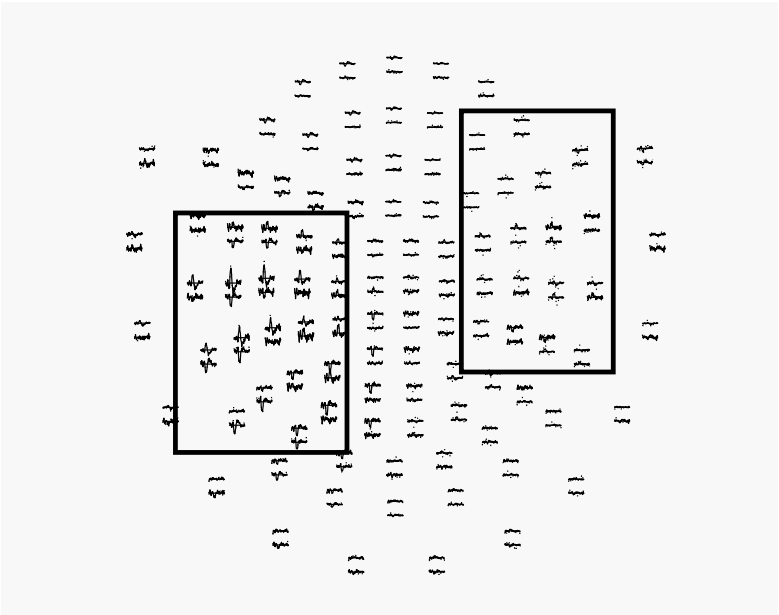

Figure 27: Channel layout of gradiometers for the filtered signal $\mathbf{b}_{left}$ corresponding to ROI_{left}.

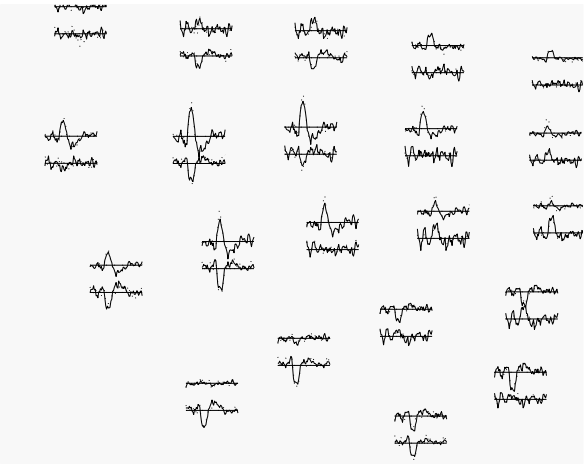

(a) The filtered signals (solid) and the original signals (dashed) from the channels that were marked by the box on the left handside in Figure 27. The filtering on the ROI_{left} retains the signals from the left hemisphere.

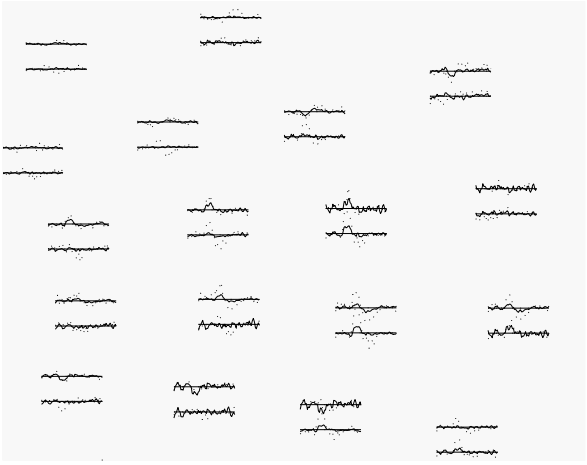

(b) The filtered signals (solid) and the original signals (dashed) from the channels that were marked by the box on the right handside in Figure 27. The auditory evoked fields arising from the right hemisphere are suppressed by the filtering.

Figure 28: Zoomed in waveforms for $\mathbf{b}_{left}$

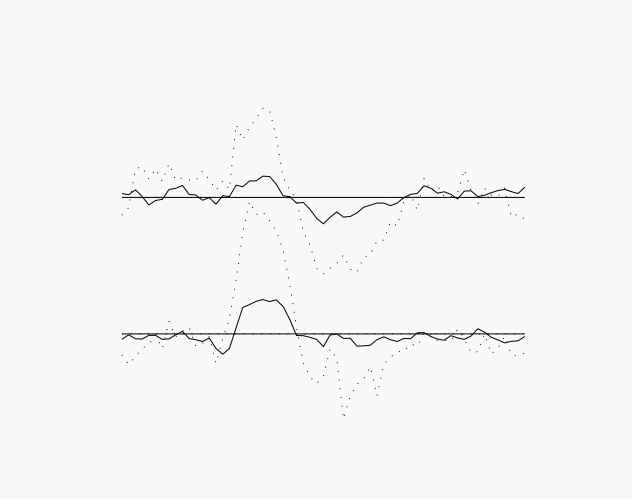

Figure 29: One of the channels in Figure 28(b). The filtered signals are solid and the original signals are dashed.

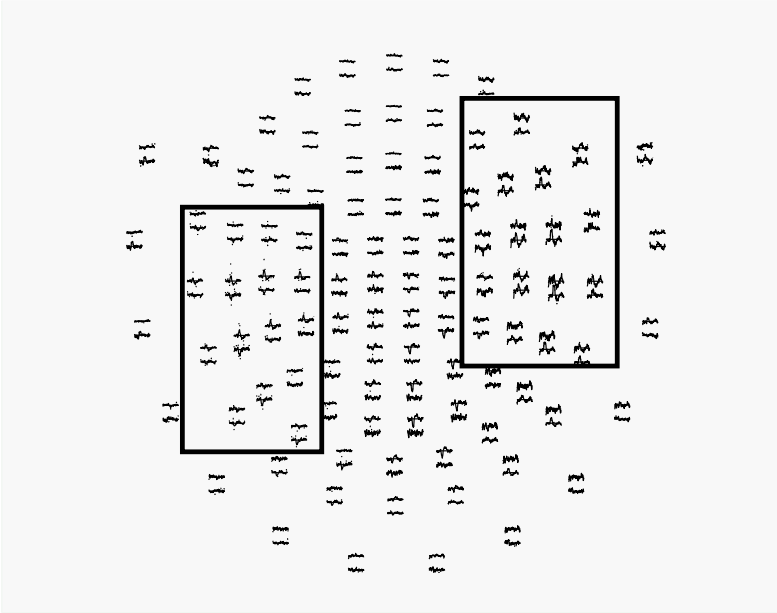

Figure 30: Channel layout of gradiometers for the filtered signal $\mathbf{b}_{right}$ corresponding to ROI_{right}.

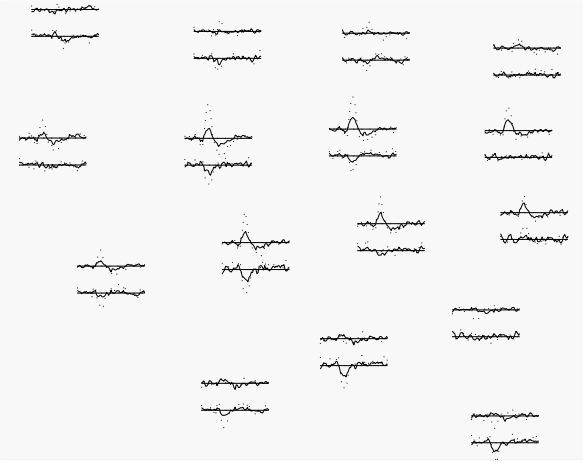

(a) The filtered signals (solid) and the original signals (dashed) from the channels that were marked by the box on the left handside in Figure 30. The filtering enables suppressing the auditory evoked peaks for these channels.

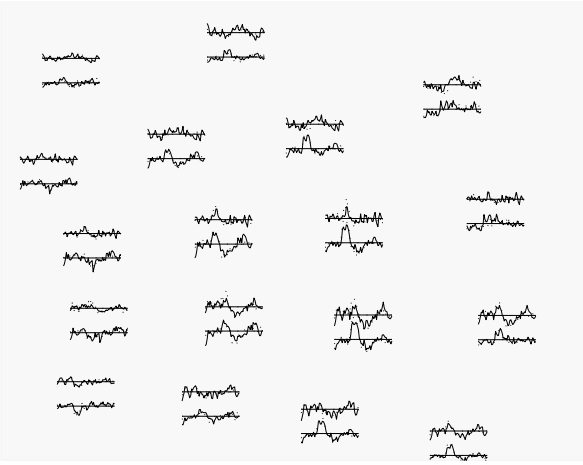

(b) The filtered signals (solid) and the original signals (dashed) from the channels that were marked by the box on the right handside in Figure 30. The original signals of the right channels are preserved.

Figure 31: Zoomed in waveforms for $\mathbf{b}_{right}$

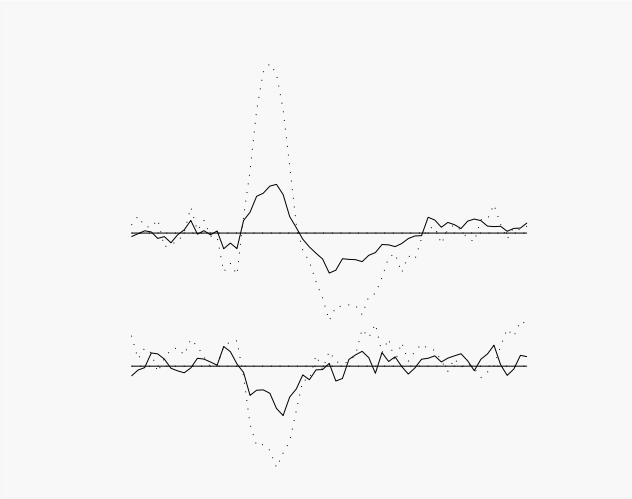

Figure 32: One of the channels in Figure 31(a). The filtered signals are solid and the original signals are dashed.

5.0 CONCLUSION

5.1 CLASSIFICATION AND SUMMARY OF THE FILTERS

Our filters, both exSSS and genexSSS, can be considered under the title of "optimum linear filters". These types of estimators share some common steps as described in [79]:

1. Computational structure with well-defined parameters: We choose the spherical harmonics domain for the computational structure. Hence, the inputs of the filters are the inner SSS coefficients $\boldsymbol{\alpha}$ and we aim to find a linear estimator that transforms $\boldsymbol{\alpha}$ to the output parameters $\hat{\boldsymbol{\alpha}}_f$ corresponding to a user-specified ROI. The block diagram of the structure of the filters is depicted in Figure 33.
2. Selection of a performance criterion: The criterion is based on the maxSNR beamspace methodology, which aims at maximizing the energy for the signals arising from the ROI, while minimizing it for the remaining source regions. The beamspace criterion allows the minimization of the mean-squared-error[55]. There is not any specific assumption on either source distribution or data statistics.
3. Optimization of the performance criterion: The solution of the optimization is obtained using a Lagrange multipliers technique, which leads to the eigendecomposition of the Gram matrix. The Gram matrix represents the second-order relations between the vector spherical harmonic functions and it is found by an integration throughout the targeted source regions. The analytical solution gives rise to explicit spatial filter designs due to the orthogonality of the vector spherical harmonics. Moreover, the obtained optimal coefficients are weighted by the eigenvalues of the Gram matrix for a filter expressing better performance.

4. Evaluation based on the performance criterion: We defined some SNR's that are directly related to the maxSNR beamspace criterion and evaluated the performances of the filters in the simulations accordingly. The methods have been validated by showing that the energy of the signals coming from the ROI is increased. We also investigated the filter sensitivity to the selection of the ROI parameters, i.e., $\hat{r}$ for the exSSS and $\hat{r}$ and O$'$ for the genexSSS estimator.

5.2 ADVANTAGES AND THE NOVELTY OF THE METHODS

Decomposing the MEG data corresponding to regions of interest may provide valuable insights into the properties of the data and has practical importance for various applications such as brain-computer interfaces [57]. The SSS algorithm attempts to realize this by obtaining the coefficients for the sources of interest inside the sensor array and the external interferences. Thus, SSS decomposes the data into two different components arising from inner head sources and undesired external interferences.

In this dissertation, we propose two novel methods, namely exSSS and genexSSS, in order to extend the capability of the SSS algorithm for a further decomposition of the data to desired locations inside the head. Fourier like representations of MEG data in terms of vector spherical harmonic basis functions yield a very convenient domain for various applications such as total information extraction [64], data continuation around the surface of the sensor array [63] and the exploration of the resolution limits of the inverse problems [51]. In a recent work [80], Taulu and Simola report the relation between the SSS coefficients and the current sources and they showed some relevant interpretations of inverse and forward problems in the SSS domain, where the estimation of the source distributions can efficiently be achieved without any numerical calculations or inversions of the leadfield matrices. They also suggested a weighting scheme derived through a minimization of the mean-square error between the desired coefficients $\boldsymbol{\alpha}$ and the noisy estimate $\hat{\boldsymbol{\alpha}}$, in order to eliminate the sensor noise contributions from the estimated coefficients.

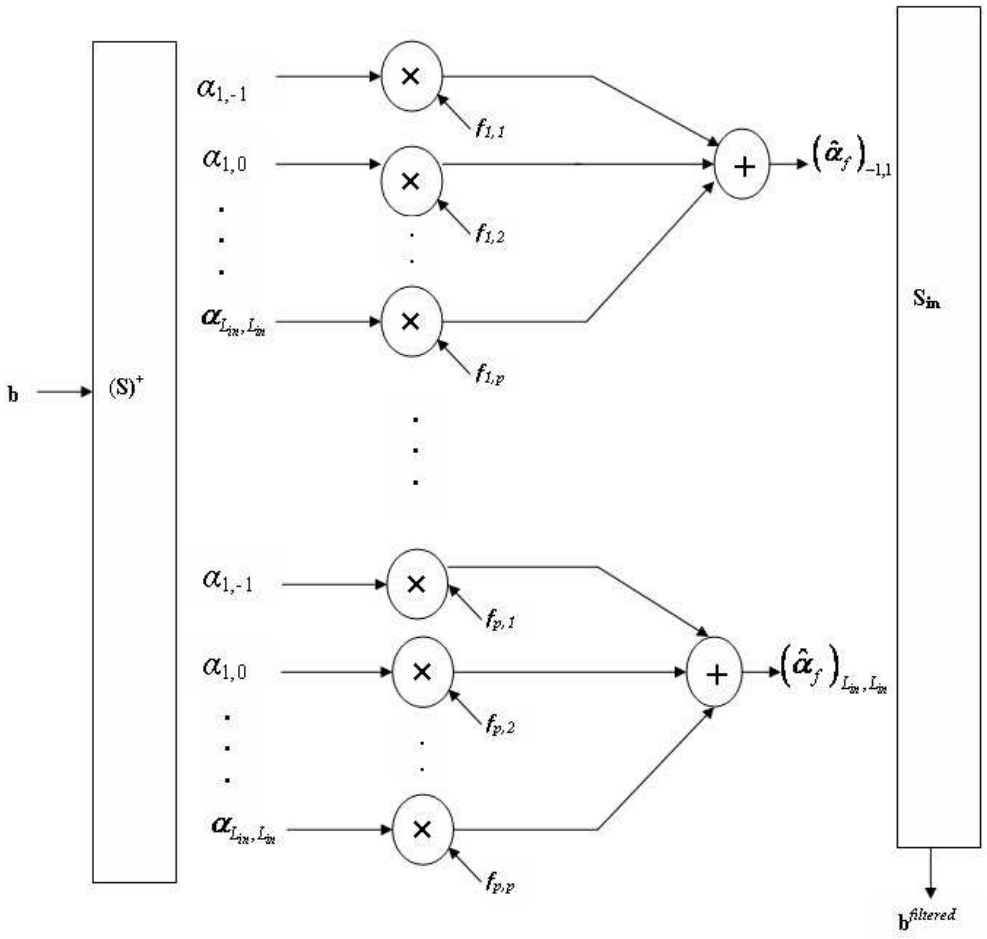

Figure 33: Block diagram for the computational structure of the spatial filtering in the spherical harmonics domain. f_{kl} represents the filter coefficients.

Our algorithms named as exSSS and genexSSS were developed by assuming that the SSS method was already applied to the MEG data and accordingly, it addresses the issue of manipulating the SSS coefficients such that the data can be constrained to any arbitrary spherical source region inside the head volume. The modification of the SSS coefficients was handled through a beamspace optimization criterion known as maxSNR. This methodology assumes the part corresponding to the ROI as "signal" and the remaining parts as "noise". It was used to modify the SSS coefficients such that the energy coming from the ROI is maximized while the energy arising from the remaining source regions is minimized. The simplicity of the derived formulations of exSSS comes from the natural appropriateness to the spherical domain and orthogonality properties of the SSS basis functions that are directly related to the vector spherical harmonics. It is well-known that these functions are orthonormal eigenfunctions of the Laplacian operator on the spherical surface [60]. The origin of the expansion should be selected as symmetrically as possible to the sensors for the success of the separation. Hence the aforementioned deep and superficial components are meant to be defined with respect to the SSS origin in the exSSS method. In the second proposed algorithm genexSSS, we further investigated the inner component to constrain it into arbitrary spherical regions with user specified centers and radii. The formulation of the filter mainly relies on a linear transformation of the SSS coefficients as in exSSS. We have demonstrated that the genexSSS filter is also a generalized form of the exSSS filter and requires only one additional parameter as the ROI center O'. Hence, by computing only one extra parameter as the vector basis function matrix $\tilde{\mathbf{S}}$ that depends on O', the filtering can be realized immediately after application of the SSS method. While both the exSSS and the genexSSS methods fundamentally take into account solely the spatial information, it is straightforward to include data dependency as we applied a simple signal space projection for avoiding possible noisy content.

The simulations and the auditory data experiments were utilized to validate the effectiveness of the filters. The experiments give evidence that the energy ratio of the targeted part to the undesired part is increased by the filters, which shows the masking capability of our methods. We also showed that the filters do not spoil the spatial structure of the input data.

There have been previous attempts for a specified waveform separation such as in [81], which exploits the spectral information of the sources without taking account the spatial consideration. Contrary to those, our approach does not assume or impose any prior information for the source waveforms. Our methods utilize "explicit" spatial filters for the estimation of components that correspond to specific regions of interest. In [57], the authors suggest spatial filters for MEG data utilizing classical leadfields based on sLORETA. It should be noted that the decomposition methodology suggested in this dissertation would not be easy with classical lead field functions since they do not possess the orthogonality property across source regions. Hence, one would have to first determine necessary coordinates by dividing the targeted and the unwanted source volumes into thousands of grids and then compute the Gram matrix discretely unlike the proposed method. Thus, our spatial filtering methods are distinguished especially by their efficiency; that is, they do not require the numerical computation of the leadfields, as do the traditional spatial filtering methods. Moreover, with our approach, while the beamspace transformation matrix is obtained, one does not have to deal with the sensor configurations and dimension reduction, i.e, choosing the eigenvectors of the Gram matrix that correspond to the largest eigenvalues. All these procedures are already previously handled by the SSS method. Hence we use the modified beamspace methodology only for decomposition purposes.

If the desired ROI (hence the parameters O, O$'$, R, $\hat{r}$) is known a priori, one can compute the filters beforehand and apply them to the data via filtering matrices stored on a computer. The pre-knowledge about the ROI's may not have to be precise in order to mask the unwanted sources. This could be the case for the roughly known brain source areas like epileptic seizure regions and auditory cortical regions.

Our methods are relevant to MEG signals for all the application areas mentioned in Section 3.1.2.3. The external noise unrelated to the brain activities is handled by the SSS algorithm incorporated in the exSSS and genexSSS formulations. Additionally, the methods are particularly to be used for the other purposes, namely constraining the signal to an ROI, obtaining deep structures and dimension reduction. Note that while we developed the methods in particular for MEG, it is straightforward to apply a similar spatial filtering ap-

proach and manipulate the multipole coefficients of EEG signals, when there is no significant noise outside the head. In fact, this condition suits to EEG signals since they are not that susceptible to outer noise as in the case of MEG.

5.3 SPECIFIC REMARKS

Source estimation problems can be classified as global and local as described in [82]. The global methods aim at finding a set of solutions that describes the measurements in their entirety. Thus, neglecting one of the sources in a global method would affect the solution for all the remaining sources. Conversely, the local methods aim at identifying sources at a local point or a region but not the entire region (total source space). These kinds of methods such as LCMV beamformers lead to independent local solutions whose summed activity is not generally equivalent to the measured signal $\mathbf{b}$ [82]. exSSS and genexSSS can be considered in the class of local estimators, i.e., they concentrate on only the targeted region (ROI) by using maxSNR beamspace methodology and the solutions for different regions do not yield the total data, even when the unity of these regions encapsulates the total source space.

Since exSSS is a local estimator, the optimizations of the deep and superficial parts are taken into account separately. Hence, when one estimates the deep and the superficial components separately, their summation would not give the total data, i.e, $\hat{\mathbf{b}}_{deep} + \hat{\mathbf{b}}_{sup} \neq \mathbf{b}$. This also explains why the filters in Figure 3 possess some common spatial frequencies. This, though, does not produce difficulty in practice. In cases where the sum of the components must equal $\mathbf{b}$, one still has the option to estimate for any region of interest and subtract it from $\mathbf{b}$. For applications where this sum is unimportant, our method offers another way of decomposition. We had attempted to develop another spatial filtering algorithm for

arbitrary spherical ROI's inside the brain [83], where we suggested shifting the sensors to a virtual spherical array and realizing the beamspace filtering on these selected virtual sensors. However, as mentioned in [83], this method has serious drawbacks in practice, such as the loss of useful signal by the shifting operation and the selection of the optimal locations for virtual sensors. genexSSS is an improvement upon that method, avoiding these pitfalls.

It is worth noting that in particular for genexSSS, the performance of the estimation of $\hat{\mathbf{b}}_f$ is directly dependent upon the external interference suppression capability of SSS, since the formulation of $f(a, b)$ obtained from modified beamspace optimization takes into account only the inner brain sources. Although SSS is expected to eliminate the external interferences, in practice, there is always a leakage that cannot be totally suppressed, as explained in detail in [60], [76]. The suppression capability is lessened as the external sources are located closer to the sensor array [60]. In [84], a method called "spatiotemporal" SSS (tSSS) handles this limitation by an additional null projection that is obtained from the common subspace of inner and outer components. Thus, the use of tSSS can be considered as a more accurate way to obtain $\mathbf{b}_{in}$ before the proposed estimation of $\hat{\mathbf{b}}_f$ and may be a useful temporal supplement to the genexSSS filter in order to remove the external noise close to the sensor array completely in practice.

BIBLIOGRAPHY

[1] M. Hamalainen, R. Hari, R. J. Ilomoniemi, J. Knuutila, and O. V. Lounasmaa, "Magnetoencephalography - theory, instrumentation and applications to noninvasive studies of the working human brain," *Reviews of Modern Physics*, vol. 65, pp. 413–497, 1993.

[2] S. Baillet, J. C. Mosher, and R. M. Leahy, "Electromagnetic brain mapping," *IEEE Signal Processing Magazine*, vol. 18, no. 6, pp. 14–30, 2001.

[3] R. M. Leahy, J. C. Mosher, M. E. Spencer, M. X. Huang, and J. D. Lewine, "A study of dipole localization accuracy for MEG and EEG using a human skull phantom," *Electroencephalography and Clinical Neurophysiology*, vol. 107, no. 2, pp. 159–173, 1998.

[4] S. Baillet, L. Garnero, G. Marin, and J. P. Hugonin, "Combined MEG and EEG source imaging by minimization of mutual information," *IEEE Transactions on Biomedical Engineering*, vol. 46, no. 5, pp. 522–534, 1999.

[5] D. M. Goldenholz, S. P. Ahlfors, M. S. Hamalainen, D. Sharon, M. Ishitobi, L. M. Vaina, and S. M. Stufflebeam, "Mapping the signal-to-noise-ratios of cortical sources in magnetoencephalography and electroencephalography," *Human Brain Mapping*, 2008.

[6] L. Parkkonen and J. Makela, "MEG sees deep sources: Measuring and modeling brainstem auditory evoked fields," in *Proceedings of the 13th International Conference on Biomagnetism*, pp. 107–109, 2002.

[7] C. D. Tesche, "Detecting activity from deep brain areas with magnetoencephalographic arrays," in *Proceedings of the International Conference of IEEE Engineering In Medicine and Biology Society*, vol. 20 of *4*, pp. 2201–2204, 1998.

[8] C. D. Tesche and J. Karhu, "Theta oscillations index human hippocampal activation during a working memory task," in *Proceedings of the National Academic of Sciences of the United States of America*, vol. 97 of *2*, pp. 919–924, 2000.

[9] C. D. Tesche and J. Karhu, "Somatosensory evoked magnetic fields arising from sources in the human cerebellum," in *Brain Research*, vol. 744 of *1*, pp. 23–31, 1997.

[10] S. Taulu and M. Kajola, "Presentation of electromagnetic multichannel data: The signal space separation method," *Journal of Applied Physics*, vol. 97, 2005.

[11] A. Tarantola, *Inverse Problem Theory and Methods for Model Parameter Estimation*. siam, 2005.

[12] J. D. Jackson, *Classical Electrodynamics*. Wiley, 3rd ed., 1998.

[13] D. J. Griffiths, *Introduction to Electrodynamics*. Prentice-Hall, 3rd ed., 1999.

[14] J. E. Marsden and A. J. Tromba, *Vector Calculus*. W.H. Freeman and Company, 4th ed., 1996.

[15] J. Sarvas, "Basic mathematical and electromagnetic concepts of the biomagnetic inverse problem," *Physics in Medicine and Biology*, vol. 32, no. 1, pp. 11–22, 1987.

[16] M. S. Hamalainen and J. Sarvas, "Realistic conductivity geometry model of the human head for interpretation of neuromagnetic data," *IEEE Transactions on Biomedical Engineering*, vol. 36, no. 2, pp. 165–171, 1989.

[17] K. A. Awada, D. R. Jackson, J. T. Williams, D. R. Wilton, S. B. Baumann, and A. C. Papanicolaou, "Computational aspects of finite element modeling in eeg source localization," *IEEE Transactions on Biomedical Engineering*, vol. 44, no. 8, pp. 736–752, 1997.

[18] A. Ribes and F. Schmitt, "Linear inverse problems in imaging," *IEEE Signal Processing Magazine*, vol. 25, no. 4, pp. 84–99, 2008.

[19] O. Hauk, "Keep it simple: a case for using classical minimum norm estimation in the analysis of EEG and MEG data," *Neuroimage*, vol. 21, pp. 1612–1621, 2004.

[20] K. Uutela, M. Hamalainen, and E. Somersalo, "Visualization of magnetoencephalographic data using minimum current estimates," *Neuroimage*, vol. 10, pp. 173–180, 1999.

[21] R. D. Pascual-Marqui, M. Esslen, K. Kochi, and D. Lehmann, "Functional imaging with low resolution brain electromagnetic tomography (LORETA): a review," *Methods and Findings in Experimental and Clinical Pharmacology*, no. 24, pp. 91–95, 2002.

[22] A. A. Ioannides, J. P. R. Bolton, and C. J. S. Clarke, "Continuous probabilistic solutions to the biomagnetic inverse problem," *Inverse Problems*, vol. 6, pp. 523–542, 1990.

[23] I. F. Gorodnitsky and B. D. Rao, "Sparse signal reconstruction from limited data using FOCUSS," *IEEE Transactions on Signal Processing*, vol. 45, no. 3, pp. 600–616, 1997.

[24] H. Liu, X. Gao, P. H. Schimpf, F. Yang, and S. Gao, "A recursive algorithm for the three-dimensional imaging of brain electric activity: shrinking LORETA-FOCUSS," *IEEE Transactions on Biomedical Engineering*, vol. 51, no. 10, pp. 1794–1802, 2004.

[25] H. Liu, P. H. Schimpf, G. Dong, X. Gao, F. Yang, and S. Gao, "Standardized shrinking LORETA-FOCUSS (SSLOFO): a new algorithm for spatio-temporal eeg source reconstruction," *IEEE Transactions on Biomedical Engineering*, vol. 52, no. 10, pp. 1681–1691, 2005.

[26] M. Huang, A. M. Dale, T. Song, H. E., D. L. Harrington, I. Podgorny, J. M. Canive, S. Lewis, and L. R. R., "Vector-based spatialtemporal minimum l1-norm solution for MEG," *Neuroimage*, vol. 31, pp. 1025–1037, 2006.

[27] T. Auranen, A. Nummenmaa, M. S. Hmlinen, I. P. Jskelinen, J. Lampinen, A. Vehtari, and M. Sams, "Bayesian analysis of the neuromagnetic inverse problem with lp-norm priors," *Neuroimage*, vol. 26, no. 3, pp. 870–884, 2005.

[28] K. H. Knuth, "Informed source separation: A Bayesian tutorial," in *Proceedings of the 13th European Signal Processing Conference*, 2005.

[29] K. H. Knuth and H. G. Vaughan, "Convergent bayesian formulations of blind source separation and electromagnetic source estimation," *Maximum Entropy and Bayesian Methods*, pp. 217–226, 1998.

[30] S. Baillet and L. Garnero, "A Bayesian approach to introducing anatamo-functional priors in the EEG/MEG inverse problem," *IEEE Transactions on Biomedical Engineering*, vol. 44, no. 5, pp. 374–385, 1997.

[31] G. S. Russell, R. Srinivasan, and D. M. Tucker, "Bayesian estimates of error bounds for EEG source imaging," *IEEE Transactions on Medical Imaging*, vol. 17, no. 6, pp. 1084–1089, 1998.

[32] J. Capon, "High resolution frequency-wavenumber spectrum analysis," *Proceedings of the IEEE*, vol. 57, p. 14081418, 1969.

[33] B. D. Van Veen, W. Van Drongelen, M. Yuchtman, and A. Suzuki, "Localization of brain electrical activity via linearly constrained minimum variance spatial filtering," *IEEE Transactions on Biomedical Engineering*, vol. 44, no. 9, pp. 867–880, 1997.

[34] K. Sekihara, S. S. Nagarajan, D. Poeppel, A. Marantz, and Y. Miyashita, "Reconstructing spatio-temporal activities of neural sources using an MEG vector beamformer technique," *IEEE Transactions on Biomedical Engineering*, vol. 48, no. 7, pp. 760–771, 2001.

[35] K. Sekihara, S. S. Nagarajan, D. Poeppel, and A. Marantz, "Performance of an MEG adaptive-beamformer technique in the presence of correlated neural activities: effects of signal intensity and time-course estimates," *IEEE Transactions on Biomedical Engineering*, vol. 49, no. 12, pp. 1534–1546, 2002.

[36] J. C. Mosher, P. S. Lewis, and R. M. Leahy, "Multiple dipole modeling and localization from spatio-temporal MEG data," *IEEE Transactions on Biomedical Engineering*, vol. 39, no. 6, pp. 541–557, 1992.

[37] J. C. Mosher, S. Baillet, and R. M. Leahy, "Equivalence of linear approaches in bioelectromagnetic inverse solutions," *IEEE Workshop on Statistical Signal Processing*, pp. 294–297, 2003.

[38] B. D. Van Veen and K. Buckley, "Beamforming: A versatile approach to spatial filtering," *IEEE ASSP Magazine*, pp. 4–24, 1988.

[39] C. D. Tesche, M. A. Uusitalo, R. J. Ilmoniemi, M. Huotilainen, M. Kajola, and O. Salonen, "Signal-space projections of MEG data characterize both distributed and well-localized neuronal sources," *Electroencephalography and Clinical Neurophysiology*, vol. 95, pp. 189–200, 1995.

[40] M. A. Uusitalo and R. J. Ilmoniemi, "Signal space projection method for separating MEG or EEG into components," *Medical and Biological Engineering and Computing*, vol. 35, pp. 135–140, 1997.

[41] G. Nolte and G. Curio, "The effect of artifact rejection by signal-space projection on source localization accuracy in MEG measurements," *IEEE Transactions on Biomedical Engineering*, vol. 46, no. 4, pp. 400–408, 1999.

[42] A. de Cheveigne, J. Le Roux, and J. Z. Simon, "MEG signal denoising based on time-shift PCA," in *IEEE International Conference on Acoustics, Speech and Signal Processing*, vol. 1, pp. 317–320, 2007.

[43] J. Vrba and S. E. Robinson, "Signal processing in magnetoencephalography," *Methods*, vol. 25, no. 2, pp. 249–271, 2001.

[44] R. Vigario, J. Sarela, V. Jousmaki, M. Hamalainen, and E. Oja, "Independent component approach to the analysis of EEG and MEG recordings," *IEEE Transactions on Biomedical Engineering*, vol. 47, no. 5, pp. 589–593, 2000.

[45] C. J. James and O. J. Gibson, "Temporally constrained ICA: An application to artifact rejection in electromagnetic brain signal analysis," *IEEE Transactions on Biomedical Engineering*, vol. 50, no. 9, pp. 1108–1116, 2003.

[46] S. Iwaki, C. Yamamoto, S. Takehara, M. Tonoike, and T. Yamamoto, "Rejection of stimulus-related artifacts from electro-gustatory magnetoencephalographic signals using independent component analysis," *IEEE Transactions on Magnetics*, vol. 38, no. 5, pp. 3381 – 3383, 2003.

[47] T. Sander, G. Wubbeler, A. Lueschow, G. Curio, and L. Trahms, "Cardiac artifact subspace identification and elimination in cognitive MEG data using time-delayed decorre-

lation," *IEEE Transactions on Biomedical Engineering*, vol. 49, no. 4, pp. 1108–1116, 2002.

[48] N. E. Ahmar and J. Z. Simon, "MEG adaptive noise suppression using fast LMS," in *Proceedings of the 2nd International IEEE EMBS Conference. on Neural Engineering.*

[49] I. Constantin, C. Richard, R. Lengelle, and L. Soufflet, "Regularized kernel-based wiener filtering. application to magnetoencephalographic signals denoising," in *IEEE International Conference on Acoustics, Speech and Signal Processing*, vol. 4, pp. 289–292, 2005.

[50] J. Gross and A. A. Ioannides, "Linear transformations of data space," *Physics in Medicine and Biology*, vol. 44, pp. 2081–2099, 1999.

[51] P. P. Mitra and H. Maniar, "Concentration maximization and local basis expansions (LBEX) for linear inverse problems," *IEEE Transactions on Biomedical Engineering*, vol. 53, no. 9, pp. 1775–1782, 2006.

[52] Y. Attal, M. Bhattacharjee, J. Yelnik, B. Cottereau, J. Lefevre, Y. Okada, E. Bardinet, M. Chupin, and S. Baillet, "Modeling and detecting deep brain activity with MEG & EEG," in *International Conference of the IEEE Engineering in Medicine and Biology Society*, pp. 4937–4940, 2007.

[53] T. E. Özkurt, M. Sun, and R. Sclabassi, "Beamspace magnetoencephalographic signal decomposition in spherical harmonics domain," in *International Conference of the IEEE Engineering in Medicine and Biology Society*, (New York, USA), 2006.

[54] T. E. Özkurt, M. Sun, and R. Sclabassi, "Decomposition of magnetoencephalographic data into components corresponding to deep and superficial sources," *IEEE Transactions on Biomedical Engineering*, vol. 55, no. 6, pp. 1716–1727, 2008.

[55] A. Rodriguez, B. V. Baryshnikov, B. D. Van Veen, and R. T. Wakai, "MEG and EEG source localization in beamspace," *IEEE Transactions Biomedical Engineering*, vol. 53, no. 3, pp. 431–441, 2006.

[56] J. P. R. Bolton, J. Gross, L. C. Liu, and A. A. Ioannides, "SOFIA: spatially optimal fast analysis of biomagnetic signals," *Physics in Medicine and Biology*, vol. 44, pp. 87–103, 1999.

[57] M. Congedo, "Subspace projection filters for real-time brain electromagnetic imaging," *IEEE Transactions Biomedical Engineering*, vol. 53, no. 8, pp. 1624–1634, 2006.

[58] M. Congedo, F. Lotte, and A. Lecuyer, "Classification of movement intention by spatially filtered electromagnetic inverse solutions," *Physics in Medicine and Biology*, vol. 51, pp. 1971–1989, 2006.

[59] K. Sekihara, S. S. Nagarajan, D. Poeppel, and A. Marantz, "Neuromagnetic source reconstruction and inverse modeling," in *IEEE EMBS Asian-Pacific Conference on Biomedical Engineering*, pp. 28–31, 2003.

[60] S. Taulu, J. Simola, and M. Kajola, "Applications of the signal space separation method," *IEEE Transactions on Signal Processing*, vol. 53, no. 9, pp. 3359–3372, 2005.

[61] G. Arfken, *Mathematical Methods for Physicists*. New York: Academic Press, 3rd ed., 1985.

[62] E. L. Hill, "The theory of vector spherical harmonics," *American Journal of Physics*, vol. 22, pp. 211–214, 1954.

[63] M. Popov, "Data continuation for the explicit solution of an inverse biomagnetic problem," *IEEE Transactions on Magnetics*, vol. 38, no. 6, pp. 3620–3632, 2002.

[64] J. Nenonen, S. Taulu, M. Kajola, and A. Ahonen, "Total information extracted from MEG measurements," *International Congress Series*, vol. 1300, pp. 245–248, 2007.

[65] G. Nolte, T. Fieseler, and G. Curio, "Perturbative analytical solutions of the magnetic forward problem for realistic volume conductors," *Journal of Applied Physics*, vol. 89, no. 4, pp. 2360–2369, 2001.

[66] K. Jerbi, J. C. Mosher, S. Baillet, and R. M. Leahy, "On MEG forward problem using multipolar expansions," *Physics in Medicine and Biology*, vol. 47, pp. 523–555, 2002.

[67] R. E. Alvarez, "Filter functions for computing multipole moments from the magnetic field normal to a plane," *IEEE Transactions on Medical Imaging*, vol. 10, no. 3, pp. 375–381, 1991.

[68] Elekta Neuromag Oy, Helsinki, Finland, *MaxFilter User's Guide*, 2005.

[69] A. I. Ahonen, M. S. Hamalainen, R. J. Ilmoniemi, M. J. Kajola, J. E. T. Knuutila, J. T. Simola, and V. A. Vilkman, "Sampling theory for neuromagnetic detector arrays," *IEEE Transactions on Biomedical Engineering*, vol. 40, no. 9, pp. 859–869, 1993.

[70] T. E. Özkurt, M. Sun, W. Jia, and R. Sclabassi, "Spatial filtering of MEG signals for user-specified spherical regions," *submitted to IEEE Transactions on Biomedical Engineering*, 2009.

[71] L. Rouve, L. Schmerber, O. Chadebec, and A. Foggia, "Optimal magnetic sensor location for spherical harmonc identification applied to radiated electrical devices," *IEEE Transactions on Magnetics*, vol. 42, no. 4, pp. 1167–1170, 2006.

[72] Elekta Neuromag Oy, Helsinki, Finland, *Elekta Neuromag System Hardware User's Manual*, 2005.

[73] C. Eulitz, E. Diesch, C. Pantev, S. Hampson, and T. Albert, "Magnetic and electrical brain activity evoked by the processing of tone and vowel stimuli," *The Journal of Neuroscience*, vol. 15, no. 4, pp. 2748–2755, 1995.

[74] E. Y. Kanal, T. E. Özkurt, M. Sun, and R. Sclabassi, "MEG imaging of prefrontal and striatal activity during a gambling task," in *Neuroscience Meeting Planner. Online.*, 2008.

[75] X. Liu, D. K. Powell, H. Wang, B. T. Gold, C. R. Corlby, and J. E. Joseph, "Functional dissociation in frontal and striatal areas for processing of positive and negative reward information," *The Journal of Neuroscience*, vol. 17, no. 27, pp. 4587–4597, 2007.

[76] T. Song, S. Taulu, R. R. Lee, and M. Huang, "Evaluation of signal space separation via simulation," *International Congress Series*, vol. 1300, pp. 265–268, 2007.

[77] M. Popescu, E. Popescu, T. Chan, S. D. Blunt, and J. D. Lewine, "Spatio-temporal reconstruction of bilateral auditory steady-state responses using MEG beamformers," *IEEE Transactions on Biomedical Engineering*, vol. 55, no. 3, pp. 1092–1102, 2008.

[78] S. S. Dalal, K. Sekihara, and S. S. Nagarajan, "Modified beamformers for coherent source region suppression," *IEEE Transactions on Biomedical Engineering*, vol. 53, no. 7, pp. 1557–1563, 2006.

[79] D. G. Manolakis, V. K. Ingle, and S. M. Kogon, *Statistical and Adaptive Signal Processing*. McGraw-Hill, 2000.

[80] S. Taulu and J. Simola, "Multipole-based coordinate representation of a magnetic multichannel signal and its application in source modelling," Tech. Rep. Report TKK-F-A855, Helsinki University of Technology Publications in Engineering Physics, 2008.

[81] B. S. Kim, K. Kobayashi, and Y. Uchikawa, "Separation of overlapping activity in first and second somatosensory evoked fields with 3-d MEG measurement," *IEEE Transactions on Magnetics*, vol. 39, no. 5, pp. 3387–3389, 2003.

[82] R. E. Greenblat, A. Ossadtchi, and M. E. Pflieger, "Local linear estimators for the bioelectromagnetic inverse problem," *IEEE Transactions on Signal Processing*, vol. 53, no. 9, pp. 3403–3412, 2005.

[83] T. E. Özkurt, M. Sun, and R. Sclabassi, "Spatial filtering of MEG signals for spherical regions in the source space," in *Proceedings of the IEEE 34th Annual Northeast Biomedical Conference*, 2008.

[84] S. Taulu and J. Simola, "Spatiotemporal signal space separation method for rejecting nearby interference in MEG measurements," *Physics in Medicine and Biology*, vol. 51, pp. 1759–1768, 2006.